Instituto Tecnológico y de Estudios Superiores de Monterrey

Campus Monterrey

School of Engineering and Sciences

TECNOLÓGICO
DE MONTERREY ®

Implantable platform with in-situ vascularization and localized
immunosuppression for allogeneic cell transplantation.

A dissertation presented by

Jesús Páez Mayorga

Submitted to the
School of Engineering and Sciences
in partial fulfillment of the requirements for the degree of

Doctor of Philosophy

In

Biotechnology

Monterrey Nuevo León, April 9th, 2021

Dedication

A mis padres, Silvia y Ernesto, por su apoyo y amor incondicional. Este trabajo es tan suyo como lo es mio.

Acknowledgements

Implantable platform with in-situ vascularization and localized immunosuppression for allogeneic cell transplantation.

By

Jesús Páez Mayorga

Abstract

Allogeneic islet transplantation for diabetes management faces the challenge of preventing immune rejection while maintaining enough graft oxygenation for proper metabolic function. Islet encapsulation within membranes impermeable to immune cells prevents rejection at the expense of optimal graft oxygenation. Conversely, direct vascularization avoids hypoxia but requires systemic administration of toxic immunosuppressive drugs. To overcome this problem, we developed the subcutaneously implantable NICHE platform, which integrates in situ graft vascularization and local immunosuppressant delivery, for long-term islet engraftment.

NICHE, 3D-printed in nylon, is comprised of independent drug and cell reservoirs separated by a nanoporous membrane. The membrane allows steady local diffusion of immunosuppressant from the drug reservoir into the cell reservoir. Enhanced NICHE vascularization was assessed using mesenchymal stem cells (MSC) and platelet rich plasma (PRP) in rats and non-human primates (NHP). Tunability of antibody and peptide release from NICHE was tested in vitro. Transplantation of allogeneic islets into prevascularized NICHE with localized co-delivery of anti-lymphocyte serum (ALS) and CTLA4Ig was evaluated in immunocompetent diabetic rats.

NICHE loaded with MSC had dense vascularity within the cell reservoir by 4 weeks of subcutaneous implantation in rats and NHP. In vitro drug release was tuned via modification of membrane exchange area and drug concentration loaded. In diabetic rats, localized co-delivery of ALS and CTLA4Ig protected allogeneic islets, resulting in reversal to euglycemic state for at least 60 days. Transplanted rats with NICHE responded to glucose challenge comparable to healthy controls and had significantly higher c-peptide levels than no-implant diabetic controls, demonstrating full graft function. ALS-CLTA4Ig co-delivery via NICHE localized drug at the transplant site with limited accumulation in plasma and peripheral tissues, avoiding potential toxicity. Moreover, circulating lymphocyte population remained intact, indicating rats were not systemically immunosuppressed.

NICHE is an effective platform for islet allotransplantation with promising adaptability for use with other cell types and pathologies.

List of Figures

Contents

Chapter 1

Introduction

1.1 Motivation

Technological advances in cell encapsulation are poised to profoundly transform the field of islet transplantation for management of type I diabetes (T1D) [1]. Currently, with the conventional approach of portal vein infusion, >60% of infused islets are destroyed within hours by the host immune response [2], leading to transplant failure. Cell encapsulation compartmentalizes transplanted cells within a semipermeable protected environment, preventing host immune destruction while maintaining facile mass transport for cell viability. Although various islet encapsulation approaches are under investigation, none have reached clinical implementation [3-5].

1.2 Problem Statement and Context

Foremost amongst the outstanding challenges in current encapsulation approaches are limitation in host vascular support as well as protection from host immune rejection. While immuno-barrier approaches provide immune protection, poor oxygen permeability and lack of vascularization through the encapsulation material creates a hypoxic environment inhospitable for long-term cell viability, such as in the case of Pec-Encap (Viacyte). Exogenous oxygen supplementation through external ports (β-Air; Beta-O_2) to address encapsulation anoxia demonstrated clinical feasibility for daily refilling [6, 7]. However, lack of islet apposition to blood vessels likely impaired facile mass transport critical for metabolic activity, affecting graft viability and function [7, 8]. In light of this, encapsulation technologies such as Cell Pouch (Sernova) or Pec-Direct (Viacyte) allow for direct vascularization into the device, which is anticipated to improve engraftment [2]. However, these approaches require chronic systemic immunosuppression, which is associated with islet toxicity [9, 10] and life-threatening adverse effects [11, 12]. Therefore, there is a critical need for an encapsulation strategy that provides both host vasculature support and immune protection to preserve islet engraftment.

As key immune rejection events occur in the graft and microenvironment, in situ immunosuppression is a logical approach to protect transplanted islets. The prime concern of other preclinical local immunosuppressive approaches (hydrogels, osmotic pumps, polymer-based microsphere or scaffolds) is that they were short-term and did not address encapsulation site anoxia [13-19]. Fundamentally, a long-lasting engraftment system requires: 1) facile mass transport (oxygen, nutrients, etc.) for transplanted islet viability and function; 2) protection from host immune rejection; 3) biocompatibility and mechanical stability for long-term deployment; 4) clinical feasibility for transplantation procedures (cell injection and replenishing) and retrievability in the event of medical complications; and 5) scalability to achieve clinically-relevant encapsulation capacity.

1.3 Research Questions

1. How can sufficient mass transport and immune system evasion be integrated within the same encapsulation platform for successful allogeneic islet transplantation?
2. Is a pre-vascularized niche with localized immunosuppression effective for transplantation of allogeneic islets to manage diabetes?

3. How can vascularization within a subcutaneously implantable device be enhanced to yield efficient cell engraftment?
4. Can localized immunosuppressant delivery effectively inhibit graft rejection without inducing systemic immunosuppression?

1.4 Solution Overview

We developed a clinically translatable solution to address the fundamental requirements for successful islet encapsulation, the neovascularized implantable cell homing and encapsulation (NICHE) platform [20]. The NICHE is an encapsulation platform integrating in situ prevascularization and local immunosuppressant delivery. Localized immunosuppressant delivery to prevent immune rejection could improve engraftment and obviate effects of systemic immunosuppression, while a pre-vascularized environment supports long-term engraftment.

NICHE deployment first entails creating a vascularized environment. To achieve this, NICHE is preloaded with a hydrogel containing mesenchymal stem cells (MSC) and subcutaneously implanted. MSC produce paracrine growth and angiogenic factors, which potentiate angiogenesis and subcutaneous tissue penetration into the cell reservoir [31, 32]. After pre-vascularization, immunosuppressant is transcutaneously loaded into the drug reservoir for local release to establish an immunosuppressed milieu. Finally, islets are transcutaneously co-transplanted with MSC into the cell reservoir of the preconditioned NICHE, which is a highly vascularized, immunoprotected environment conducive to engraftment. Co-transplantation with MSC leverages their immunomodulatory potential to further inhibit rejection and enhance engraftment.

The subcutaneous site is commonly used for implantation of therapeutic devices due to ease of access or retrievability. Numerous clinically tested islet encapsulation platforms such as Sernova's Cell Pouch, and Viacyte's Pec-Direct and Pec-Encap are implanted subcutaneously [1]. Subcutaneous implantation of the NICHE permits minimally invasive and easy transcutaneous access for loading and refilling of drugs or islets. In clinical trials, the Sernova platform is subcutaneously implanted in the abdomen or volar forearm, while Viacyte's devices are placed in the flank. Similarly, for future clinical deployment, we envision the NICHE to be subcutaneously implanted in the inner forearm for discretion, protection from external impact, as well as for ease of access.

1.5 Main contributions

Our NICHE encapsulation platform is unique and conceptually innovative as it integrates local immunosuppressant delivery and prevascularization in one device, distinct from other technologies. Key innovative aspects of the NICHE include the following: *1) Multifunctional platform technology:* The dual cell-drug reservoir architecture allows for microenvironment conditioning pre- and post- transplantation, with potential for sequential elution of cytokines, growth factors, and immunosuppressants. For example, pre-transplantation, sustained elution of

vascular endothelial growth factor (VEGF) could aid MSC and host vascular progenitor cell populations in establishing an optimal vascular network, which is essential for transplant viability and function. Post-transplantation, the drug reservoir can be used for sequential elution of immunosuppressants to address acute and chronic rejections. *2) Localized immune protection of transplanted cells*. Sustained elution of immunosuppressants directly into cell reservoir provides in situ immunoprotection. This resolves the significant clinical issue of adverse effects associated with lifelong systemic immunosuppression. In addition, localized drug delivery offers opportunities for promising immune modulators that present systemic toxicity. *3) Flexibility.* The NICHE can be adopted for the delivery of various cell types for multiple clinical indications beyond diabetes. Further, the NICHE is drug-agnostic and can be used for sustained elution of a broad spectrum of molecules, including imaging agents for transplant monitoring. Additionally, it does not require drug reformulation as in the case for polymeric delivery systems. *4) Repeated cell and drug refillability* are fundamental for long-term clinical deployment of implantable delivery devices. While the NICHE can be implanted anywhere, subcutaneous implantation allows for minimally invasive transcutaneous accessibility. This enables straightforward therapy replenishment for long-term deployment without necessitating surgeries, external ports or complex image guidance. *5) Rapid scalability and customization.* The NICHE is designed to allow for straightforward scalability and customization via additive manufacturing. This is of utmost importance to accommodate sufficient cell mass for clinical deployment. Collectively, our encapsulation platform is biotechnologically innovative and encompasses design features derived from material science, mechanical engineering, tissue regeneration, and immunology to address the lack of an all-encompassing encapsulation for clinical cell transplantation.

1.6 Dissertation Organization

This research work was structured in 3 specific aims:

Aim 1: To elucidate a clinically feasible approach to enhance vascularization of subcutaneously implanted NICHE.

Aim 2: To demonstrate feasibility of NICHE for allogeneic cell transplantation and localized immunosuppression in a proof of concept study.

Aim 3: To assess NICHE efficacy for pancreatic islet allotransplantation to cure diabetes in an immunocompetent rat model.

Chapter 2

Methodology

2.1 Materials and methods for chapter 3

2.1.1 Encapsulation device fabrication

Parts for the device were 3D-printed (Bioplotter, EnvisionTec, Gladbeck, Germany) in polylactic acid (PLA; Foster corporation, Putnam, CT, USA) by fused deposition modeling technique as previously described [21]. 3D dataset for the fabrication process were created using Solidworks® (Dassault Systemes, Velizy-Villacoublay, France). The discoidal device has a diameter of 9 mm, a thickness of 2.5 mm, and a reservoir volume of 120 μL. The surface of the device consists of an array of microchannels with a nominal cross section of 100 μm x 100 μm. A lateral loading port (1 mm diameter) sealed with medical grade silicone (Nusil, USA) allows access into the reservoir for gel and cell loading.

2.1.2 Scanning Electron Microscopy (SEM) Imaging

3D-printed devices were sputtered with 7 nm iridium and imaged using Nova NanoSEM 230 at the Houston Methodist Research Institute Scanning Electron Microscopy and Atomic Force Microscopy Core.

2.1.3 PRP hydrogel preparation

PRP was autologous. Two days prior to device implantation, whole blood was collected in EDTA tubes (BD Biosciences, San Jose, CA, USA). Within 1 h of collection, tubes were centrifuged at 1600 rpm for 30 minutes. The top layer containing PRP was transferred to a clean tube and centrifuged again at 1600 rpm for 30 minutes to pellet any remaining red blood cells. Supernatant containing PRP was collected. Sodium alginate solubilized in platelet-rich plasma (PRP) was cross linked with calcium chloride in order to form a growth factor enriched hydrogel following a previously described method [21].

2.1.4 PB-MSC isolation

Autologous PB-MSCs were isolated from whole blood as previously described [22]. Briefly, whole blood was collected from each animal in heparinized tubes (BD Biosciences) and the mononuclear cell (MNC) fraction isolated using Ficoll density gradient. Isolated cells were cultured in 75 cm^2 flasks with DMEM (Sigma, St Louis, MO, USA), 0.1 mM nonessential amino acids, 100-U/ml penicillin and streptomycin, 1 ng/ml basic fibroblast growth factor (FGF), 10% FCS, and 0.2 mM L-glutamine. Isolated cells positive for markers CD105, CD90, CD29 and negative for markers of hematopoietic lineage, CD14, CD34, CD45 were defined as MSCs.

2.1.5 PB-MSCs hydrogel preparation

Subconfluent cultures of MSCs were detached with 0.25% trypsin (Gibco, Thermo Fisher Scientific, Waltham, MA, USA). Cells were pelleted and re-suspended in 100 μL of pluronic-F127 hydrogel (15% in DMEM) [23, 24]. The average MSC yield was

$5.5 \pm 1.3 \times 10^5$ cells per animal. The MSCs-hydrogel was injected into the devices and allowed to gel at 37 ºC.

2.1.6 In vivo vascularization assessment

8-week-old Sprague-Dawley (SD) rats (n=36) (Charles River, Houston, TX, USA), and 7-19-year-old Indian rhesus macaques (*Macaca mulatta*) (n=3) were used in this study. SD rats were kept in the Houston Methodist Research Institute, Houston TX. All procedures were approved by the Houston Methodist Institutional Animal Care and Use Committee (#0717-0040) in accordance with the National Institute of Health Guide for the Care and Use of Laboratory Animals and the Animal Welfare Act. Rhesus macaques were bred and kept at the AAALAC-I accredited Michale E. Keeling Center for Comparative Medicine and Research, The University of Texas MD Anderson Cancer Center (UTMDACC), Bastrop, TX. All experiments were carried out according to the provisions of the Animal Welfare Act, PHS Animal Welfare Policy, and the principles of the NIH Guide for the Care and Use of Laboratory Animals. All procedures were approved by the Institutional Animal Care and Use Committee at UTMDACC (#00001749-RN00). Devices loaded with PRP, MSCs or vehicle hydrogel (Control) were implanted subcutaneously in the dorsum of animals (n=12 devices/group; n=3 devices/time point). For rats, each animal was implanted with one device. For NHP, each animal was implanted with 12 devices (n=4 per group; n=1 per time point). At 1, 2, 4, and 6 weeks post-implantation, devices with surrounding tissue were collected and processed for histology (n=3 devices per group/time-point).

2.1.7 Histopathology and IHC staining

Harvested devices on week were fixed in 10% formalin overnight, transferred to 10% sucrose solution for 48 h and then stored in 1% sucrose solution. To assess device biointegration while preserving in vivo architecture, we performed resin embedding that allowed us to section through PLA polymer. For this purpose, devices were embedded in polymethyl methyl acrylate (PMMA) resin, sectioned at a thickness of 10 μm and stained with Hematoxylin and Eosin (H&E) (n=1 device per time-point, per group). The tissue processing for resin embedding is incompatible with immunohistochemical labeling. As such, for blood vessel quantification, tissues were dissected out of explanted devices and embedded in paraffin. Devices in 1% sucrose were transferred to 70% ethanol for 24 h and subsequently processed for paraffin embedding with routine ethanol and xylene washes (n=2 devices per time-point per group). For rat samples, sections were stained with lectin from *Bandeiraea simplicifolia* (BS-1) as previously described [20]. For NHP samples, following deparafinization and antigen retrieval in citrate buffer pH 6.0 for 20 min, sections were incubated with CD31 (Abcam, Cambridge, MA, USA) for 1 h at room temperature, followed by incubation with HRP-conjugated secondary antibody and developing using 3,3'-Diaminobenzidine (DAB) system. For maturity marker assessment, devices in 1% sucrose solution were embedded in optimal cutting temperature (OCT) medium and snap frozen in liquid nitrogen. Frozen sections were blocked with 5% normal goat serum and incubated overnight with mouse anti-CD31

(Novus Biologicals, Centennial, CO, USA) and rabbit anti-eNOS (Abcam). Secondary antibodies were rhodamine-conjugated goat anti-mouse (ThermoScientific, Waltham, MA, USA) and FITC-conjugated sheep anti-rabbit (MP Biomedicals, Irvine, CA, USA). For negative controls, immunoglobulin (IgG) and species-matched isotype control antibodies were used to set baseline values. Preparations for imaging of tissue sections were mounted in Slow Fade GOLD with 4',6-diamidino-2-phenylindole (DAPI) (Molecular Probes, OR, USA) and observed using a Nikon T300 Inverted Fluorescent microscope (Nikon, Tokyo, Japan). For eNOS quantification, green (FITC) fluorescence intensity was measured in 9 regions of interest for each condition using NIKON NIS-Elements (Imaging software, Nikon Instruments Inc.).

2.1.8 Blood vessel quantification

For blood vessel density quantification, BS-1 and CD31-stained sections were used for rat and NHP samples, respectively. At least 8 fields of view per condition were randomly imaged using an Olympus IX51 wide field microscope and blood vessels quantified by a blinded scientist. Vessel density was reported as vessel number per mm^2 using equation (1).

$$\textbf{Blood vessel density} = \frac{\textbf{Vessel number}}{\textbf{FOV area}} \qquad (1)$$

Regional vessel quantification of tissue in devices implanted for 4 weeks was performed on resin-embedded H&E slides. At least two slides >100 µm apart containing whole cross sections per explanted device were quantified by two blinded scientists. To evaluate the spatial distribution of blood vessels, full cross sections of devices were equally divided in thirds: top (section closer to skin), middle, and bottom (section closer to muscle). Blood vessels were counted and reported as percentage of total blood vessels in the device using the equation (2).

$$\textbf{Blood vessel \%} = \frac{\textbf{Regional vessel number}}{\textbf{Total vessel number}} \textbf{ x 100} \qquad (2)$$

2.1.9 Statistical analysis

All results are expressed as mean ± standard deviation. Sample sizes are specified in each figure legend. Statistical analyses were performed using Prism 8 software (GraphPad Software Inc., San Diego, CA, USA). The number of animals allowed to detect statistical differences between groups with 80% power. One-way Analysis of variance (ANOVA) with Tukey's multiple comparisons test were performed to determine statistical significance of differences among groups, and P values less than 0.05 were considered significant. Significance was indicated as follows: *, $p \leq 0.05$; **, $p \leq 0.01$; and ***, $p \leq 0.001$.

2.2 Materials and methods for chapter 4

2.2.1 Device fabrication and sterilization procedure
NICHE was fabricated by 3-dimensional printing (Sculpteo, CA) with selective laser sintering using biocompatible polyamide PA 2200 (Electro Optical Systems). Three-dimensional datasets for the fabrication process were created using Solidworks (Dassault Systemes, Velizy-Villacoublay, France). NICHE has a flat rectangular structure and dimensions of 25 mm × 14.6 mm × 5.0 mm (Fig. 2A). The drug reservoir (~345 μL) included within the main structure of NICHE has a '*U*' shape and surrounds the cell reservoir (19 mm × 6 mm × 4.4 mm; 502 mm^3) on 3 sides. Immunosuppressant drug is eluted from the drug reservoir into the cell reservoir through two 100-nm nanoporous nylon membranes (GVS, Sanford, ME), which are affixed between the drug and cell reservoirs with implantable-grade, biocompatible fast-cure silicone adhesive (MED3-4213; NuSil). The top and bottom surfaces of the cell reservoir are created by 2 nylon meshes, an inner nylon mesh with 300 μm × 300 μm openings, and an outer nylon mesh with 100 μm × 100 μm openings. Assembled NICHEs were sterilized with sequential washes of 0.3% H_2O_2, 0.03% H_2O_2, 70% ethanol, and sterile H_2O under a clean laminar flow hood.

2.2.2 Assessment of polyamide PA 2200 degradation
Three-dimensionally printed NICHEs (n=10) were weighed and completely immersed in glass scintillation vials containing 22 mL of phosphate-buffered saline (PBS; Gibco) and incubated at 37°C. At weeks 1, 2, 4, 6, 8, 16, and 32 NICHEs were rinsed in distilled water to remove excess salt, dried using absorbent tissue and the weights were recorded (XPE56 Microbalance; Mettler Toledo Greifensee, 174 Switzerland). Material degradation was assessed via weight change percentage relative to day 0 using equation (3). Where W_0 is the original device weight and W_t is the device weight at each time point.

$$\mathbf{WC\%} = \frac{\mathbf{W_t - W_0}}{\mathbf{W_0}} \mathbf{\ x\ 100} \qquad\qquad (3)$$

2.2.3 Scanning Electron Microscopy (SEM) Imaging
Nylon meshes and membranes were fixed in 10% formalin, dehydrated in ethanol and sputtered with 7nm iridium. Imaging was performed using Nova NanoSEM 230 under high vacuum setting and 5 kV electron beam at the Houston Methodist Research Institute Scanning Electron Microscopy and Atomic Force Microscopy Core.

2.2.4 In vitro cytotoxicity assays
To assess the biocompatibility of NICHE and toxicity of Cytotoxic T-Lymphocyte Associated protein 4 Immunoglobulin (CTLA4Ig), we performed cytotoxicity studies on mesenchymal stem cells (MSCs), human umbilical vein endothelial cells (HUVECs), and rat Leydig cells (LC540). MSCs were cultured in StemXVivo

Mesenchymal Stem Cell Expansion Media (R&D Systems); HUVECs were cultured in endothelial cell growth medium (Angio-Proteomie); Leydig cells were cultured in Eagle's minimal essential medium supplemented with 10% FBS, 100 U/mL penicillin, and 100 µg/mL streptomycin. NICHE extract was generated as follows: sterile NICHEs were incubated with 12 mL of appropriate medium for each cell line at 37°C for 72 h. The 100% extract was then diluted to 50% and 25% using complete medium pre-incubated at 37°C for 72h. For cell viability assays, 5 x 10^3 cells/well were seeded in 96-well plates and incubated overnight to allow cell adherence. The next day, culture medium was aspirated and replenished with 50%, or 25% extract or with complete medium containing the immunosuppressant CTLA4Ig (Orencia; Bristol-Myers-Squibb) at final concentrations of 5, 25, or 50 µg/mL. Twenty-four hours later, MTT assay was performed using the TACS MTT cell proliferation assay (R&D systems) following the manufacturer's instructions.

2.2.5 In vitro CTLA4Ig release assays
CTLA4Ig was conjugated to Alexa Fluor 647 NHS ester (Invitrogen) following the manufacturer's instructions. Then 1, 2, 3.4, and 11 mg/mL CTLA4Ig stock solutions were made by mixing unlabeled and AlexaFluor647-conjugated drug at a 9:1 ratio. Stock solutions were injected into the drug reservoir of NICHEs (n=5/group) using 25G needles. Loaded NICHEs were submerged in glass scintillation vials containing 22 mL of PBS and incubated at 37°C under magnetic agitation. Every third day, samples of sink solution were collected and measured with a fluorometer and the sink solution was fully replenished.

2.2.6 Assessment of CTLA4Ig stability in vitro
CTLA4Ig solution was prepared in PBS at 3.00 mg/mL concentration and filtered through 0.2 µm syringe filter. 1 mL aliquots of the filtered solution were placed in High Performance Liquid Chromatography (HPLC) vials and capped. Solutions were incubated at 37 °C under gentle agitation. Stability of CTLA4Ig was assessed at time points of 0, 1, and 3 weeks by gel permeation chromatography (GPC). GPC analyses were performed at 37 °C using GPCmax pump/autosampler/degasser system (Malvern Panalytical, Malvern, UK). Refractive index signals were recorded using Viscotek TDA305 detector (Malvern Panalytical) and absorbance signals at 280 nm were recorded using Viscotek 2600 UV-Vis detector (Malvern Panalytical). Chromatography was conducted using Viscotek A4000 aqueous column (300×8.0 mm) (Malvern Panalytical), PBS spiked with sodium azide as an eluent, 1.000 mL/min flow rate, and 25 µL injections.

2.2.7 Generation of bioluminescent cell line
HEK293T cells (ATCC) were used for transfection. Twenty-four hours before transfection, 5 × 10^5 cells were seeded on a 6-well plate. On the day of transfection, cell culture medium was replaced with 1 mL of fresh complete medium. Two 1.5-mL Eppendorf tubes were prepared. One tube contained a mixture of 1 mL of serum-free DMEM, 4 µg of pHIV-luc-ZsGreen plasmids (Addgene #39196), 3 µg of psPAX2 plasmids (for packaging, Addgene #12260), and 1 µg of pMD2.G plasmids (for

expressing VSV-G, Addgene #12259). The other tube contained a mixture of 1 mL of serum-free DMEM and 21 µL of polyethyleneimine (linear, 25,000MW, ChemCruz, sc-360968, stock solution 1 mg/mL in dH_2O). The contents of tubes 1 and 2 were mixed in a single tube and incubated for 20 min at room temperature. The HEK293T cells were incubated with the transfection mixture overnight, and then the mixture was replaced with fresh complete medium. Twenty-four hours later, the medium containing lentivirus was filtered and used for transduction. To establish bioluminescent cell line LC540-luc-ZsGreen, 80% confluent LC540 cells (Leydig cells) were transduced with lentivirus-containing medium for 24 h. After several passages, ZsGreen-positive cells were sorted by FACS (BD FACS Aria III) and used for experiments.

2.2.8 Animal models
Eight-week-old male Wistar Furth rats (Charles River, Houston, TX, USA) were used in this study. All animals were maintained and used in conformity with guidelines established by the American Association for Laboratory Animal Science. Rats were kept in the Houston Methodist Research Institute animal facility. All procedures were approved by the Houston Methodist Institutional Animal Care and Use Committee in accordance with the National Institute of Health Guide for the Care and Use of Laboratory Animals and the Animal Welfare Act. Animals had access to food and water ad libitum.

2.2.9 Generation and implantation of MSC-NICHEs and vascularization study
MSCs isolated from bone marrow of Wistar Furth rats were obtained from Cyagen at P2 and expanded in vitro using StemXVivo Mesenchymal Stem Cell Expansion Media (R&D Systems). Osteogenic, chondrogenic and adipogenic differentiation potential was confirmed to ensure MSC lineage (Appendix A1).

On implantation day, MSCs were suspended in a pluronic F-127 hydrogel (15% PF-127 in Expansion Media) and injected into the cell reservoir of NICHEs to generate MSC-NICHEs (Appendix A2). MSCs permanence in NICHE was validated in a prior in vivo experiment in rats, which confirmed the presence of DiI-labeled MSCs immediately prior to and 6 weeks post-implantation (Appendix A2). For implantation of MSC-NICHEs, immunocompetent, 8-week-old male Wistar Furth rats were anesthetized using 2% isoflurane in 1.5. L of oxygen. Upon confirmation of absence of pedal withdrawal reflex, a subcutaneous pocket was created, and the MSC-NICHEs were aseptically implanted (1 per animal) in the right dorsum. The wound was closed using clips, and rats were allowed to recover under heat supplementation until motor skills were regained. Rats were monitored every day thereafter to confirm animal well-being.

For the vascularization study, sterile NICHEs (n=5 per group) were filled with 250,000 or 500,000 MSCs suspended in 15% PF-127 while vehicle controls were filled only with 15% PF-127. Six weeks post-implantation, rats were euthanized via CO_2 asphyxiation, NICHEs retrieved from the subcutaneous pocket, and processed for histology. For blood vessel quantification, four fields of view of each H&E-stained slides were captured at 200x magnification with an Olympus IX81 wide field

microscope (Olympus, Tokyo, Japan) by an individual blinded to the treatment groups. Blood vessel counting was performed by three independent scientists blinded to the treatment groups.

2.2.10 Immunosuppression and cell transplantation

Six weeks after NICHE implantation (pre-vascularization period), rats were randomized into 3 experimental groups: no-drug (Control), local (NICHE), and daily systemic (IP) immunosuppression. Rats in the control group received no CTLA4Ig. Rats in the NICHE group were loaded with 55 mg/mL CTLA4Ig (Orencia; Bristol-Myers Squibb) in the drug reservoir. Rats in the IP group received daily intraperitoneal (i.p.) injections (500 µg/day) of CTLA4Ig. Upon initiation of immunosuppression, 2×10^6 Leydig cells and 5×10^5 MSCs in a 1:1 Matrigel:PBS mixture were transcutaneously loaded in the NICHE cell reservoir of all rats using a 27G needle attached to a 1-mL syringe. To assess plasma CTLA4Ig levels, blood was collected from the saphenous vein before and every 4 days after initiation of CTLA4Ig treatment in heparinized tubes. Plasma was isolated via centrifugation. To assess tissue CTLA4Ig levels, NICHE, the fibrotic capsule and skin surrounding NICHE, liver, spleen, and kidneys were harvested and homogenized in T-PER buffer supplemented with protein inhibitor cocktail (Thermo Scientific). Tissue homogenates were clarified via centrifugation and stored frozen until analysis. CTLA4Ig in plasma and tissue homogenates was quantified using human CTLA4 ELISA (Invitrogen) following the manufacturer's instructions

2.2.11 In vivo cell tracking

Before and every 4 days after cell loading into the NICHE cell reservoir, cell viability and permanence within NICHE were assessed via bioluminescence in vivo imaging system (IVIS; Perkin Elmer). Briefly, rats received i.p. injections of 150 mg/kg D-Luciferin potassium salt solution (Gold Biotechnology). Thirty-four minutes later, anesthetized rats were imaged using bioluminescence IVIS spectrum with auto-exposure setting.

2.2.12 In vivo drug reservoir refillability assessment

NICHEs implanted in rats were transcutaneously loaded with CTLA4Ig-Alexa Fluor 647 conjugate and imaged via fluorescence IVIS with excitation and emission filters of 640 nm and 680 nm, respectively. Background threshold was obtained by acquiring an image of implanted empty NICHE prior to CTLA4Ig-Alexa Fluor 647 loading.

2.2.13 Histology analysis and blood vessel quantification

Upon harvesting, tissues were rinsed with PBS and fixed in 10% formalin for 48 h. Fixed tissues were dehydrated and cleared using standard ethanol and xylene washes followed by embedding with paraffin or Poly(methyl methacrylate) (PMMA) resin. Five µm sections were cut and stained with hematoxylin-eosin, Masson's Trichrome or Picro-Sirius red and visualized using an Olympus IX81 wide field

microscope (Olympus). For blood vessel quantification, 5 µm sections were stained with lectin from *Bandeiraea simplicifolia* following a published method [25]. Briefly, following deparafinization and rehydration, sections were blocked with 5% normal goat serum in 0.1% bovine serum albumin/tris buffered saline (BSA/TBS) for 1 h at room temperature (RT). Sections were incubated with biotinylated lectin (Sigma) in 0.1% BSA/TBS for 24 h at 4 ºC followed by streptavidin alkaline-phosphatase (Invitrogen) for 30 min at RT. Sections were developed with Warp Red Chromogen system (Biocare Medical, California, USA) and counterstained with hematoxylin. Visualization was performed using an Olympus IX81 wide field microscope (Olympus). For quantification, 12 fields of view per condition were photographed at 400x magnification and blood vessels manually counted. For each condition, 4-5 biological replicates were analyzed. For immunofluorescence staining, 5 µm sections were subjected to heat induced epitope retrieval in rodent decloaker buffer (Biocare Medical) at 121 ºC for 20 min followed by blocking in 5% normal goat serum for 1 h at room temperature. Primary antibodies were incubated for 16 h at 4 ºC in renaissance antibody diluent (Biocare Medical) and secondary antibodies for 1 h at room temperature in blocking buffer. Prolong Diamond mounting media with DAPI was added to preserve fluorescence (Invitrogen). Sections were visualized using a FluoView TM 3000 confocal microscope (Olympus). Antibodies used and dilutions are specified in table 1.

Table 1. List of antibodies

Target	Make	Cat. No.	Dilution
Lectin (*B. simplicifolia*) biotin conjugate	Sigma	L3759	1 µg/mL
RECA1	Santa Cruz	sc-52665	1:100
αSMA	Abcam	ab5694	1:100
Firefly Luciferase (CS17)	Invitrogen	35-6700	1:100
CD3 (SP7)	Invitrogen	MA1-90582	1:150
CD4	Invitrogen	PA5-87425	1:100
CD8 (OX-8)	Invitrogen	MA1-70003	1:100
CD45	Abcam	ab10558	1:100
anti-mouse (Alexa Fluor 647)	Abcam	ab150115	1:1000
anti-rabbit (Alexa Fluor 555)	Invitrogen	A-21428	1:200

2.2.14 Statistical analysis

Results are expressed as mean ± standard deviation. Statistical analyses were performed using Prism 8 software (GraphPad Software Inc., San Diego, CA, USA). Normality testing was performed and Student's t-test, One-way analysis of variance (ANOVA) or Two-way ANOVA were performed to determine statistical significance

of differences among groups. The sample sizes for in vivo studies were determined to provide statistical power of 80% to detect differences between groups. P values less than 0.05 were considered significant. Significance was indicated as follows: *, $p \leq 0.05$; **, $p \leq 0.01$; and ***, $p \leq 0.001$.

2.3 Materials and methods for chapter 5

2.3.1 Animal models
Eight-week-old male RNU or Fischer 344 were used as recipients and Lewis rats as donors (Charles River, Houston, TX, USA). All animals were maintained and used in conformity with guidelines established by the American Association for Laboratory Animal Science. Rats were kept in the Houston Methodist Research Institute animal facility. All procedures were approved by the Houston Methodist Institutional Animal Care and Use Committee in accordance with the National Institute of Health Guide for the Care and Use of Laboratory Animals and the Animal Welfare Act. Animals had access to food and water ad libitum.

2.3.2 Generation and implantation of NICHE with MSC
NICHE were fabricated as described in section 2.2.1. MSCs isolated from bone marrow of Fischer 344 rats were obtained from Cyagen at P2 and expanded in vitro using StemXVivo Mesenchymal Stem Cell Expansion Media (R&D Systems). NICHE loading with MSC hydrogel and implantation was performed as described in section 2.2.9.

2.3.3 Diabetes induction
Fischer 344 rats were injected intraperitoneally (i.p.) with 2 doses of streptozotocin (STZ; 40 mg/kg; Sigma) 3 days apart. To prevent dehydration, rats were provided Lactate Ringers Saline subcutaneously (2 mL/day) for 7 days starting on the day of first STZ injection. To prevent acute hypoglycemia, rats were provided 10% sucrose water ad libitum for 7 days starting on the day of first STZ injection. Blood glucose was monitored using a glucometer (AlphaTrak). Rats were considered diabetic after 3 consecutive blood glucose readings >300 mg/dL.

2.3.4 Islet isolation and transplantation
Lewis rats were overdosed with isoflurane immediately prior to pancreas harvesting. Pancreas were perfused through the pancreatic duct with 9 mL Clzyme RI collagenase (Vitacyte). Digestion was performed via static incubation in a water bath at 37C for 19 min and 40 seconds. Next, enzymatic activity was quenched by adding 20 mL of Hanks buffered saline (HBS) with 20% FBS and mechanical dissociation performed via vigorous shaking for 8 s. Tissue digest was washed 3 times with ice cold HBS and strained through a 500 μm wire mesh. The tissue pellet was re-suspended in 15 mL 1.096 g/cm^3 OptiPrep Density Gradient Medium (Sigma) and layered with 10 mL 1.068 g/cm^3 and 1.037 g/cm^3 OptiPrep and centrifuged at 1600

rpm 20 min with no break. Islets were collected at the 1.096 g/cm^3 and 1.068 g/cm^3 interphase, washed with HBS 3 times and cultured in RPMI-1640 media supplemented with 10% FBS, 1% penicillin/streptomycin, 20 mM HEPES, 5.5 mM glucose and 1 mM sodium pyruvate in a cell culture incubator set at 25°C and 5% CO_2.

For transplantation, islet doses were aliquoted into 15 mL falcon tubes and allowed to sediment (Appendix A3). An MSC-collagen hydrogel was prepared by re-suspending MSC in 4 mg/mL neutralized, thermo-responsive collagen hydrogel (RatCol, Advanced Biomatrix). Islet supernatant was carefully aspirated out without disturbing the islet pellet. Islets were re-suspended with MSC-collagen hydrogel using a wide tip and immediately loaded into a 1 mL syringe equipped with a 22G needle. The islet-MSC-hydrogel was immediately transcutaneously injected into NICHE cell reservoir through the silicone port. To prevent leakage, the needle was held in place for 1 min to allow for hydrogel polymerization.

2.3.5 Immunosuppression regimen and monitoring
Four weeks after NICHE implantation (pre-vascularization period), rats were loaded with 55 mg/mL CTLA4Ig (Orencia; Bristol-Myers Squibb) and 2 mg/mL anti-lymphocyte serum (ALS; Accurate Chemical Lot No. J2547) in the drug reservoir. For systemic immunosuppression reference, rats were injected i.p. with 10 mg ALS (0.5 mL). To assess plasma CTLA4Ig and ALS levels, blood was collected from the saphenous vein before and every 4 days after immunosuppression initiation in heparinized tubes. Plasma was isolated via centrifugation and analyzed using human CTLA4 ELISA (Invitrogen) and Rabbit IgG quantification kit (Invitrogen) following the manufacturer's instructions. Circulating T-Cells were quantified to assess systemic immunosuppression. Blood was collected from the saphenous vein into EDTA tubes. Staining solution was prepared with anti-CD45 (BD Cat No. 561867 at 1:80 dilution) and anti-CD3 (Invitrogen, Cat No. 12-0030-82 at 1:180 dilution) in 50 μL FACS buffer (PBS supplemented with 0.5% BSA and 5 mM EDTA). Staining solution was added to 100 μL whole blood and incubated for 30 min at RT. Next, samples were incubated with 1.8 mL of 1X 1-step fix/lyse solution (Invitrogen) for 10 min with rotation for erythrocyte lysis and cell fixation. Cells were washed twice, re-suspended in 300 μL FACS buffer, and 50 μL of CountBright Absolute Counting Beads (Invitrogen) were added to each sample. Samples were analyzed using a BD LSRII cell counter. T-Cell concentration was calculated using equation (4).

$$\textbf{T Cell Concentration} = \frac{\textbf{\# of cell events}}{\textbf{\# of bead events}} \times \frac{\textbf{beads/50 }\mu\textbf{L}}{\textbf{Sample volume}} \tag{4}$$

2.3.6 Intraperitoneal Glucose Tolerance Test
After overnight fasting, rats were injected i.p. with 3 g/kg of 50% dextrose solution (Northeast Medical Products). Blood glucose readings were obtained at baseline and at 15, 30, 60, 90, and 120 minutes post-injection with a glucometer (AlphaTrak).

2.3.7 In vitro glucose stimulated insulin release (GSIR).

Krebs buffered solution (KBS) was prepared with 115 mM NaCl, 24 mM NaHCO$_3$, 5 mM KCl, 1 mM MgCl$_2$, 0.1% BSA, 2.5 mM CaCl$_2$, and 25 mM HEPES. Low (LG) and high (HG) glucose KBS was supplemented with 2.8 mM or 16.7 mM glucose, respectively. After incubation with everolimus, CTLA4Ig, ALS or MSC, islets were transferred to 3 μm cell culture inserts in a 24-well plate and equilibrated with LG-KBS 1 h at 37°C. Next, inserts were transferred to 15 mL falcon tubes and centrifuged at 100g for 15 seconds. Inserts with islets were transferred to a clean 24-well plate and incubated with LG-KBS for 1 h at 37°C followed by incubation with HG-KBS for 1 h at 37°C. Samples were analyzed for insulin content via ELISA (Alpco) following the manufacturer's instructions. The stimulation index was calculated as the HG-to-LG insulin secretion ratio.

2.3.8 Histological analysis

Upon harvesting, tissues were fixed in 10% formalin for 48 h. Fixed tissues were dehydrated and cleared using standard ethanol and xylene washes followed by embedding with paraffin. Five μm sections were cut and stained with hematoxylin-eosin and visualized using an Olympus IX81 wide field microscope (Olympus). Blood vessels were stained with lectin from *B. simplicifolia* as described in section 2.2.9. For immunofluorescence staining, 5 μm sections were subjected to heat induced epitope retrieval in rodent decloaker buffer (Biocare Medical) at 121ºC for 20 min followed by blocking in 5% normal goat serum for 1 h at room temperature. Sections were incubated with rabbit anti-insulin (Cell Signaling, Cat No. 3014S, 1:500 dilution) for 16 h at 4ºC in renaissance antibody diluent (Biocare Medical) and AlexaFluor 555 goat anti-rabbit (Invitrogen, Cat No. A-21428; 1:200 dilution) for 1 h at room temperature in blocking buffer. Prolong Diamond mounting media with DAPI was added to preserve fluorescence (Invitrogen). Sections were visualized using a FluoView TM 3000 confocal microscope (Olympus). Imaging Mass Cytometry was performed in 5 μm sections at the Houston Methodist Research Institute ImmunoMonitoring Core following their standard procedures.

2.3.9 Statistical analysis

Results are expressed as mean ± standard deviation. Statistical analyses were performed using Prism 8 software (GraphPad Software Inc., San Diego, CA, USA). Normality testing was performed and Student's t-test, One-way analysis of variance (ANOVA) or Two-way ANOVA were performed to determine statistical significance of differences among groups. The sample sizes for in vivo studies were determined to provide statistical power of 80% to detect differences between groups. P values less than 0.05 were considered significant. Significance was indicated as follows: *, p≤0.05; **, p≤0.01; and ***, p≤0.001.

Chapter 3

Vascularization study

In this study, we sought to investigate a method to enhance vascularization of a 3D-printed, polymeric subcutaneously-implantable cell encapsulation platform [26]. We enriched our cell encapsulation device with platelet-rich-plasma (PRP) or Mesenchymal Stem Cells (MSCs) and implanted it in the subcutaneous space of rats and non-human primates (NHP). Device acceptability as well as amount, distribution, and maturity of penetrating blood vessels was assessed via histopathology analysis. Key aspects for a successful cell encapsulation device entail rapid and straightforward production, biocompatibility, and a readily available source of oxygen, nutrients and metabolites for transplanted cells. The platform described herein accomplishes these fundamental requirements.

3.1 Device fabrication

Additive manufacturing has found a niche in the field of tissue engineering and regenerative medicine as it allows for straightforward fabrication of bioengineered platforms. Specifically, fused deposition modeling (FDM) is compatible with a wide range of materials suitable for various applications including but not limited to dental, bone, neural, dermal, and soft tissue regeneration [27, 28]. The cell encapsulation device used herein was fabricated as two symmetrical structures via FDM using biocompatible PolyLactic Acid (PLA). The two structures were welded together to yield a hollow discoidal device with a diameter of 9 mm and a thickness of 2.5 mm (Fig. 1A). The hollow chamber in the device serves as a reservoir to house and confine transplanted cells. A circular port (1 mm in diameter) on the side of the device, sealed using biocompatible silicone, allows for hydrogel and cell loading. The device surface comprises of an array of square microchannels (nominally 100 μm x 100 μm) to allow blood vessel penetration into the reservoir.
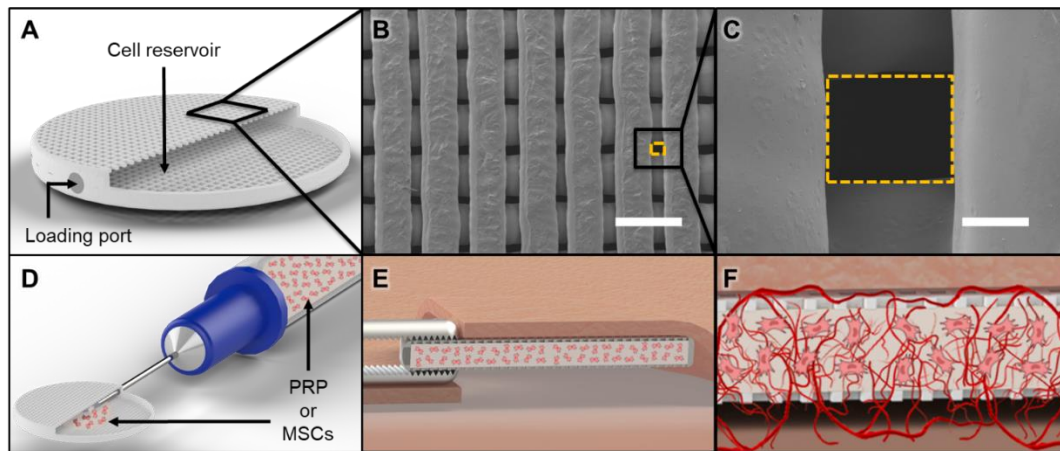

Fig. 1 Device design and deployment strategy. (A) 3D-rendering of encapsulation device depicting the cell reservoir and lateral loading port. (B) SEM imaging of microchannels indicated by black square in A. Scale bar represents 400 μm. (C) SEM imaging of a single 100 x 100 μm microchannel outlined in yellow. Scale bar represents 40 μm. Deployment strategy of the device as follows: (D) Platelet-Rich Plasma (PRP) or Mesenchymal Stem Cells (MSCs) are loaded into the cell reservoir

through the loading port ex vivo. (E) Loaded devices are implanted in a subcutaneous pocket. (F) PRP and MSCs stimulate vascularization of the cell reservoir.

Scanning electron microscopy (SEM) imaging of the device surface confirmed uniform fabrication of the microchannels with an average side length of 98.5 ± 18.5 μm throughout the structure of the device (Fig. 1B, C). We used PLA for its biocompatibility, mechanical characteristics, and low cost [29]. PLA is a biodegradable material with an average clearance time of 24 months after implantation.[30] In this timeframe, transplanted cells would have fully engrafted into the bioengineered microenvironment and the need for the polymeric structure could be obviated. If permanence is warranted, a bioinert polymer such as nylon could be used [31]. Nevertheless, manufacturing via FDM allows straightforward material substitution, tailoring to patient need based on cell transplant type. The deployment strategy for the device is as follows: 1) assembled devices are loaded ex vivo with PRP or MSC hydrogel via the loading port (Fig. 1D); 2) loaded devices are implanted in a subcutaneous pocket (Fig. 1E); 3) blood vessels penetrate into the device cell reservoir and form a dense vascular niche (Fig. 1F) at which point cells can be percutaneously loaded into the device to encounter a densely vascularized environment conducive to engraftment and long-term viability.

3.2 In vivo vascularization in rats driven by PRP or MSCs
The subcutaneous space is commonly deemed suboptimal for cell transplantation due to limited vascularization that results in graft anoxia and death [32, 33]. As such, pre-conditioning of the subcutaneous space to increase vascularization of the transplant microenvironment is a viable strategy for successful cell engraftment [20]. PRP contains a wide variety of growth factors including Vascular Endothelial Growth Factor (VEGF), Transforming Growth Factor β (TGF-β), and Platelet Derived Growth Factor (PDGF), which play key roles in driving angiogenic and wound healing responses [21, 34, 35]. MSCs produce autocrine and paracrine signals in the form of chemokines, cytokines, and growth factors that drive proangiogenic (i.e. VEGF, PDGF) and immunomodulatory (i.e. prostaglandin E2 (PGE2), interlukin-10 (IL10)) responses [36, 37]. To evaluate the effects of PRP and MSCs on driving vascularization into our encapsulation device, we implanted either PRP- or MSC-hydrogel filled devices in the subcutaneous space of rats. Devices filled with vehicle hydrogel were subcutaneously implanted in a cohort of rats as controls.

After 1 week of implantation, devices across all cohorts showed limited cell mobilization between the microchannels, while the reservoirs only had hydrogel remnants without quantifiable vessels (Appendix A4).
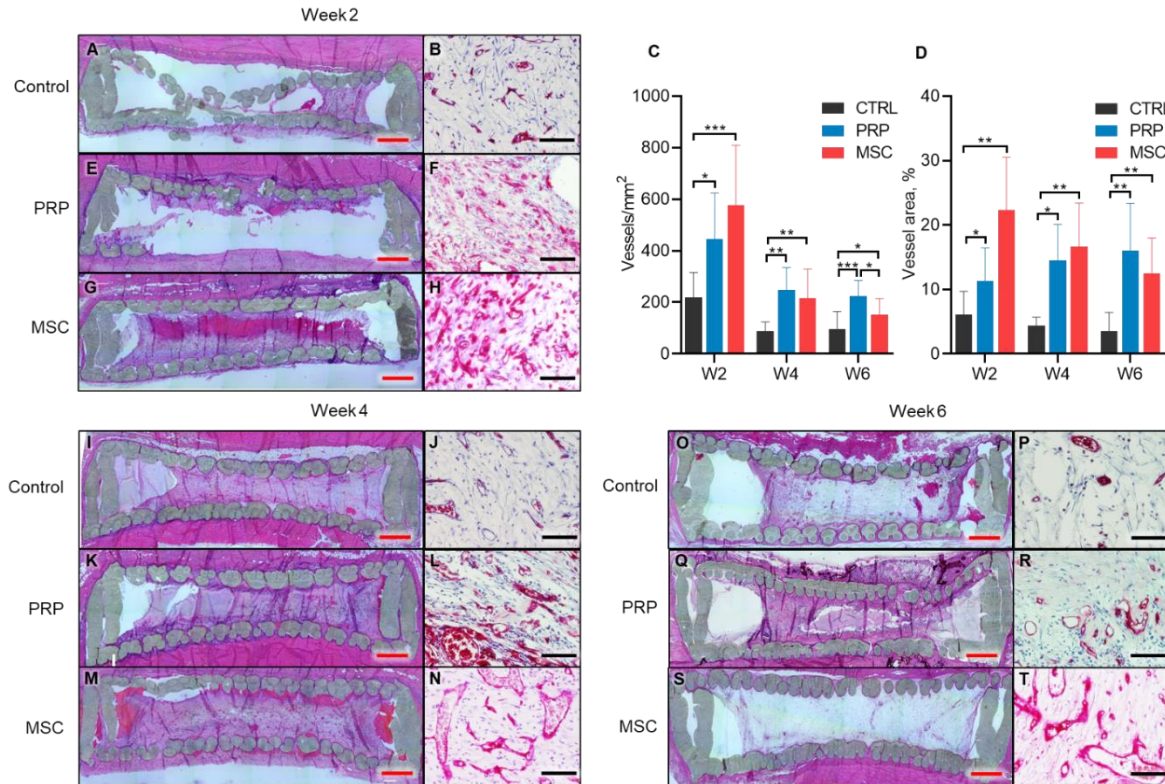
Fig. 2 Device vascularization in rats. 40X magnification of resin-embedded sections stained with H&E and 200X magnification of paraffin-embedded sections with blood vessels stained in red with lectin (BS-1). (A) H&E- and (B) BS-1-stained sections of control devices 2 weeks post-implantation. (C) Blood vessel density inside cell reservoirs throughout 6 weeks of implantation quantified from BS-1-stained sections. (D) Area of tissue comprised of blood vessels expressed as percentage of total tissue area per field of view. Mean ± SD; n=8-20 per condition; One-Way ANOVA with Tukey's multiple comparison test. *$P<0.05$; **$P<0.01$; ***$P<0.001$. Two week post-implantation sections of PRP devices stained with (E) H&E or (F) BS-1; and MSC devices stained with (G) H&E and (H) BS-1; Control devices with (I) H&E and (J) BS-1, PRP devices with (K) H&E and (L) BS-1, and MSC devices with (M) H&E and (N) BS-1 4 weeks post-implantation; Control devices with (O) H&E and (P) BS-1, PRP devices with (Q) H&E and (R) BS-1, and MSC devices with (S) H&E and (T) BS-1 6 weeks post-implantation. Red and black scale bars indicate 1 mm and 100 µm, respectively.

After 2 weeks of implantation, control (Fig. 2A, B) devices showed regional infiltration of vascularized tissue with quantifiable blood vessels (Fig. 2C, D). Implantation with PRP yielded similar amount, but significantly more vascularized, tissue penetration than control devices (Fig. 2E, F). Enrichment of devices with MSC yielded significant differences compared to controls or implantation with PRP. Cell reservoirs of the MSC devices had extensive tissue penetration from both surfaces with a migratory distribution that seemed to decrease in maturity as it approximated the center of the device, as suggested by the extensive RBC infiltration in that area (Fig. 2G).

Moreover, the penetrating tissue in MSC-loaded devices was thoroughly vascularized (Fig. 2H) with higher blood vessel density (577 ± 232 vessels / mm^2) than control (218 ± 97 vessels / mm^2) and PRP (446 ± 177 vessels / mm^2) groups (Fig. 2C). By week 4, control (Fig. 2I, J) and PRP (Fig. 2K, L) devices had comparable tissue penetration spanning ~2/3 of the cell reservoir, but the PRP cohort was significantly more vascularized. By this time point, the MSC group had tissue ingrowth spanning the entirety of the device and ~2.5-fold more vessel density than control devices (Fig. 2M, N). Complete colonization of the device is important as ingrown tissue would provide mechanical support to the device and additional protection to cells housed within. Histological sections of MSC devices consistently showed bleeding inside the cell reservoir at the interphase between tissue and polymer. This bleeding pattern may be attributable to tissue injury at time of explant secondary to decompression of the device, further underscoring extensive vascularization of MSC devices. By week 6 of implantation, ~3/4 of control (Fig. 2O, P) and PRP (Fig. 2Q, R) cell reservoirs were filled with tissue, but PRP devices remained significantly more vascularized. MSC devices were completely filled with tissue and had higher vessel density compared to control (Fig. 2S, T).

Overall, the strongest angiogenic response was observed at 2 weeks post-implantation in both PRP and MSC devices where tissue inside the reservoirs was extensively colonized by small capillaries. The blood vessel density decreased across groups by 4 weeks post-implantation; however, the area of tissue occupied by blood vessels stayed constant throughout the six-week study (Fig. 2D). This may be explained by dynamism in the wound healing response. At early time points, the vascular component of the penetrating tissue was mainly comprised of small, sprouting capillaries, characteristic of granulation tissue. As the wound healing response was resolved, many capillaries regressed and those remaining matured into larger, likely permanent, vessels. In sum, the number of vessels was reduced but the effective area covered by vascular tissue, and ultimately permeated with oxygen and nutrients, remained nearly constant. Mature, permanent vessels are of importance as these would maintain the graft long-term. Enrichment with PRP and MSC not only increased the initial angiogenic response with numerous infiltrating capillaries but also enhanced their maturation and permanence. It is noteworthy that, throughout the six week study, the percentage of tissue comprised of blood vessels in PRP and MSC devices (Fig. 2D) was comparable to that reported in islets transplanted under the kidney capsule (~10% of area covered by vessels) [38, 39], a gold standard transplant site in rodent models [40].

The various degrees of vascularization achieved with PRP and MSC enrichment throughout time revealed potential transplantation windows that may be exploited depending on cell type. For example, in the case of pancreatic islets, enrichment with MSC and transplantation at 2 weeks post-implantation might be ideal as the high capillary density and nearly complete tissue ingrowth could provide support to the islet mass while avoiding overcrowding. Moreover, intra-islet capillary re-anastomosis upon transplantation is paramount for successful islet engraftment [41]. In this context, the numerous sprouting vessels observed at week 2 may be harnessed as a readily available pool of capillaries to achieve islet vascular re-anastomosis. Subsequently, the tissue in the device would mature in tandem with

the transplant, creating a specialized environment suitable for long-term engraftment. Transplantation of other cell types that benefit from a denser matrix for engraftment, such as Leydig cells [42], may benefit from a longer pre-vascularization period, namely 4 weeks. It has to be noted that underlying pathologies, such as diabetes [43], may impair angiogenesis and therefore the timeframe for optimal vascularization could be different and would need to be assessed.

3.3 Device tolerability in rats

The discoid shape of the device was chosen to optimize biointegration by reducing sharp edges and maximizing surface contact with the surrounding tissue [44]. Successful biointegration of the cell encapsulation device is paramount for transplanted cell survival. Thus, in parallel to vascularization assessment, device tolerability was evaluated in rats for all groups. At 1-week post-implantation, control devices showed a thin layer of monocytes adhered to the surface of the material and immediately distal to it, formation of highly cellular granulation tissue with fibroblasts, monocytes and capillaries (Fig. 3A). By week 2 post-implantation, the granulation tissue appeared more organized with lower cellularity and higher collagen fiber deposition and alignment than at week 1 (Fig. 3B). By week 4, a thin, collagenous fibrotic capsule was in place, suggesting resolution of the foreign body reaction (FBR) to the device material (Fig. 3C).
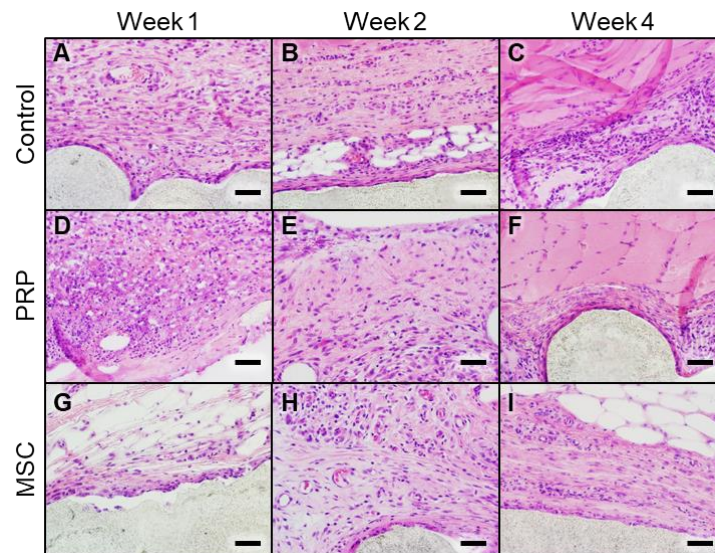

Fig. 3 Reactivity to the implant in rats. H&E stained sections of tissue around control devices (A) 1, (B) 2, and (C) 4 weeks post-implantation; PRP devices (D) 1, (E) 2, and (F) 4 weeks post-implantation; and MSC devices (A) 1, (B) 2, and (C) 4 weeks post-implantation. Scale bars represent 50 µm.

Overall, control devices elicited a classic FBR to biocompatible materials that was limited and resolved within 4 weeks of implantation [45], underscoring that the

geometry and material employed in our devices were well tolerated. Addition of PRP augmented the FBR to the device at early time point, probably due to release of growth factors and chemotactic cues that stimulate angiogenesis, fibroblast expansion, and immune cell recruitment [46, 47]. Notably, at 1-week post-implantation, PRP devices showed platelets in the subcutaneous space adjacent to the devices, likely due to platelet escape from the degrading PRP hydrogel (Fig. 3D). Escaped platelets were surrounded by highly cellular and disorganized granulation tissue comprised of macrophages, fibroblasts, and capillaries. However, by 2 weeks post-implantation, the granulation tissue was more organized, showing premature fibroblast alignment, collagen deposition, and decreased cellularity compared to week 1 (Fig. 3E). By 4 weeks post-implantation, PRP devices were surrounded by an organized, thin fibrotic capsule, indicating biointegration and resolution of FBR to the material (Fig. 3F). Similar to control and PRP groups, MSC devices had a thin layer of mononuclear cells adhered to the surface of the material 1 week post-implantation (Fig. 3G). However, the granulation tissue formation was notably reduced compared to the other groups. This difference in reaction may be attributed to the immunomodulatory properties MSCs exert by secreting PGE2, IL-10, nitric oxide (NO), indoleamine 2,3-dioxygenase (IDO), among other cues that drive anti-inflammatory response [37]. After 2 weeks of implantation, MSC devices showed granulation tissue formation with cellularity and organization similar to that observed on weeks 1 and 2 of control and PRP devices, suggesting a delayed and ameliorated response to the material (Fig. 3H). Moreover, the FBR formed around MSC devices was highly colonized by capillaries which correlated temporally with profuse vessel penetration into the devices (Fig. 2L, M). By 4 weeks post-implantation, MSC devices were surrounded by a thin, organized fibrotic capsule comprised of aligned collagen fibers, dispersed fibroblasts, and blood vessels (Fig. 3I). Overall, the device elicited a limited foreign body reaction that resolved by 4 weeks post-implantation across all groups, indicating adequate biointegration and biocompatibility. Encapsulation devices that rely on diffusion for nutrient and oxygen delivery to transplanted cells are typically affected negatively by FBR, where fibrotic capsule formation around the material increases thickness and hampers solute diffusion [48]. In our encapsulation device, although initiation of a limited FBR resulted in a thin and organized fibrotic capsule, the penetrating blood vessels into the reservoir provide necessary oxygen and nutrients. In fact, a thin fibrotic capsule is beneficial as it anchors the device to the subcutaneous space, reducing irritation secondary to device displacement [49]. Moreover, we previously demonstrated our device is non-cytotoxic and maintains function of various cell types including stem-cell-derived insulin-producing cells [50], islets [51, 52], and Leydig cells [21]. Taken together, these results underscore our device holds potential for successful cell transplantation.

3.4 In vivo vascularization in non-human primates.

Aiming at clinical translation of the technology, we sought to investigate if enrichment with PRP and MSCs would yield similar results in NHP to those obtained in rats. NHP response would more closely mimic that of humans, representing a superior model for translation efforts.

Subcutaneous implantation of control, PRP or MSC devices elicited a mild FBR with infiltration of small capillaries and few inflammatory cells lining the polymer structure. The reaction was limited throughout 4 weeks of implantation (Appendix A5). In terms of vascularization, at 1-week post-implantation, mobilization of cells with collagen deposition was visible across the microchannels in all groups, but only hydrogel occupied the reservoirs (Appendix A4). At 2 weeks post-implantation, control devices had limited tissue colonization (Fig. 4A, B) with few quantifiable blood vessels (Fig. 4C, D).
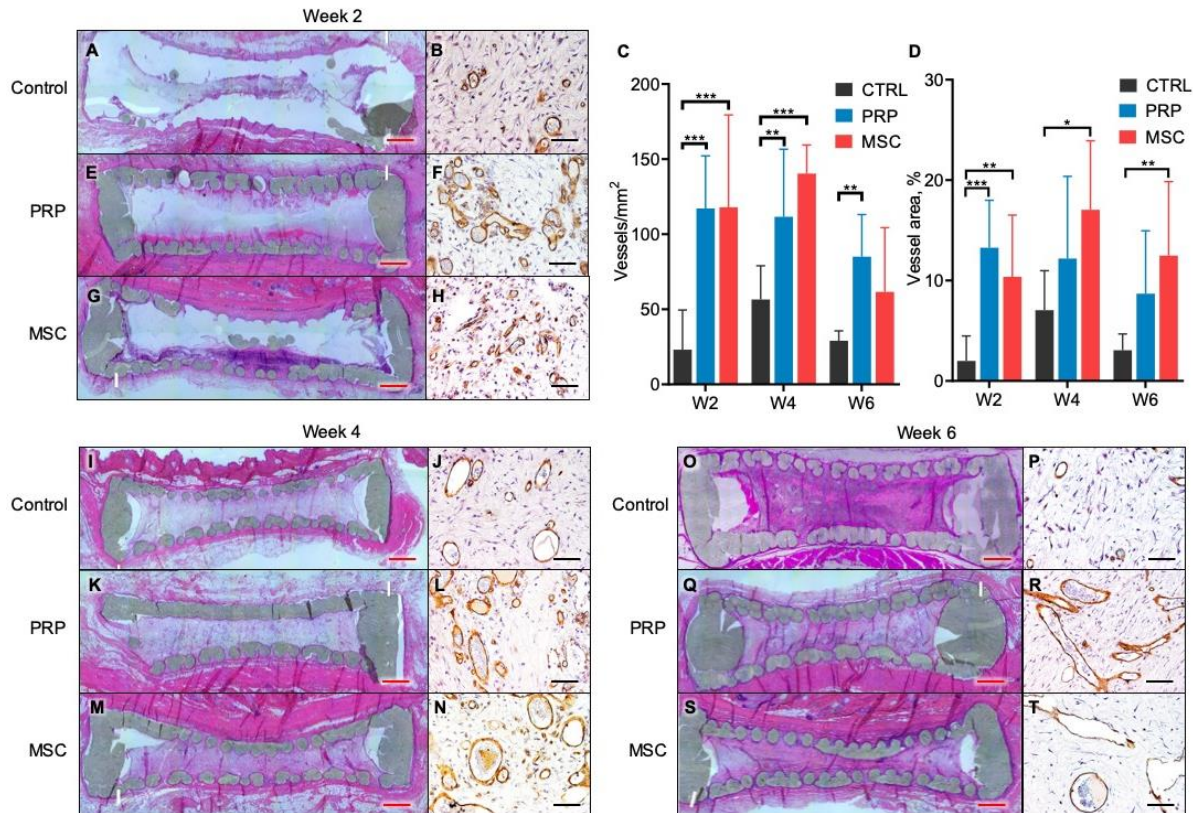

Fig. 4 Device vascularization in NHP. 40X magnification of resin-embedded sections stained with H&E and 200X magnification of paraffin-embedded sections with blood vessels stained in brown (CD31). (A) H&E- and (B) CD31-stained sections of control devices 2 weeks post-implantation. (C) Blood vessel density inside cell reservoirs throughout 6 weeks of implantation quantified from CD31-stained sections. (D) Area of tissue comprised of blood vessels expressed as percentage of total tissue area per field of view. Mean ± SD; n=8-12 per condition; One-Way ANOVA with Tukey's multiple comparison test. *P<0.05; **P<0.01; ***P<0.001. Two week post-implantation sections of PRP devices stained with (E) H&E or (F) CD31; and MSC devices stained with (G) H&E and (H) CD31; Control devices with (I) H&E and (J) CD31, PRP devices with (K) H&E and (L) CD31, and MSC devices with (M) H&E and (N) CD31 4 weeks post-implantation; Control devices with (O) H&E and (P) CD31, PRP devices with (Q) H&E and (R) CD31, and MSC devices with (S) H&E

and (T) CD31 6 weeks post-implantation. Red and black scale bars indicate 1 mm and 100 µm, respectively.

PRP (Fig. 4E, F) and MSC (Fig. 4G, H) devices had marginal tissue penetration. Albeit the amount of tissue was limited, the vascular density in PRP and MSC devices was 5 times higher (117 ± 35 and 118 ± 61 vessels / mm^2, respectively) than controls (23 ± 26 vessels / mm^2) (Fig. 4C). By 4 weeks post-implantation, devices were largely filled with connective tissue across all groups. Control devices showed increased vascularization compared to week 2 (Fig. 4I, J). PRP (Fig. 4K, L) and MSC (Fig. 4M, N) devices remained significantly more vascularized, with vessel densities similar to the previous time point (Fig. 4C). By week 6, devices across all groups remained fully colonized by tissue (Fig. 4O, P) with higher vessel densities in PRP (Fig. 4Q, R) and MSC (Fig. 4S, T) groups. Overall, enrichment of our encapsulation device with PRP and MSC prior to implantation in NHP resulted in increased blood vessel density. Similar to what was observed in rats, NHP exhibited the strongest angiogenic response was observed at two weeks post-implantation, which remained stable up to week 4. The non-significant drop in vessel density observed at week 6 across groups may be explained by regression of small, immature capillaries, as suggested by unchanged vessel area across time points (Fig. 4D). The similarity in results between rats and NHP underscores promise for device translatability.

3.5 Regional vessel quantification
To further characterize the vascularization inside the devices, we investigated the spatial distribution at 4 weeks post-implantation, when vessel density stabilized, for rats and NHPs. To achieve this, we divided the device into three sections, namely top, middle, and bottom, as displayed in Fig. 5A. In rats, control devices had a homogeneous distribution of blood vessels throughout the cell chamber (about 33% per region) (Fig. 5B). PRP devices had the highest vessel accumulation at the bottom (50.64 ± 10.33%), followed by the middle region (29.38 ± 5.41%), and least amount at the top (19.98 ± 5.10%). In contrast, MSC devices had the highest vessel accumulation in the middle region of the device (47.78 ± 6.16%), followed by the bottom (35.80 ± 2.52) and the least amount at the top (16.42 ± 5.13%). In NHP, control and PRP-treated devices had the majority of vessels conglomerated in the middle of the device (73.60 ± 18.65% and 50.65 ± 10.90%, respectively), whereas MSC had an even distribution between middle and bottom regions of the device (about 45% each) (Fig. 5C). Overall, PRP and MSC devices had an asymmetrical vessel distribution, indicating these treatments elicited a stronger angiogenic response from the tissue closer to the muscle than the subcutaneous space. We attribute this polarization to the intrinsic muscle architecture responsive to vasculogenic cues. Muscle tissue has a high metabolic demand and, as such, requires a rich vascular supply [53]. This inherently dense capillary network provides an enriched pool of vascular components (i.e. endothelial cells, smooth muscle cells, and pericytes) able to respond to pro-angiogenic cues delivered by PRP and MSCs [54]. In fact, Li et al., demonstrated that implanting PRP/MSC-enriched

demineralized bone matrix enveloped in a muscle flap significantly increased construct vascularization [55].
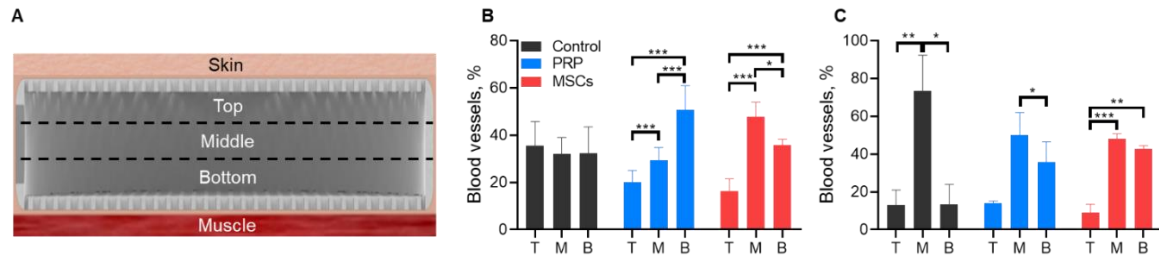

Fig. 5 Blood vessel distribution in rats and NHP. (A) Schematic of device division for regional quantification of blood vessels. Distribution of blood vessels in top (T), middle (M), and bottom (B) regions at 4 weeks post-implantation in (B) rats and (C) non-human primates. Mean ± SD; n=2-6 per condition; One-Way ANOVA with Tukey's multiple comparisons test. *P<0.05; **P<0.01; ***P<0.001.

3.6 Evaluation of blood vessel maturity.

Blood vessel maturity is paramount to ensure adequate nutrient and oxygen delivery to the transplanted cells. As such, we evaluated if enrichment with PRP and MSCs would have an effect on the maturity of blood vessels penetrating into the device at 4 and 6 weeks post-implantation. These time points were selected based on amount of tissue colonization of the cell reservoirs and expectation of blood vessel maturity. To this end, we immunolabeled sections of the device with an endothelial marker (CD31) to identify vascular structures, whereas endothelial nitric oxide synthase (eNOS) was used as a marker of vessel maturity and function. Isotype control staining of tissue collected from devices implanted in rats revealed background autofluorescent foci from RBC in red and green channels, which helped to discriminate positive staining from autofluorescence (Appendix A6). At 4 weeks post-implantation, control (Fig. 6A) devices revealed vascular structures with marginal eNOS staining. In contrast, PRP (Fig. 6B) and MSC (Fig. 6C) devices showed increase in eNOS positive staining, indicating a higher degree of maturity than the control group (Fig. 6D).
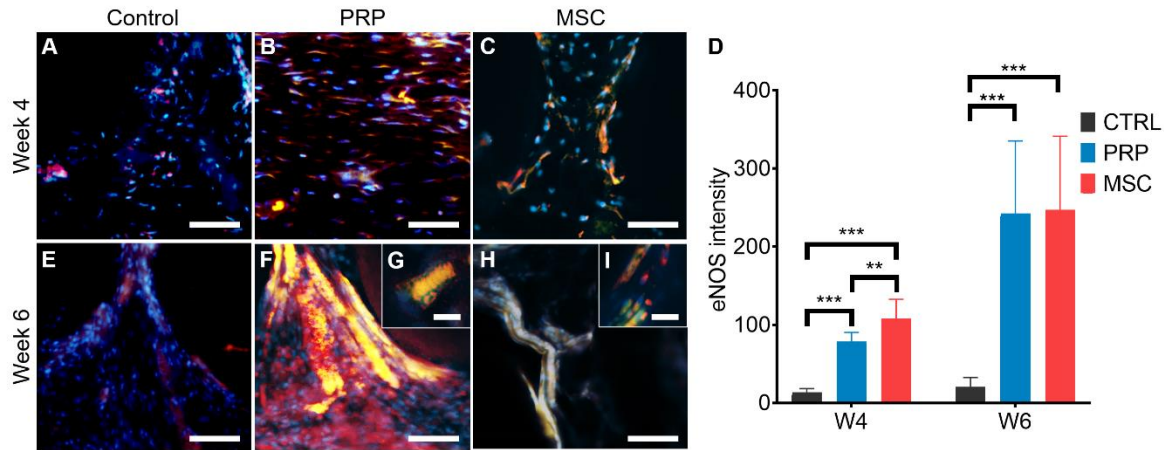
Fig. 6 Blood vessel maturity in rats. Merged images of CD31 (red), eNOS (green), and DAPI (blue) immunolabeling of tissues collected from (A) control, (B) PRP, and (C) MSC devices 4 weeks post-implantation. (D) eNOS intensity quantification as a marker of vessel maturity at 4 and 6 weeks post-implantation. Mean ± SD; n=9/condition. One-Way ANOVA with Tukey's multiple comparisons test. **$P<0.01$; ***$P<0.001$. Tissue collected 6 weeks post-implantation from (E) Control, (F-G) PRP, and (H-I) MSC devices labeled with CD31 (red), eNOS (green), and DAPI (blue). Scale bars represent 25 μm. (G, I) Magnification of F and H, respectively. Scale bars represent 15 μm.

At 6 weeks post-implantation, vessels in control devices stained marginally for eNOS (Fig. 6D, E), similar to week 4. PRP devices had extensive colonization with numerous patent blood vessels and autofluorescent RBCs in the lumen (Fig. 6F). High magnification imaging of these structures showed the endothelial-cell lining stained positively for CD31 and eNOS co-expression in a characteristic punctate pattern as well as membrane bound, stacked RBCs in the lumen (Fig. 6G) [56, 57]. At 6 weeks, MSC devices had mature, branching blood vessels with consistent eNOS expression (Fig. 6H-I) that was significantly higher than controls (Fig. 6D).

In NHP tissues, isotype staining revealed RBC autofluorescence across all groups (Appendix A6). At 4 weeks post-implantation, control devices had identifiable vascular structures with limited eNOS expression (Fig. 7A). In contrast, PRP (Fig. 7B) and MSC (Fig. 7C) devices had consistent eNOS expression, indicating a significantly higher level of maturity than the control group (Fig. 7D). At 6 weeks post implantation, eNOS staining remained limited in control devices (Fig. 7E). PRP devices had strong eNOS labeling in branching vessels (Fig. 7F). Similarly, MSC devices exhibited strong eNOS expression in the lining of blood vessels (Fig. 7G), albeit significantly lower than the PRP group (Fig. 7D).
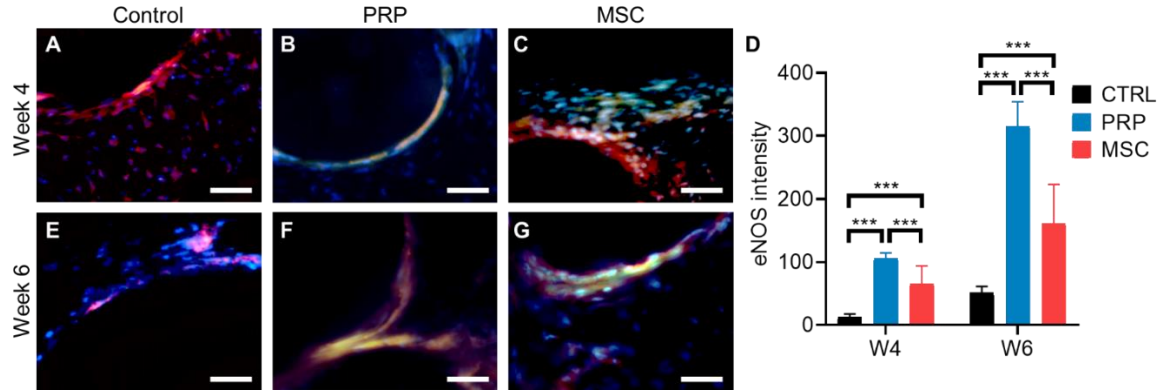
Fig. 7 Blood vessel maturity in NHP. Merged images of CD31 (red), eNOS (green), and DAPI (blue) immunolabeling of tissues collected from (A) control, (B) PRP, and (C) MSC devices 4 weeks post-implantation. (D) eNOS intensity quantification as a marker of vessel maturity at 4 and 6 weeks post-implantation. Mean ± SD; n=9/condition. One-Way ANOVA with Tukey's multiple comparisons test. ***$P<0.001$. Sections of tissue collected 6 weeks post-implantation from (E) Control, (F) PRP, and (G) MSC devices labeled with CD31 (red), eNOS (green), and DAPI (blue). Scale bars represent 50 µm.

Overall, PRP and MSCs increased vessel density and maturity in our devices across species. The slight variation in the effects of PRP and MSCs between rats and NHP is likely attributable to dissimilar composition between species. For the studies presented in this manuscript, standard levels of platelets and MSCs were used to enhance the wound healing response. However, it has been documented that, even in the case of consistent concentrations of platelets, red blood cells, fibrinogen levels, and active TGF-β1, the amount of VEGF-A, PDGF and white blood cells in PRP may vary substantially between donors [58, 59]. Moreover, although PRP and MSC based therapies perform similar functions in enhancing wound healing response, their mechanisms are different [60]. PRP serves as a finite reservoir of growth factors that are passively released as they diffuse from the carrier [61]. MSCs, on the other hand, are plastic cells that produce trophic factors in response to paracrine signals in the microenvironment. As a result, trophic factors are produced in an orderly fashion conducive to sequential vessel sprouting and remodeling, as needed [62]. Additionally, MSC transdifferentiation potential allows them to acquire endothelial or pericyte-like phenotypes and provide support to newly formed blood vessels, further contributing to vessel maturation [63].

The difference in mechanism by which PRP and MSC stimulate angiogenesis could be leveraged to further potentiate vascularization in the context of device scale-up (for clinical use) or implantation in patients with compromised vasculogenic response (e.g. diabetic patients). We speculate that co-implantation of devices with PRP and MSCs would augment the vascularization response. In this setting, release of pro-angiogenic growth factors from PRP would not only drive migration of endogenous vessels into the device, but also directly stimulate co-implanted MSCs to adopt an endothelial-pericyte phenotype for vessel remodeling. In this sense, rather than

depending merely on wound healing cues from the host, MSCs would be primed in a growth factor-rich milieu. We posit that this synergistic approach would provide a densely vascularized niche conducive to long-term cell engraftment and function. Moreover, PRP is already approved for use in the clinic and MSCs have undergone numerous clinical trials that underscore their safety and efficacy [64-66], allowing for straightforward adaptability and translatability of our platform. The combination of PRP and MSCs into a single platform, as well as oxygenation assessment of the cell reservoir, will be the subject of our future study.

The geometry, materials, and deployment strategy of our encapsulation platform promoted rapid biointegration with minimal FBR. Moreover, the immunomodulatory effect of MSCs was highlighted by delayed and limited FBR to these devices. Both PRP and MSCs drove extensive vascularization of cell reservoirs in rats and NHP. However, enrichment with MSCs expedited vessel maturation across species. A combinatorial approach with implantation of devices enriched with both PRP and MSCs could provide a synergistic effect to further potentiate the angiogenic response. We unveiled a promising window for cell transplantation at 2 weeks that would provide grafts with sufficient mechanical support, oxygen, and nutrients. In conclusion, we effectively enhanced the vascularization of our encapsulation device using PRP and MSCs, creating a subcutaneous microenvironment promising for successful cell transplantation.

Chapter 4

NICHE efficacy study

To date, no cell encapsulation systems are available that integrate the following critical features for long-lasting cell engraftment: 1) an environment conducive to efficient mass transport (of oxygen, nutrients, therapeutic factors, etc.); 2) protection from host immune rejection via local immunosuppressant delivery; 3) biocompatibility and robust mechanical stability for long-term deployment; 4) ease of cell loading, cell and immunosuppressant replenishing, and device retrieval in the event of medical complications; and 5) scalability to achieve clinically relevant encapsulation capacity for delivery of sufficient cell mass.

In efforts to acquire a transformative approach for cell encapsulation, we developed a cell transplantation system encompassing all the above-mentioned critical features [26]. Our system, termed "neovascularized implantable cell homing and encapsulation" (NICHE) is a dual-reservoir encapsulation platform integrating in situ pre-vascularization and local immunosuppression. NICHE deployment first entails creating a vascularized environment. To achieve this, NICHE is preloaded with a hydrogel containing mesenchymal stem cells (MSCs) and subcutaneously implanted (Fig. 8A). MSCs produce paracrine growth and angiogenic factors, which potentiate angiogenesis and subcutaneous tissue penetration into the cell reservoir [63, 67]. After pre-vascularization (Fig. 8B), immunosuppressant is transcutaneously loaded into the drug reservoir for local release to establish an immune-suppressed milieu (Fig. 8C). Finally, cells are transcutaneously transplanted into the cell reservoir of the preconditioned NICHE, which is a highly vascularized, immunoprotected environment conducive for engraftment (Fig. 8D).
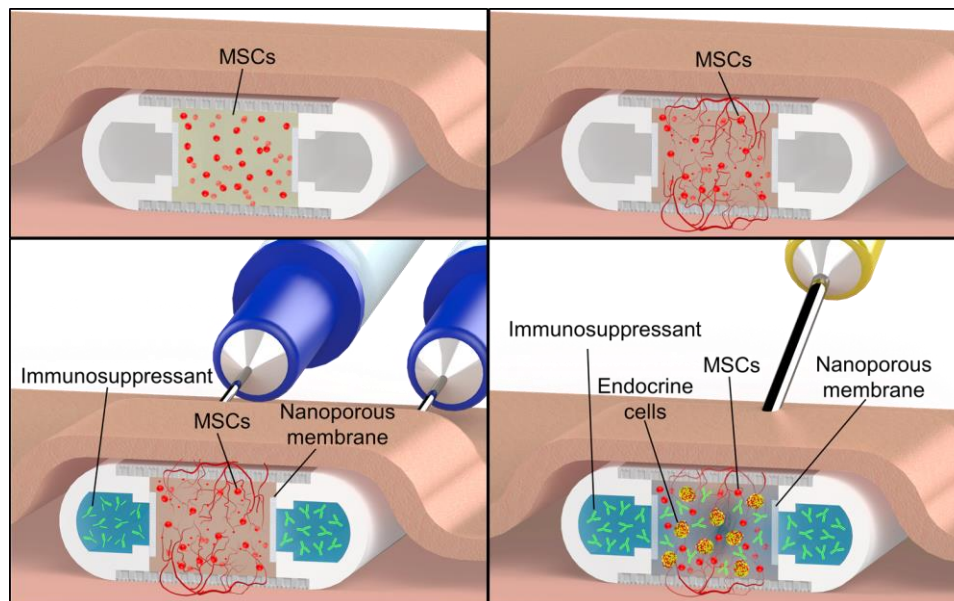

Fig. 8 NICHE deployment strategy. (A) Mesenchymal Stem Cells (MSCs) hydrogel-filled NICHE is implanted in a subcutaneous pocket to stimulate vascularization. (B) Pre-vascularization phase, with blood vessel formation across

the cell reservoir. (C) Transcutaneous loading of immunosuppressant into NICHE drug reservoir using loading and venting needles. Needles are advanced into the NICHE drug reservoir through self-sealing silicon ports (visible in Fig. 9). Upon drug loading, the venting needle permits flushing of the reservoir and removal of entrapped air or liquid. (D) Transcutaneous transplantation of cells into the vascularized and immunosuppressed cell reservoir using a needle connected to a cell-loaded syringe.

4.1 NICHE fabrication and loading

To integrate both in situ prevascularization and local immune-suppressant delivery into an encapsulation platform, NICHE was developed as a dual reservoir system. A central cell reservoir is surrounded by a '*U*'-shaped drug reservoir that sustainably elutes immunosuppressant through two nanoporous nylon membranes (Fig. 9A). The drug reservoir, which serves as the backbone of the NICHE, is fabricated using selective laser sintering (SLS) in biocompatible nylon (PA 2200). Additive manufacturing permits rapid scalability and flexibility for device size and geometry customization. The drug reservoir has two longitudinal 2.3 mm x 15 mm rectangular windows (Fig. 9A) on either side of the cell reservoir. Two nanoporous nylon membranes are affixed onto the rectangular windows using biocompatible silicone glue (Fig. 9B). Two biocompatible silicone plugs on the '*U*'-shaped drug reservoir serve as the loading and venting ports for transcutaneous drug replenishment. A two-layered woven nylon mesh system encloses the cell reservoir (Fig. 9D): an inner 300 µm x 300 µm nylon mesh provides mechanical support, while an outer 100 µm x 100 µm nylon mesh allows for blood vessel penetration and cell retention [21]. Importantly, SEM imaging of woven meshes and nanoporous membranes obtained from NICHE after implantation in rats for 10 weeks showed material integrity remained intact (Fig. 9B-E). We observed collagenous tissue colonization of the woven mesh openings after implantation, which further contributes to cell retention in NICHE (Fig. 9E).
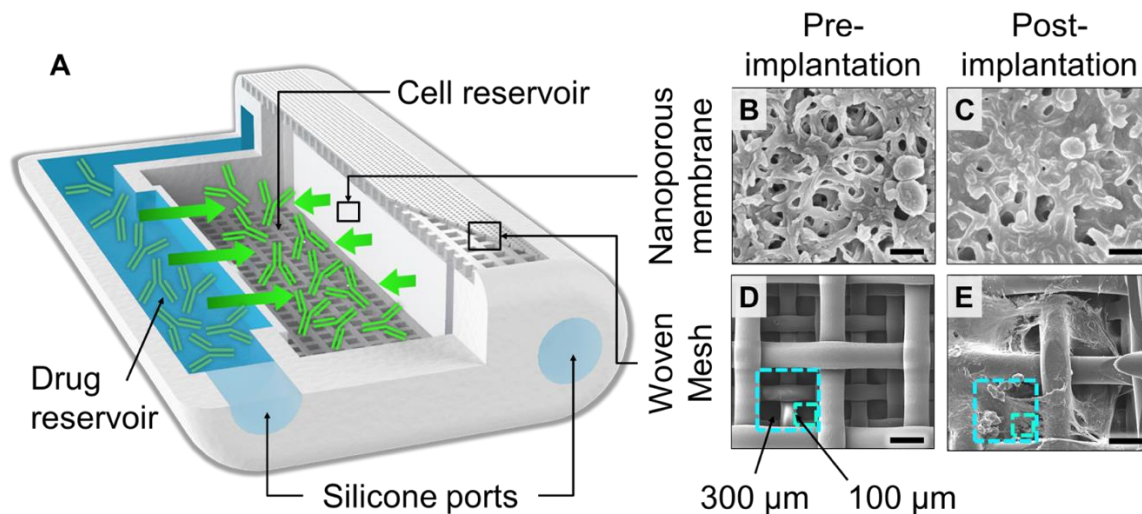
Fig. 9 NICHE design. (A) Rendering of NICHE showing the cell and drug reservoir as well as the loading ports. SEM image of nylon nanoporous membrane before (B) and after (C) implantation. Scale bars represent 1 μm. SEM image of the two-layer nylon woven mesh before (D) and after (E) implantation. Scale bars represent 150 μm.

While the NICHE can be implanted anywhere in the body, including the omentum, we focused on subcutaneous implantation, which facilitated straightforward and minimally invasive transcutaneous loading of cells and drug into the respective reservoirs. Loading of the drug reservoir was achieved by advancing needles through the skin and the silicon ports. One needle served for drug loading, while the other vented out air or excess drug solution. This configuration prevents chance of nanoporous membrane puncture. Cell loading is performed by advancing a needle through the skin and nylon meshes, and into the cell reservoir. Finally, the internal wall of the cell reservoir serves as a backstop and landmark, ensuring cells are dispersed within the cell reservoir.

4.2 PA 2200 degradation and biocompatibility
As NICHE is intended for long-term deployment, we sought to investigate material stability in vitro. To this end, we assessed degradation of PA 2200 (the material of NICHE structure) through specimen weight change in vitro over time at 37 °C in PBS. We observed a 0.5% increase in the weight of the device at 1 week of incubation (Fig. 10A). The weight continued to steadily rise at a rate of 0.1% per week for up to 8 weeks. Thereafter, up to a total 1.5% weight increase was detected at 32 weeks (0.01% per week). We attribute this weight increase to water absorption by the material, in line with literature reports for PA 2200 (otherwise known as PA12) [68, 69].
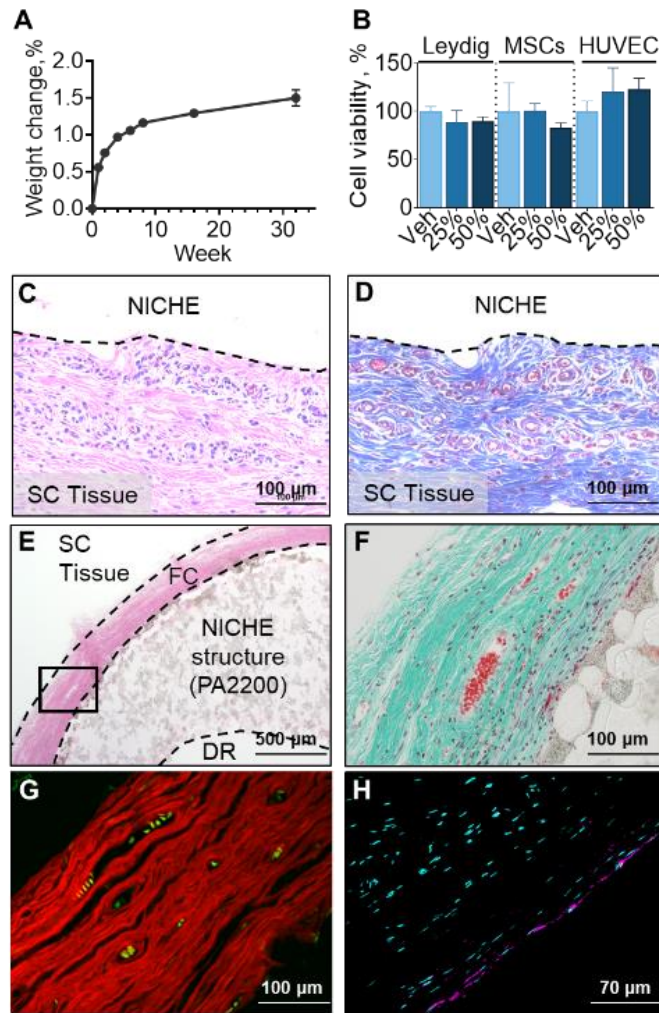
Fig. 10 NICHE characterization and biocompatibility. (A) In vitro degradation test of NICHE structure. (B) Viability of Leydig cells, Mesenchymal Stem Cells (MSCs), and Human Umbilical Vein Endothelial Cells (HUVEC) after incubation with NICHE extract in media or media alone as vehicle (Veh). Mean ± SD. One-way ANOVA. FFPE sections of subcutaneous tissue in direct contact with NICHE at 10 weeks post-implantation stained with (C) Hematoxylin and Eosin (H&E) and (D) Masson's Trichrome (MT). Dotted line indicates NICHE-SC tissue intersection. (E) Poly-methyl methacrylate embedded sections of NICHE implanted for 10 weeks stained with H&E. "NICHE structure" refers to the 3D-printed portion of NICHE, namely the PA2200 polymer. Square indicates area of the fibrotic capsule magnified and stained with MT in (F). Fluorescence imaging of fibrotic capsule sections stained with (G) Picro-Sirius Red and with (H) pan-leukocyte marker (CD45 in magenta; DAPI in cyan). Green autofluorescence from red blood cells highlights vascular component of the fibrotic capsule in G. FFPE: Formalin-fixed, paraffin embedded; SC: subcutaneous; FC: Fibrotic capsule; DR: Drug Reservoir.

To assess biocompatibility of NICHE, we performed cytotoxicity studies with representative cell lines relevant to our deployment strategy as well as through in vivo implantation in rats. Cytotoxicity of NICHE was evaluated via MTT cell viability assay in Leydig cells, MSCs and HUVECs as representatives of model of endocrine cells for transplantation, stem cells for local angiogenesis and immune modulation, and endothelial cells involved in the formation of the vascular network, respectively. Cells incubated in NICHE extract maintained comparable viability to those incubated with media only (Veh) (Fig. 10B). This indicates that NICHE does not have a direct toxic effect, nor does it affect any processes important for mammalian cell survival. To further characterize the biocompatibility of NICHE, we performed an in vivo implantation test in the subcutaneous tissue of rats. Histological evaluation of subcutaneous tissue in direct contact with NICHE collected after a ten-week implantation period showed a marginal foreign body reaction characterized by granulation tissue with neovessel formation and without chronic inflammation, exacerbated fibrosis, giant cell or mast cell infiltration (Fig. 10C-D). Typical of medical device implantation, a fibrotic capsule formed around NICHE at the interphase between the polymer and the subcutaneous (SC) tissue (Fig. 10E). The capsule was of moderate thickness (351.92 ± 81.69 µm) and mainly comprised of a dense and organized collagenous matrix with scattered blood vessels (Fig. 10E-F and Appendix A7). Moreover, pan-leukocyte staining with CD45 showed a monolayer of leukocytes, likely macrophages, limited to the material-tissue interphase, a normal reaction to biocompatible materials (Fig. 10H) [70]. It is noteworthy that the thickness of the fibrotic capsule was comparable to that reported by other medical devices implanted for similar time periods [71, 72]. Taken together, these results indicate NICHE is mechanically stable and biocompatible.

4.3 In vivo NICHE vascularization

As oxygen and nutrient delivery to transplanted cells is imperative for engraftment and survival, we sought to create a highly vascularized environment that would provide adequate mass transport to and from the graft. To this end, we explored the use of MSCs for their known ability to drive vascularization [73]. We subcutaneously implanted NICHEs filled with vehicle hydrogel as control (Fig. 11A), and either 250,000 (Fig. 11B) or 500,000 MSCs (Fig. 11C) in rats and allowed for a vascularization period of 6 weeks. Upon explantation, we observed that NICHE was bio-integrated into the subcutaneous tissue with visible blood vessels branching from the host tissue, through the nylon meshes, and penetrating into the device (Fig. 11D and Appendix A8). Gross analysis of cross-sections of NICHEs revealed implantation with MSCs increased tissue penetration into the cell reservoir (Fig. 11A-C) with macroscopic vessels scattered throughout (Appendix A8). With respect to vehicle control (Fig. 11E), histological examination of MSC-loaded NICHE showed increased patent, red blood cell-laden vessels embedded in a collagenous extracellular matrix (Fig. 11F, G). Incorporation of MSC into NICHE increased blood

vessel density (vessel number / mm^2) in a dose-dependent manner. As compared to NICHEs containing vehicle hydrogel (n = 264 ± 114 vessels / mm^2), NICHEs loaded with 250,000 or 500,000 MSC had 170% (n = 457 ± 59 vessels / mm^2) and 270% (723 ± 121 vessels / mm^2) higher vessel density, respectively (Fig. 11H). Moreover, the vascular structures within NICHE showed positive labeling for vessel markers *B. simplicifolia* lectin (Fig. 11E-G), alpha smooth muscle actin (αSMA; Fig. 11I), and rat endothelial cell antigen 1 (RECA-1; Fig. 11J). The merged immunofluorescence image of αSMA and RECA-1 showed concentric labeling with the endothelial layer surrounded by the muscularis layer, indicating vessel maturity (Fig. 11K, L). Importantly, blood vessel markers stained positively in control as well as MSC-loaded NICHE, indicating that NICHE structure is conducive to functional and mature vessel colonization. Based on significantly higher extent of vascularization, 500,000 MSC were used for pre-vascularization of the cell reservoir in all future studies.
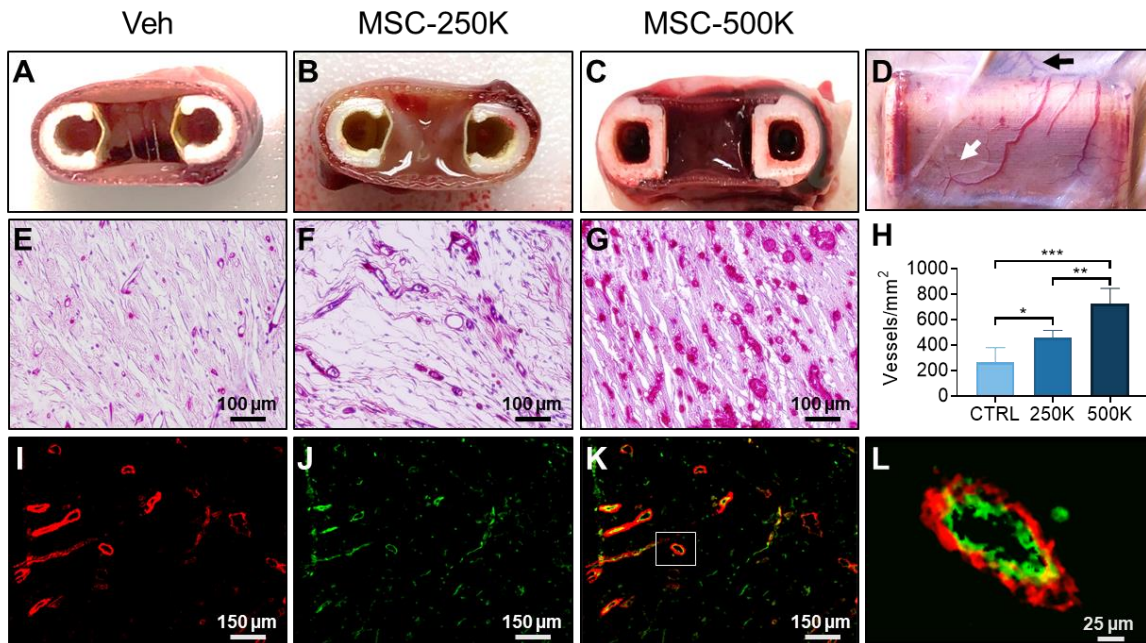

Fig. 11 NICHE pre-vascularization using MSCs. Gross cross-sections of explanted NICHE from rats after a 6-week pre-vascularization period using (A) vehicle hydrogel (Veh) or hydrogel containing (B) 250,000 MSCs (MSC-250K) or (C) 500,000 MSCs (MSC-500K) loaded in the cell reservoir. (D) Magnification of MSC-500K NICHE with visible blood vessels penetrating from the subcutaneous tissue (black arrow) into the cell reservoir (white arrow). Representative sections of tissue collected from cell reservoirs of (E) Veh, (F) MSC-250K, and (G) MSC-500K NICHE at 6 weeks post-implantation with blood vessels labeled in red with *B. simplicifolia*. (H) Blood vessel density quantification of sections obtained from Veh, MSC-250K, and MSC-500K NICHE (12 fields of view/slide; n=4-5 NICHE/condition). Mean ± SD. One-way ANOVA. Immunofluorescence analysis of cell reservoir tissue collected

from MSC-500K NICHE and immunostained for (I) αSMA and (J) RECA1. (K) Merged immunofluorescence image of αSMA-RECA1. (L) Magnification of area in K enclosed in the white square showing concentric labeling of αSMA-RECA1 in a blood vessel. MSC: Mesenchymal Stem Cells; H&E: Hematoxylin and Eosin; FFPE: Formalin-fixed, paraffin embedded; αSMA: alpha smooth muscle actin; RECA1: Rat Endothelial Cell Antigen 1.

4.4 CTLA4Ig in vitro release and cytotoxicity and in vivo loading

While vascularization of the cell reservoir is critical for cell viability, vasculature permits cellular influx, rendering allotransplanted cells unprotected from immune cell recognition and destruction. To overcome this issue, we incorporated a drug reservoir in NICHE for controlled delivery of immunosuppressant locally through a nanoporous membrane. We performed in vitro release assays to characterize the release profile of CTLA4Ig, an immunosuppressant with promise in preventing transplant rejection [74-76], from NICHE. One way of tuning NICHE drug release is through modification of the porous membrane surface area (Fig. 12A, B), which elutes CTLA4Ig into the cell reservoir. As a first approach, we assessed the release across a surface area of 69 mm^2 (Fig. 12A) and observed a rapid release rate that plateaued by day three, independently of the drug concentration loaded (Fig. 12C). To prolong dosing, we decreased the membrane surface area to 8 mm^2 (Fig. 12B), which slowed CTLA4Ig release rate and revealed a biphasic release profile (Fig. 12D). During the first 10 days, devices loaded with 3.4 and 11 mg/mL released an average of 16 and 70 µg/day of drug, respectively. By day 13, the release rate decreased to 9 and 22 µg/day and remained quasi-constant for an additional 30 days. Overall, the daily release rate changed proportionally to the concentration of drug loaded, while a biphasic release profile occurred across concentrations (Fig. 12E). Maintenance of drug stability is imperative for prolonged dosing. As such, we investigated the stability of CTLA4Ig in solution at 37 ºC over 3 weeks. Chromatography traces of freshly prepared CTLA4Ig and solutions incubated for 1 and 3 weeks were similar across all samples, showing a single monomodal peak corresponding to CTLA4Ig. The peak intensity, which is directly correlated with CTLA4Ig concentration, did not change during incubation and no additional peaks that could correspond to CTLA4Ig aggregates of degradation products were observed, indicating no loss in CTLA4Ig (Fig. 12F). We demonstrated that CTLA4Ig is stable and drug delivery is tunable through altering loaded drug concentration or modifying NICHE surface exchange area. For prolonged and sustained drug dosing during transplantation, we used the 8 mm^2 configuration of the drug reservoir for the next in vivo experiments.
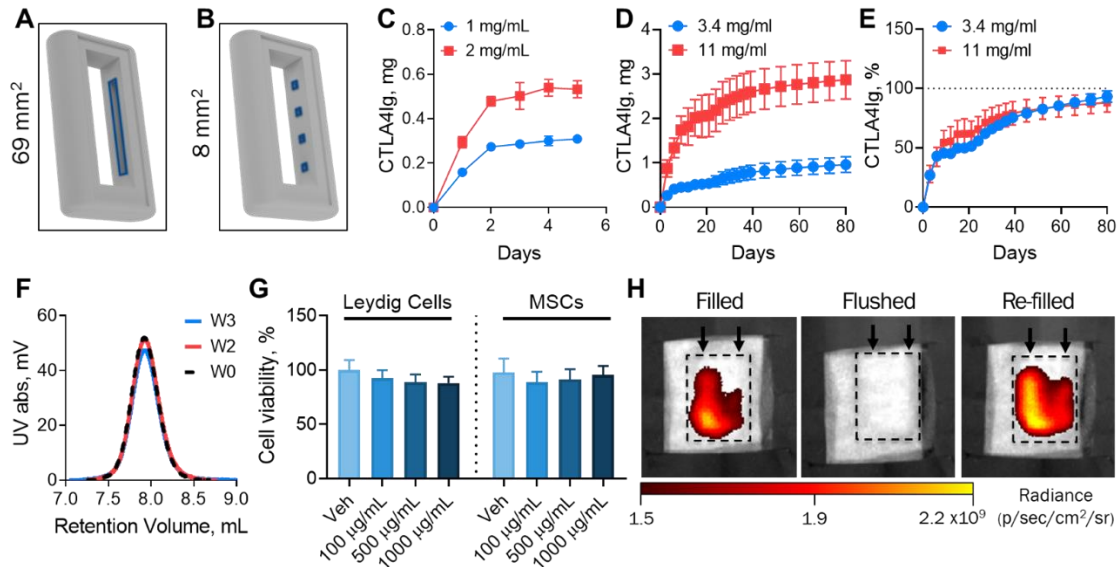
Fig. 12 CTLA4Ig in vitro release and cytotoxicity. 3D rendering of NICHE with (A) 69mm^2 and (B) 8mm^2 drug reservoir surface exchange areas delineated in blue. In vitro CTLA4Ig release from NICHE with (C) 69 mm^2 or (D-E) 8 mm^2 surface exchange areas. (F) CTLA4Ig stability in solution at 37 °C. (G) Viability of Leydig cells and Mesenchymal Stem Cells (MSCs) cultured with CTLA4Ig or culture media (Veh). Mean ± SD. One-way ANOVA. (H) IVIS analysis of drug reservoir refilling in implanted NICHE using fluorescently tagged CTLA4Ig.

In situ immunosuppressant elution into the cell reservoir results in direct drug exposure to transplanted graft. As such, we investigated the cytotoxic effect of CTLA4Ig on Leydig cells and MSCs via MTT assay. In vitro cytotoxicity studies revealed that incubation with CTLA4Ig at increasing concentrations of 100, 500, and 1000 μg/mL did not impact Leydig cell or MSC viability, with respect to media only control (Fig. 12G). This data suggests that CTLA4Ig is suitable for use in a local setting without detrimental effects on cells.

Long term deployment of NICHE would require periodic replenishment of the drug reservoir. As such, we evaluated in vivo transcutaneous refillability in rats using CTLA4Ig fluorescently labeled with Alexa Fluor 647 (CTLA4Ig-AF647), which allowed visualization of the drug via IVIS. NICHE drug reservoir was transcutaneously filled with CTLA4Ig-AF647 after subcutaneous implantation (Fig. 12H). The signal intensity localized within the filled drug reservoir disappeared upon reservoir flushing with saline and was re-established once the reservoir was replenished, indicating successful transcutaneous manipulation and refilling of drug reservoir (Fig. 12G). Taken together, this data indicates that local release of immunosuppressant via NICHE is tunable, CTLA4Ig is non-toxic, and the drug reservoir is easily replenishable.

4.5 In vivo validation of NICHE

To assess the efficacy of our encapsulation system in vivo, we performed allogeneic Leydig cell transplantation in NICHE using immunocompetent rats following the deployment strategy described in Fig. 1. We used luciferase-expressing Leydig cells, which allowed us to track cell viability and retention in NICHE. We compared NICHE (local CTLA4Ig immunosuppression) to daily systemic CTLA4Ig administration via intraperitoneal injection (IP), and no immunosuppression (Control). NICHE filled with 500,000 MSCs were subcutaneously implanted in the dorsum of rats and allowed 6-weeks for prevascularization period. Following this, CTLA4Ig was transcutaneously loaded into the drug reservoir. Leydig cells were co-transplanted with MSCs in all groups, leveraging their immunomodulatory properties that hold promise in promoting transplant engraftment and survival [63, 73]. NICHEs in all groups were assessed via IVIS imaging one day after transplantation, and weekly thereafter. On day 1, NICHEs in all groups were observed to have luminescence signal, indicative of successful cell loading and viability (Fig. 13A). By day 14 post-transplant, 100% of rats in the control group without immunosuppression had lost signal. On the contrary, rats in NICHE and IP groups maintained 75% and 60% graft survival, respectively, with comparable signal intensities up to day 31, indicating that immunosuppression was imperative for allogeneic cell survival (Fig. 13A-C). Importantly, upon explantation of NICHEs at study termination on day 31, there was no residual luminescence signal, indicating that the bioluminescent cells were fully retained within NICHE (Fig. 13A, Day 31 PE).
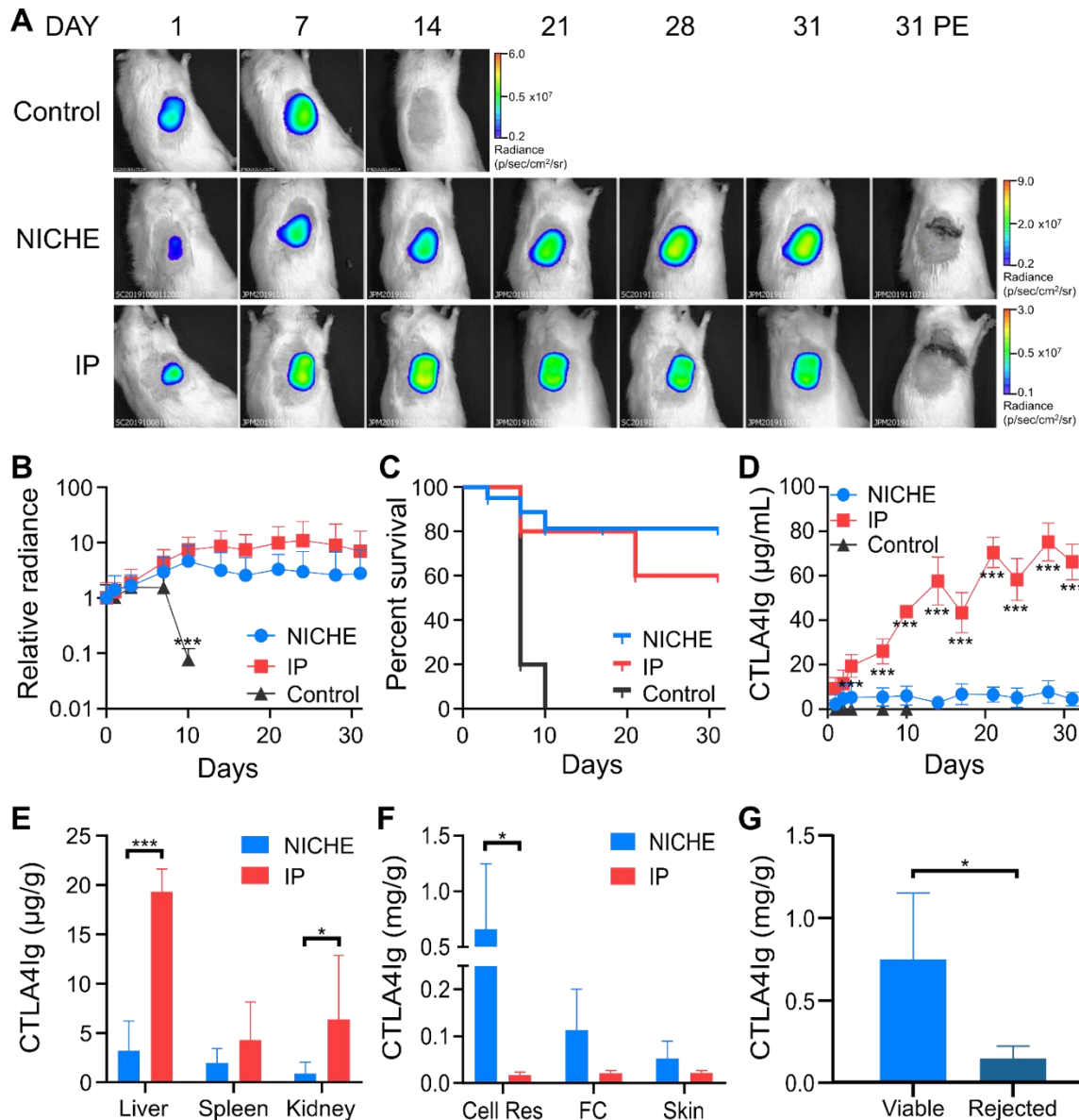
Fig. 13 NICHE efficacy study. (A) IVIS analysis of allogeneic Leydig cells transplanted in NICHE receiving no immunosuppressive treatment (Control), local CTLA4Ig delivery from the drug reservoir (NICHE) or systemic CTLA4Ig delivery via intraperitoneal injections (IP). (B) IVIS signal intensity quantification relative to day of transplant. (C) Kaplan-Meier survival curve indicating last day of signal obtained from IVIS. Log-rank test NICHE vs IP p=0.46; NICHE vs Control p=0.001; IP vs Control p=0.01. (D) ELISA analysis of plasma CTLA4Ig concentration throughout the 31-day study. CTLA4Ig quantification in (E) peripheral organs or (F) transplant site: cell reservoir, fibrotic capsule, and skin in contact with NICHE at time of NICHE retrieval via ELISA. (G) CTLA4Ig quantification in tissue from cell reservoirs of viable and rejected grafts. PE: Post explant; Cell Res: Cell reservoir; FC: Fibrotic Capsule. Mean ± SD. Statistical analysis was performed via two-way ANOVA (D-F) and student's t-test (G) *p<0.05, ***p<0.001.

Exposure to immunosuppression was assessed via quantification of CTLA4Ig levels in plasma (Fig. 13D) and peripheral tissues (Fig. 13E). Rats in the control group had no detectable CTLA4Ig throughout the study. In the plasma of experimental animals, drug levels were detectable by day 1 of administration with both NICHE (2.19 ± 4.10 µg/mL) and IP (9.15 ± 5.11 µg/mL) delivery. CTLA4Ig plasma concentration in the IP group escalated consistently for 14 days up to 57.67 ± 10.79 µg/mL and fluctuated thereafter, peaking at 75.30 ± 8.52 µg/mL on day 28. In contrast, CTLA4Ig plasma concentrations in rats receiving local immunosuppression with NICHE reached about 6 µg/mL 2 days after reservoir loading and remained stable for 10 days (Fig. 13D). On day 14, plasma concentrations dropped to ~ 2 µg/mL, suggesting a decrease of CTLA4Ig in the drug reservoir. At this point, the drug reservoir was transcutaneously re-loaded, which restored plasma CTLA4Ig levels to steady state. Preemptive re-filling of the drug reservoir on day 24 (10 days after first re-filling) maintained plasma levels constant throughout the remainder of the study, underscoring efficient transcutaneous refilling. Overall, systemic drug exposure was up to 12 times higher in the IP cohort, compared to NICHE. Similar to plasma, CTLA4Ig accumulation in peripheral tissues was higher in IP than NICHE group, with 6-fold, 3-fold and almost 2-fold higher levels in liver, kidney, and spleen, respectively (Fig. 13E). Quantification of CTLA4Ig in the transplant microenvironment revealed that rats receiving local immunosuppression resulted in a gradient-like distribution with uppermost concentrations in the cell reservoir (0.66 ± 0.58 mg/g), followed by the fibrotic capsule (0.11 ± 0.08 mg/g) and skin (0.05 ± 0.03 mg/g) (Fig. 13F). In contrast, rats receiving systemic immunosuppression had lower concentrations (~0.02 mg/g) and homogeneously low distribution of CTLA4Ig across tissues in the transplant microenvironment (Fig. 13F). Moreover, in rats receiving local immunosuppression, CTLA4Ig concentration was higher in cell reservoir tissues with viable (0.75 mg/g ± 0.15 mg/g) versus rejected (0.15 ± 0.07 mg/g) grafts (Fig. 13G).

We evaluated the tissue collected from the cell reservoir of NICHE for assessment of Leydig cell engraftment and immune infiltration via histological analysis. The rejected grafts had visibly fewer engrafted cells (Fig. 14A), in line with decreased IVIS signal intensity. Histological analysis of viable grafts showed Leydig cell engraftment in both local (Fig. 14B) and systemic immunosuppression cohorts (Fig. 14C). Moreover, CD3 (pan-lymphocyte) staining revealed that immune cell infiltration was higher in rejected (Fig. 14A) than viable grafts (Fig. 14B-C). To further characterize the immune reaction at the transplant microenvironment, we analyzed CD4 and CD8 lymphocyte subpopulations. Rejected grafts (Fig. 14D) had significantly more CD4 and CD8 positive cells than viable grafts with local (Fig. 14E) or systemic immunosuppression (Fig. 14F and G). However, the CD4 to CD8 ratio did not change, suggesting immunosuppressive treatment ameliorated, but not shifted, the immune response at the transplant microenvironment (Fig. 14H). It is noteworthy that, in rats receiving local immunosuppression, cell reservoirs with

viable grafts had higher CTLA4Ig concentrations and lower lymphocyte infiltration than those with rejected grafts, underscoring efficient local immunosuppression. Further, we assessed if cell transplantation and local versus systemic immunosuppression affected host reactivity towards NICHE by means of fibrotic capsule thickness and leukocyte infiltration. We found no significant difference in fibrotic capsule composition between groups (Appendix A7). Taken together, these data suggest that 1) NICHE microenvironment was conducive to cell engraftment; 2) local delivery of immunosuppressant effectively maintained graft viability while reducing systemic exposure up to 12-fold; 3) fibrotic capsule formation is a resolved reaction to the device and not to transplanted cells or immunosuppressant.
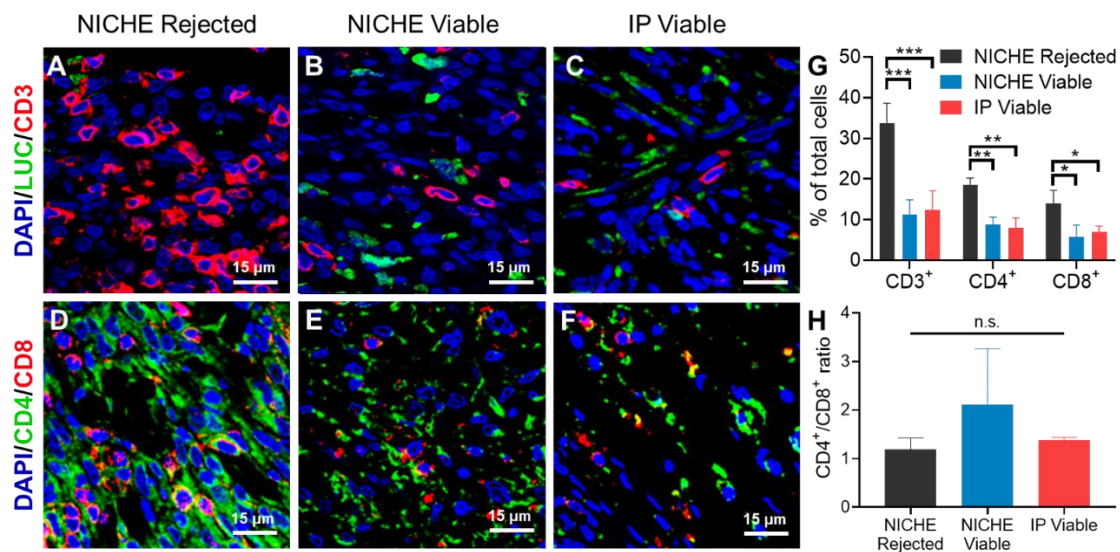

Fig. 14 Immunofluorescence analysis of tissue collected from NICHE cell reservoirs transplanted with Leydig cells. Sections were immunostained for (A-C) luciferase/Leydig cells (green) and pan-lymphocyte marker CD3 (red) or (D-F) CD4 (green) and CD8 (red). Nuclei were stained with DAPI (blue). Tissues were collected from (A, D) Rejected grafts in NICHE with local immunosuppression cohort; (B, E) Viable grafts under NICHE with local immunosuppression; and (C, F) Viable grafts under systemic IP immunosuppression. (G) Quantification of $CD3^+$, $CD4^+$, and $CD8^+$ cells expressed as percent of total cells per field of view. Mean ± SD. Two-way ANOVA. (H) $CD4^+/CD8^+$ ratio per field of view. Mean ± SD. One-way ANOVA (12-24 fields of view/slide; n=3 NICHE/condition).

In this study, we developed NICHE, an encapsulation platform integrating in situ pre-vascularization and local immunosuppressant delivery for engraftment of allotransplanted cells. NICHE was carefully designed to meet key components for successful cell encapsulation: biocompatibility, mechanical stability, scalability, feasibility of clinical use, efficient mass transport, and immune system evasion.

3D printing for manufacturing of medical devices in the context of tissue regeneration is widely used as it allows creation of complex designs that provide a personalized approach to meet patient need. Using selective laser sintering to manufacture NICHE provided ease of design modification and fast, cost-effective scalability. These characteristics are especially relevant for clinical translation to allow size and geometry customization depending on transplant type or individual need, and to produce enough devices to meet clinical need. Among the wide range of materials compatible with SLS, we chose nylon as it is a non-biodegradable and robust material with long-lasting tensile strength and high elasticity [69]. These characteristics make nylon an ideal material for long-term deployment inside the body by having the mechanical stability required for implantation in the subcutaneous space, where movement and exposure to external forces could compromise device integrity [31]. Further, nylon is an ideal polymer for SLS manufacturing [77], widely characterized for biomedical use [78], and readily commercially available, which allows for straightforward, reproducible elaboration of the device. Moreover, nylon is biocompatible and widely used as an implantable material for various applications ranging from suture material and catheters [79] in the clinical setting to scaffolding and cell encapsulation in pre-clinical research [31, 80]. Indeed, the results of this study showed the nylon used to construct NICHE was mechanically stable and highly biocompatible in vitro and in vivo.

Deployment of NICHE in the subcutaneous space allows straightforward, clinically relevant use in terms of ease of implantation, refillability, and retrievability. Specifically, NICHE implantation into a subcutaneous pocket required only an ambulatory and minimally invasive surgical procedure, similar to those performed currently for implantation of other subcutaneous medical devices [81]. Device placement directly under the skin renders NICHE drug and cell reservoirs easily accessible, allowing for straightforward transcutaneous filling with immunosuppressant or replenishment of cells as needed. These procedures could be easily performed in a doctor's office in an outpatient setting. Further, we demonstrated successful and minimally invasive en bloc removal of intact NICHE surrounded by a thin fibrotic capsule and with complete containment of transplanted cells, which further informed on key safety aspects should retrieval be needed due to adverse side effects.

Pre-vascularization of the transplant site has shown promise in being conducive for efficient mass transport between graft and host by reducing the distance between the transplant and source of oxygen and nutrients [82, 83]. In the context of tissue engineering, many strategies have been used to drive vascularization, including release of angiogenic factors [51], formation of scaffolds for endothelial colonization [84, 85], and co-transplantation with endothelial cells or MSCs [86, 87]. With NICHE, we used MSCs to drive vascularization into the cell reservoir by leveraging their ability to produce an angiogenic wound healing response. MSCs serve as pericytes to promote neovessel maintenance [88], and can also modulate their

microenvironment to ameliorate immune response. Indeed, NICHEs implanted with MSCs inside the cell reservoir were significantly more vascularized than controls in a dose-dependent manner. Moreover, the vessels had well-formed endothelial and muscularis layers, indicating they were structurally mature and permanent. Additionally, successful in vivo cell tracking of the luciferase-expressing cells used in our efficacy study further informed on the maturity of the vascular network formed within NICHE and its direct connection to the systemic vasculature. For our study, rats were administered an intraperitoneal (systemic) injection of luciferin prior to imaging. Obtaining bioluminescent signal from cells within NICHE post-systemic luciferin administration requires luciferin transport to the transplant site via the systemic circulation through vasculature. Signal generation from cells within NICHE indicated that they were viable and had preserved their metabolic activity, suggesting adequate vascular perfusion. While other cell encapsulation technologies are preferentially implanted in the omentum due to inherent high vascular density, at this site, device implantation, manipulation, and retrieval are complicated and require invasive procedures.

While the subcutaneous space is commonly considered poorly vascularized, Using NICHE, we were able to obtain a mature vascular network suitable for cell engraftment. Notably, the blood vessel density achieved with our approach was comparable to that reported for pancreas. This highlights the NICHE potential for transplantation of hypoxia-sensitive cells [89] such as pancreatic islets. Pancreatic islets have high oxygen demand and require extensive vascular apposition to develop intra-islet capillary networks, especially during engraftment [90]. Further enhancement of vascularization could be achieved. As an example, concomitant to implantation with MSC hydrogel in the cell reservoir, NICHE drug reservoir could be loaded with pro-angiogenic factors such as Vascular Endothelial Growth Factor (VEGF) during the pre-vascularization phase, further potentiating neo-vessel formation. Alternatively, implantation of NICHE with a scaffold pre-conditioned with growth factors in the cell reservoir to tailor the architecture of the microenvironment could also be feasible [91]. We are currently exploring these strategies as we prepare to move the platform for transplantation of other cell types, including pancreatic islets.

Direct contact of graft with blood vessels necessitates systemic immunosuppression, which is associated with a myriad of side effects spanning risk of infection, cancer development, and death [92, 93]. As an alternative to systemic immunosuppression, NICHE contains a drug reservoir that elutes immunosuppressant directly into the cell reservoir. In our study, we used CTAL4Ig as the immunosuppressant for its ability to bind to CD80 and CD86 on antigen presenting cells (APCs) and block co-stimulation through CD28 on T cells, thus inhibiting early phases of T cell activation [94, 95]. In vitro, we observed a biphasic release rate using the 8 mm^2 membrane surface area, which was congruent with a progressive decrease in CTLA4Ig concentration inside the drug reservoir. Notably, the release rate observed in our in vivo efficacy study

mimicked in vitro behavior as plasma CTLA4Ig levels remained constant for a period of 10 days and dropped soon after, indicating a decrease in release rate. Upon transcutaneous refilling of the drug reservoir, plasma trough levels were restored, underscoring consistent drug dosing and refillability of the drug reservoir. The correlation observed between in vitro and in vivo behaviors assures straightforward dose optimization in vivo by extrapolating in vitro testing. The plasma CTLA4Ig levels obtained with systemic administration in this study were comparable to other reports in patients and large animal studies [96-98]. It is noteworthy that administration of CTLA4Ig with NICHE confined drug to the transplant site and limited systemic exposure up to 12-fold while maintaining allogeneic cell survival as efficiently as with systemic dosing. Furthermore, lower accumulation of CTLA4Ig at the transplant site in locally immunosuppressed animals correlated with graft failure and higher immune cell infiltration. Interestingly, a non-statistically significant drop in IVIS signal intensity at day 14 correlated with a drop in CTLA4Ig plasma levels attributable to diminution of CTLA4Ig in the drug reservoir. We speculate that the drop in CTLA4Ig levels at the transplant microenvironment allowed for immune cell activation and attack on Leydig cells. Refilling of the drug reservoir likely restored local CTLA4Ig levels and prevented further rejection of transplanted cells, underscoring the efficacy of localized suppression. Mechanistically, a previous report showed that high-dose CTLA4Ig treatment was able to maintain allogeneic graft survival in spite of regulatory T cell (Treg) depletion, a known side effect of CTLA4Ig treatment [75]. We theorize that grafts survived with local immunosuppression because the concentration of CTLA4Ig within the cell reservoir was sufficiently high to suppress the host immune system at the transplant microenvironment; however, by limiting CTLA4Ig permeation into systemic circulation, Tregs were spared, resulting in a synergistic immunomodulatory effect. On the other hand, IP CTLA4Ig administration could have caused systemic immunosuppression that suppressed the host immune system even in the context of Treg depletion.

A limitation to our study is that maintenance of the allograft with local immunosuppression was only explored for a limited duration. Longer, more comprehensive studies to determine optimal dosing and immunosuppressive agents using different cell types are warranted and will further characterize our approach. The current prevailing strategy to achieve immune evasion in the field of cell encapsulation is by physical immunoisolation using nanoporous membranes [5, 7]. However, insufficient vascularization resulted in subpar graft function, prompting leaders in the field to move towards fully vascularized encapsulation systems that rely on undesirable systemic immunosuppression [99, 100]. Our approach is novel by providing both extensive vascularization of the encapsulation system and localized immunosuppression to circumvent the hurdles of systemic dosing. Localized immunosuppression for maintenance of transplanted allografts has been explored, although not in parallel with prevascularization. Some efforts using immunosuppressant loaded in nanoparticles targeted to the transplant site showed promise but finding a specific targeting moiety that efficiently enriches the

nanoparticles to the desired site is still a major challenge [101, 102]. Others explored in situ generation of immunosuppressant CTLA4Ig via adenoviral gene transfer in allogeneic islet [103], kidney [104], and cornea [105] transplantation with various degrees of success. Specifically in the context of islet transplantation [103], local CTLA4Ig expression via adenoviral transduction prolonged graft survival only marginally whereas a similar approach in a kidney transplantation model prolonged graft function for up to 2 months [104]. In an approach more similar to ours, Zhang et al [106] demonstrated that placement of a CTLA4Ig-eluting patch in the vicinity of transplanted pancreatic islets under the kidney capsule of mice prolonged graft survival over 150 days. However, even though their approach underscored promise for local immunosuppression, the patch was a separate entity to the transplanted islets and did not allow for retrievability. It is noteworthy that effective refillability and sustained dosing from NICHE drug reservoir can be exploited to further tailor the transplant microenvironment. For example, through sequential refilling of the reservoir with various immunomodulators, in single form or in cocktails, throughout the life of the transplant. This feature is especially important for clinical translation as clinically relevant immunosuppressive regimes go through induction and maintenance phases that employ various drugs and doses.

In summary, NICHE is the first encapsulation platform for allogeneic cells transplantation integrating extensive pre-vascularization and effective localized immunosuppression for allogeneic cell engraftment into a single, minimally invasive, retrievable platform. Our innovative, mutli-functional encapsulation platform could pave the way for a new cell replacement therapy approach, providing improved management of endocrine disorders.

Chapter 5

Islet transplantation with NICHE

In this study, the efficacy of NICHE for transplantation of pancreatic islets to revert diabetes was evaluated. Firstly, the feasibility of islet engraftment within the vascularized NICHE environment was evaluated in immunocompromised rats. Next, allogeneic islets were transplanted in NICHE of immunocompetent rats with localized co-delivery of anti-lymphocyte serum and CTLA4Ig.

5.1 Immunocompromised diabetic rat model.

Firstly, we investigated if the pre-vascularized environment in NICHE was hospitable for islet engraftment. To this end, we used immunosuppressed RNU as recipients, allowing to circumvent engraftment hurdles posed by the immunological barrier. Lewis (Lew) rats were used as islet donors. RNU rats were subcutaneously implanted with NICHE loaded with 5×10^5 MSC. Following a 4-week pre-vascularization period, rats were rendered diabetic via streptozotocin (STZ) injection and ~3000 Lew IEQ + 4×10^6 MSC embedded in collagen hydrogel were transplanted in NICHE (Appendix A3). Blood glucose (BG) levels dropped immediately, rats became euglycemic by day 5 post-transplantation and remained so thereafter (Fig 14A). NICHE explantation on day 60 resulted in reversal to diabetic state, confirming euglycemia was achieved due to transplanted islets. Furthermore, post-transplantation intraperitoneal glucose tolerance test (ipGTT) demonstrated adequate islet function with glycemic curves similar to those of healthy controls (Fig 14B). In contrast, ipGTT performed after NICHE explant demonstrated loss of glycemic control with sustained hyperglycemia comparable to that observed pre-transplantation.
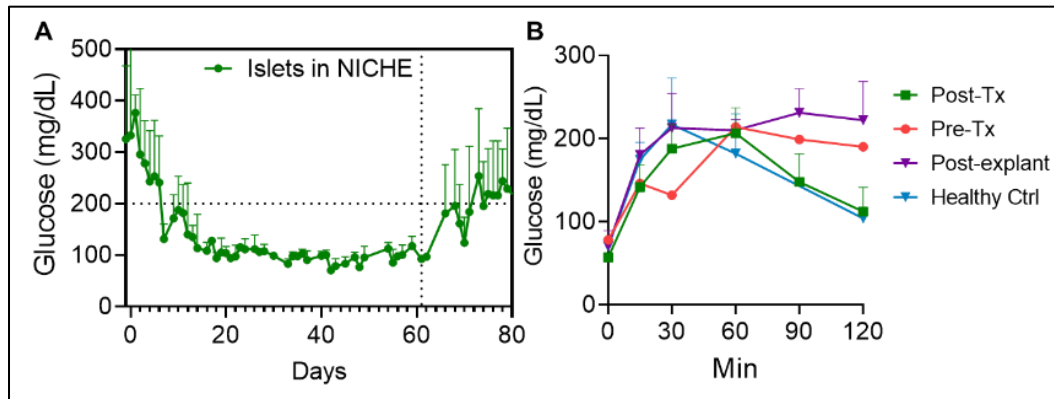

Fig. 15 Islet transplantation in immunocompromised rats. BG curves of (A) non-fasted and (B) during ipGTT in diabetic nude rats transplanted with islets in NICHE. Tx: Transplant.

Histological analysis of explanted NICHE showed engrafted islets with preserved architecture and intra-islet revascularization (Fig 16A, B). Immunohistochemical (IHC) analysis demonstrated insulin expression within graft, further underscoring preserved cell fate and function (Fig 16C). Moreover, pancreatic tissue in the transplanted animals did not stain positively for insulin, indicating lack of native islet function and further demonstrating diabetes reversal was due to the transplanted

islets (Fig 16D). In their native environment, islets are well embedded in the extracellular matrix (ECM) and profusely vascularized via intra-islet capillaries [90, 107]. ECM anchoring promotes islet survival and function, preserves islet architecture and cell fate, and downregulates apoptotic gene expression [108-110]. During the isolation procedure, the connection between islets, vasculature, and ECM gets severed, which rapidly compromises islet viability in culture. In vitro culture of islets embedded in collagen enhanced islet viability (Fig. 16E), which has also been reported by others [111]. Therefore, in our approach, islets and MSC were embedded in a collagen hydrogel immediately prior to the transplantation procedure. We posit that using collagen as a carrier during transplantation provided ECM anchoring support to islets, preserving architecture and downregulating apoptosis. Moreover, collagen hydrogels are conducive to vascularization which, in tandem with co-transplantation of pro-angiogenic MSC, might have further contributed to islet re-vascularization [63, 112, 113]. In an allogeneic setting, MSC immunomodulatory potential would have the added benefit of ameliorating allo-response to the graft [114, 115]. Finally, co-culture of islets with MSC improved islet insulin secretion after glucose stimulation (Fig. 16F) which correlated with extensive literature demonstrating co-transplantation with MSC enhances islet engraftment and function [116-119]. In sum, these results indicated NICHE pre-vascularized microenvironment is conducive to islet engraftment and long-term function.
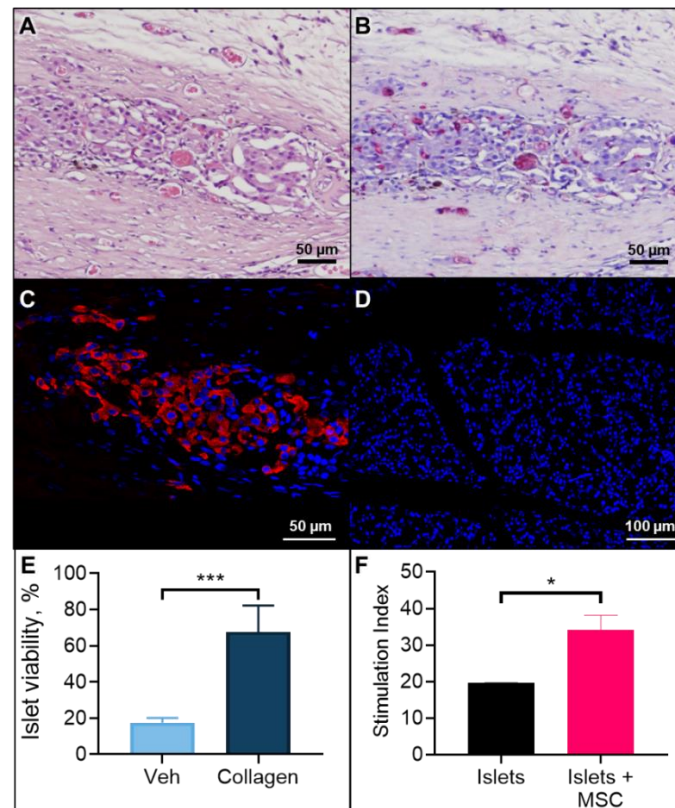

Fig. 16 Islet engraftment in NICHE. Sections of NICHE cell reservoir tissue from a transplanted, euglycemic rat stained with (A) H&E, (B) *B. Simplicifolia* lectin, and (C)

Insulin (red) and DAPI (blue). (D) Pancreatic tissue collected from the same rat as A-C stained with insulin. (E) Live/Dead assay results of islets cultured in media (veh) or collagen hydrogel for 5 days. (F) Glucose stimulated insulin release from islets after 28 h in culture alone or with MSC. E and F results are expressed as mean ± SD and analyzed via student's t-test.

5.2 Immunocompetent diabetic rat model.

In the following study we investigated NICHE efficacy for allogeneic islet transplantation in an immunocompetent diabetic rat model using localized immunosuppression.

5.2.1 Immunosuppression for islet transplantation.

The immunological barrier imposed by MHC mismatching necessitates alloresponse amelioration. In a previous study, we used CTLA4Ig monotherapy to prevent rejection of allogeneic Leydig cells transplanted in NICHE for 31 days [20]. CTLA4Ig is an effective immunosuppressant clinically approved for treatment of rheumatoid arthritis and prophylaxis of renal transplant rejection [120-122]. Moreover, CTLA4Ig prolonged islet engraftment in large animal models [122-125] and clinical trials [126]. However, a study exploring CTLA4Ig monotherapy for renal transplantation demonstrated that it is not effective as a standalone immunosuppressant [127]. As such, CTLA4Ig is always combined with other immunosuppressive agents to provide long-term protection.

Anti-lymphocyte serum (ALS) is a lymphocyte-depleting polyclonal antibody preparation and is the rat analog of anti-thymocyte globulin (ATG) used in the clinic. Systemic dosing of ATG causes profound immunosuppression with high rates of opportunistic infection; thus, it is only used transiently as induction therapy or during acute rejection episodes [128]. Current ATG dosing regimens are empiric and highly variable. An ideal dose of ATG would prevent severe graft rejection, while simultaneously allowing for adequate immune reconstitution to prevent severe adverse effects. High dosing of ATG reduced the risk of graft-versus-host disease (GVHD) at the expense of increased risk for infectious death and nonrelapse mortality [129]. On the contrary, low doses of ATG increased the risk for severe acute GVHD [130]. A reduction in circulating T-cell concentration to <20 cells/μL following ATG therapy was regarded as adequate immunosuppression for organ transplantation [131]. Under this regimen, lymphocyte depletion was observed by day 2 of administration [132], which correlated with a massive, transient cytokine storm [133]. A recent study showed that co-treatment with CTLA4Ig and prolonged low-dose ATG benefited allograft survival synergistically by promoting Treg expansion, inhibiting effector T cell activation, and preventing anti-rabbit antibody generation, but systemic immunosuppression still ensued [134]. We posit that low-dose, localized CTLA4Ig and ALS co-delivery with NICHE will obviate ALS systemic toxicity while maintaining immunosuppressive synergy with CTLA4Ig.

Localized immunosuppressant delivery inherently causes direct, chronic immunosuppressant exposure to the graft. Calcineurin and mTOR inhibitors, which

are highly effective for clinical islet transplantation [135], are incompatible with our model as they deter islet function (Fig. 17A) [93, 136]. Thus, we sought to elucidate the safety profiles of CTLA4Ig and ALS for appropriate localized dosing. We used quantification of CTLA4Ig levels in the cell reservoir from our previous study to determine relevant testing conditions. In vitro glucose stimulated insulin release (GSIR) assays performed after 5 days of incubation with drug showed CTLA4Ig did not inhibit islet function at any concentration tested (Fig. 17B). For ALS, the stimulation index was affected at concentrations higher than 1 mg/mL which was set as the toxicity threshold (Fig. 17C). Moreover, combination treatment with CTLA4Ig and ALS did not exacerbate islet toxicity (Fig. 17D). Of note, drug release from NICHE is tunable by means of concentration loaded, allowing to maintain ALS dosing below toxicity.
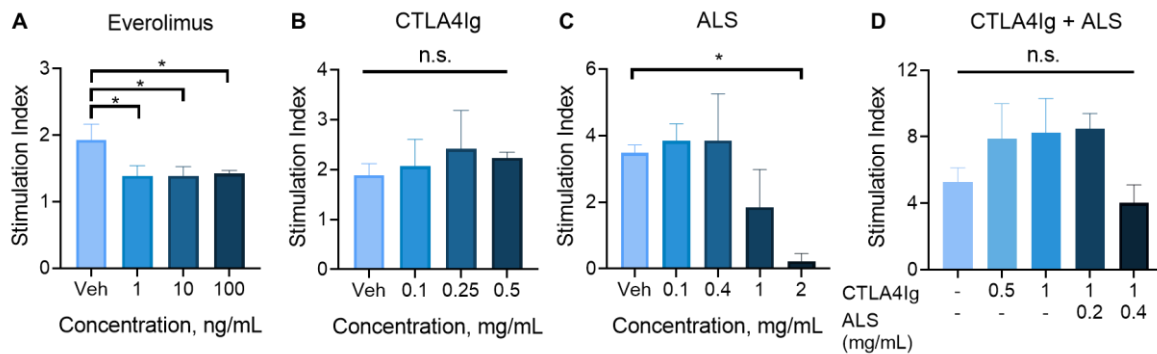
Fig. 17 Islet function under localized immunosuppression. Islet glucose stimulated insulin release of islets cultured with (A) Everolimus for 48 h, (B) CTLA4Ig (C) ALS, and (D) CTLA4Ig + ALS for 5 days. Mean ± SD. One-way ANOVA.

5.2.2 Islet transplantation in NICHE

To establish an allogeneic model, Lew rats were used as donors and Fischer 344 as recipients. F344 rats (n=4) were implanted with NICHE and allowed to pre-vascularize 4 weeks. NICHE were then loaded with an immunosuppression cocktail (ISC) composed of CTLA4Ig (55 mg/mL) and ALS (20 mg/mL). Three days after ISC loading, ~2,500 Lew IEQ and 3.75×10^6 F344 MSC were co-transplanted in NICHE. As an immunosuppressive therapy [137, 138], MSCs inhibit T cell proliferation, promote M2 macrophages polarization (anti-inflammatory and pro-angiogenic) [115, 139, 140], and induce transplant tolerance [141, 142]. Moreover, MSCs can enhance allogeneic islet engraftment [114, 118, 119, 143-145] and improve islet viability and insulin secretion [116, 117, 146] in preclinical models (Fig. 16F). A clinical trial using MSCs in diabetic patients demonstrated β-islet restoration and amelioration of hyperglycemia [147]. The islet cell to MSC ratio was calculated on the premise that 1 IEQ contains ~1500 cells [117, 118, 148, 149]. After transplantation, 1/4 animals became euglycemic whereas the remaining animals had only a decrease in BG levels (Fig 18A). ipGTT performed on day 10, correlated with these results where the animal with lower non-fasting BG showed response to glucose challenge (Fig

18B) whereas the remaining 3 did not. On day 25 the 3 animals that remained diabetic were transcutaneously (TransQ) refilled with ~3,250 Lew IEQ and 5 x 10^6 F344 MSC (Fig 18A). BG levels dropped to euglycemic levels in all animals and have remained so for 60 days (Fig 18A-study ongoing). This trend correlated with ipGTT performed on day 31 where 4/4 transplanted animals responded to glucose challenge (Fig 18C). Furthermore, animals in the NICHE cohort showed significantly lower BG than diabetic controls (Fig 18D) and responded to glucose challenge similarly to healthy controls (Fig 18E). Moreover, plasma C-peptide concentrations in NICHE rats were comparable to healthy controls and significantly higher than diabetic controls, demonstrating insulin release. Additionally, animals in the NICHE cohort showed body weight recovery approaching that of control cohort, further underscoring improvement in overall wellbeing (Fig. 18F).
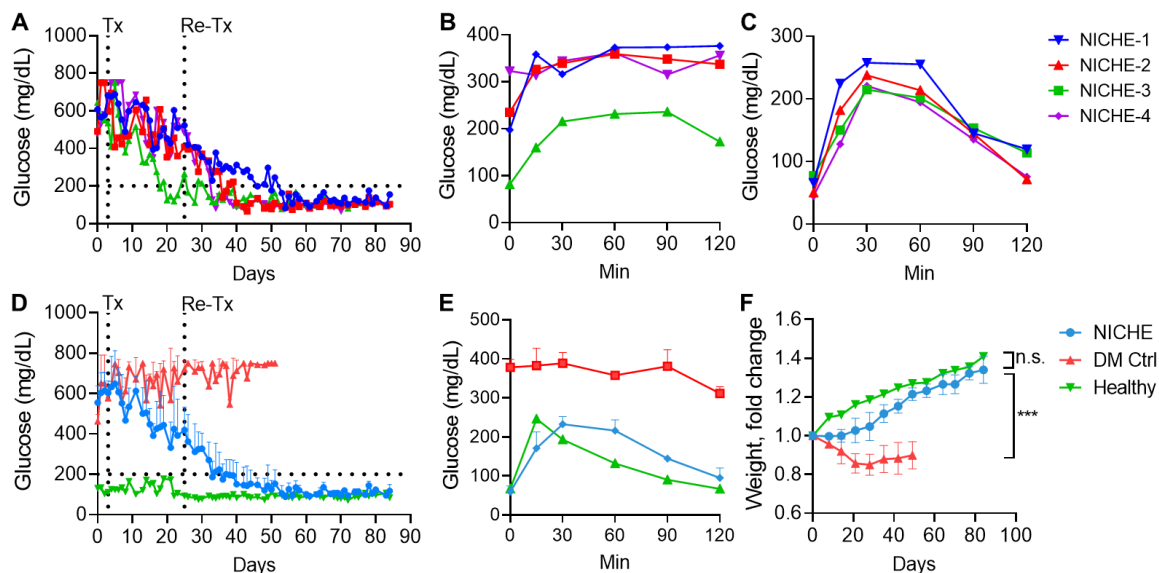
Fig. 18 NICHE efficacy study for allogeneic islet transplantation. Individual BG curves of (A) non-fasted and during ipGTT on days (B) 10 and (C) 31 of immunocompetent rats allotransplanted (Tx) with islets in NICHE. Grouped BG curves of (D) non-fasted and during ipGTT on day (E) 10 and (F) 31 of rats allotransplanted in NICHE, diabetic and healthy controls.

Plasma CTLA4Ig and ALS concentrations remained low and stable in a range between 20 and 40 µg/mL (Fig 19A). To establish a point of reference for systemic immunosuppression, a cohort of rats were injected systemically with ALS. Rats receiving systemic ALS displayed peak plasma concentrations of ~450 µg/mL (Fig 19A) that resulted in profound immunosuppression with circulating T-cell concentrations of ~5 cells/µL (Fig 19B). In contrast, ALS dosing through NICHE resulted in plasma levels ~20 µg/mL and circulating T-cell concentrations statistically identical to vehicle controls, indicating that local immunosuppressant release with NICHE did not induce systemic immunosuppression. These results not only demonstrate our localized immunosuppression strategy was safe and effective but

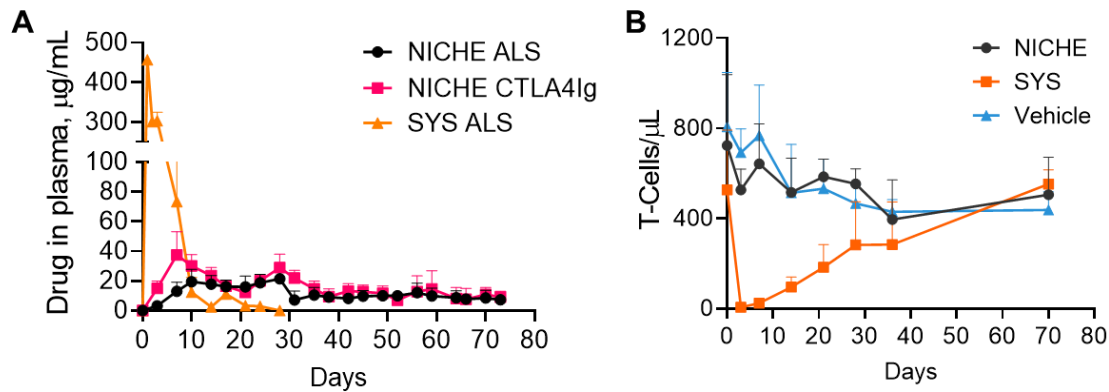further underscore feasibility of NICHE for co-delivery of clinically relevant immunosuppressive cocktails.

Fig. 19 Immunosuppression with NICHE (A) Plasma CTLA4Ig and ALS concentrations in rats dosed locally (NICHE) or systemically (SYS). Dotted line indicates NICHE drug reservoir refilling. (B) Circulating T-Cell concentration in rats receiving ALS locally (NICHE), systemically (SYS) or vehicle control.

As a mid-point analysis, on day 76 post-transplantation one NICHE was explanted from an animal with preserved graft function. Histological examination of NICHE showed engrafted islets in the cell reservoir with intra-islet revascularization (Fig. 20 A and B). Imaging mass cytometry analysis revealed the islet structures had a central beta-cell core (insulin+) surrounded by a mantle of alpha cells (glucagon+), indicating preserved morphology and cell fate (Fig. 20C). Moreover, the presence of neutrophils (Myeloperoxidase; MPO+) was negligible. Cytotoxic lymphocytes (CD8+, GranzymeB+) were scarce and scattered throughout the tissue. Importantly, lack of lymphocyte clustering and graft infiltration – hallmarks of active rejection [150, 151]– underscored efficient localized immunosuppression. Overall, these results indicated allogeneic islets transplanted in NICHE were well engrafted, revascularized, and without rejection.
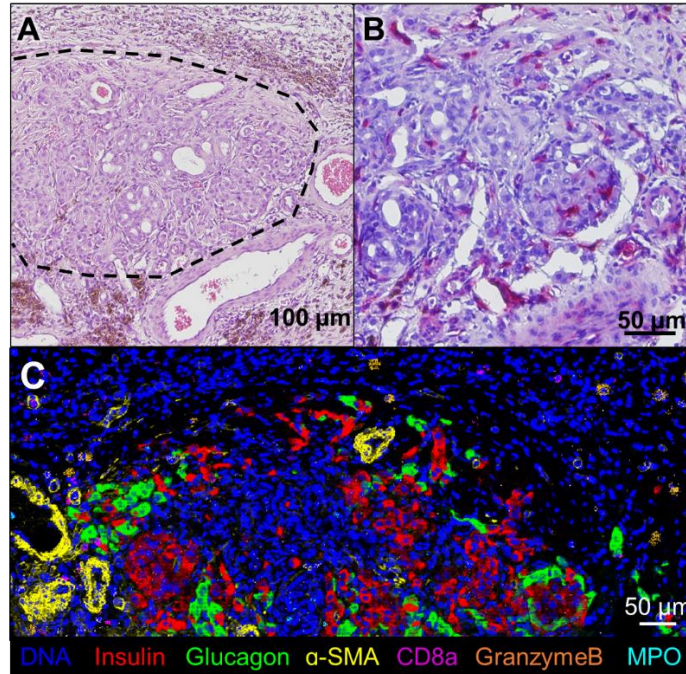
Fig. 20 Allogeneic islet engraftment in NICHE. Sections of NICHE cell reservoir tissue from a transplanted, euglycemic rat stained with (A) H&E; dotted line encircles engrafted islets, arrow head indicates siderophages, (B) *B. Simplicifolia* lectin (vessels in red), (C) Insulin (red) and Glucagon (green), and (D) Pan-leukocyte marker (CD45).

In sum, this study demonstrated the pre-conditioned NICHE cell reservoir was conducive to engraftment of allogeneic islets. The engrafted islets had preserved morphology and function, and restored euglycemia in diabetic animals. The localized delivery of ALS and CTLA4Ig was effective and safe as it provided long-term graft immunoprotection without inducing systemic immunosuppression. The NICHE is the first encapsulation system integrating direct vascularization and immunosuppression for the transplantation of islets, providing a transformative approach to diabetes management.

Chapter 6

Conclusions

6.1 Conclusions to the work presented herein

6.1.1 Vascularization study
The geometry, materials, and deployment strategy of our encapsulation platform promoted rapid biointegration with minimal foreign body reaction (FBR). Moreover, the immunomodulatory effect of MSC was highlighted by delayed and limited FBR to these devices. Both PRP and MSC drove extensive vascularization of cell reservoirs in rats and NHP. However, enrichment with MSC expedited vessel maturation across species. A combinatorial approach with implantation of devices enriched with both PRP and MSC could provide a synergistic effect to further potentiate the angiogenic response. We unveiled a promising window for cell transplantation at 2 weeks that would provide grafts with sufficient mechanical support, oxygen, and nutrients. In sum, we effectively enhanced the vascularization of our encapsulation device using PRP and MSC, creating a subcutaneous microenvironment promising for successful cell transplantation.

6.1.2 NICHE proof of concept study
The dual reservoir configuration of NICHE was conducive to efficient vascularization of the cell reservoir and sustained, localized immunosuppressant release. Pre-vascularization permitted rapid cell engraftment and preserved metabolic function. Localized immunosuppression protected cells from rejection while significantly limiting systemic drug exposure and potential adverse effects. NICHE is the first encapsulation platform integrating extensive pre-vascularization and effective localized immunosuppression for allogeneic cell engraftment into a single, minimally invasive, retrievable platform. Our innovative, multifunctional encapsulation platform could pave the way for a new cell replacement therapy approach, providing improved management of endocrine disorders.

6.1.3 NICHE efficacy for islet transplant
NICHE pre-vascularized environment was conducive to long-term islet engraftment, re-vascularization, and efficient diabetes management in 100% of transplanted subjects. NICHE configuration permitted straightforward co-delivery of 2 immunosuppressive drugs, underscoring relevance for translation into the clinical setting where immunosuppressive cocktails are the norm. Moreover, limited systemic exposure to immunosuppressants via localized delivery with NICHE permitted prolonged administration of potent drugs whose clinical use is hindered by systemic toxicity. Overall, this study demonstrated the potential of NICHE for pancreatic islet allotransplantation to treat type 1 diabetes, setting the stage for transitioning of the technology into models relevant to clinical translation.

6.2 Future perspectives

6.2.1 Future studies with NICHE for islet allotransplantation
Future studies will focus on optimization of key parameters to enhance engraftment efficiency in terms of optimal transplantation window, MSC dose for co-

transplantation, and minimal islet curative dose. Recapitulating a native environment that provides adequate vascular and ECM support is paramount to promote efficient islet engraftment and preserve metabolic function. However, the engraftment efficiency of islets transplanted into mature, unmodified tissues tends to be low and long-term function is often compromised [41]. Therefore, finding the optimal transplantation window that allows islet biointegration in parallel to active tissue remodeling is key for efficient islet engraftment. The benefits of islets and MSC co-transplantation are well documented; however, an optimal co-transplantation ratio varies with each system. Consequently, studies evaluating various MSC-to-islet ratios are warranted. Finally, Due to lack of an optimized microenvironment, up to 60% of the transplanted mass is lost during clinical islet transplantation [152]. As a result, patients often require serial transplantations (2-3 donors) to obtain clinical benefit and shortage in cadaveric donors further limits the number of patients that can be treated [153]. In our study, 3/4 rats required a second transplantation to obtain euglycemia. Thus, reducing the islet mass required for clinical benefit with NICHE is needed.

In the efficacy study presented herein, CTLA4Ig and ALS combination therapy successfully protected allogeneic islets from rejection in rats. We demonstrated localized co-delivery of anti-rejection therapeutics with NICHE is viable, paving an avenue towards implementation with other immunosuppressive cocktails. Due to immunological discrepancy between rodents and humans, future studies for optimization of clinically applicable anti-rejection cocktails are warranted in non-human primates which better recapitulate the human immune response. In addition, primate models are compatible with the large repertoire of immunosuppressive drugs available in the clinic, expediting future efforts towards translation.


6.2.2 Efforts towards clinical translation

NICHE key components were designed and selected with the target of streamlined clinical translation. Pre-vascularization of the cell reservoir is achieved using MSC whose wound healing, angiogenic and immunomodulatory properties are currently being leveraged for various applications in clinical trials [154]. In addition, MSC obtained FDA approval for hematopoietic and immunologic reconstitution [155]. Autologous bone-marrow derived-MSC are well characterized and widely used; however, their procurement is costly and invasive. Therefore, for clinical relevance, NICHE has been designed to be cell agnostic, providing adaptability for use with MSC from different sources such as adipose tissue, umbilical cord, and peripheral blood. Alternatively, hypoimmunogenic allogeneic MSC (Rooster Bio or OrganaBio) could be employed as an "off the shelf" MSC source. Localized immunosuppressant delivery for transplant rejection prophylaxis is clinically attractive for its potential in ameliorating systemic toxicity. NICHE drug reservoir is compatible with the wide array of clinically available immunosuppressive agents (Table 2), expediting adoption of NICHE into a clinically relevant setting. In addition, subcutaneous deployment allows minimally invasive, transcutaneous drug refilling that could be performed at the physician's office during routine visits or at home by trained patients. Donor shortage is a key hurdle in clinical islet transplantation and great

efforts are underway to obtain a more sustainable therapeutic cell source, namely stem-cell-derived beta cells. NICHE's pre-vascularized and locally immunosuppressed microenvironment could be optimized for transplantation of such cell types, maintaining clinical relevance of the platform as newer technologies become available. Finally, albeit the current prototypes used for pre-clinical testing do not meet current good manufacturing practices (CGMP), the fabrication and assembly procedures were designed for eventual transition into CGMP facilities. In sum, NICHE is conceptually disruptive and its versatile design conducive to adoption of current and future technologies, fundamentally contributing to the field of diabetes management.

Table 2. Clinically available immunosuppressants

| Lymphocyte-depleting	Anti-IL2	Anti-CD52
Thymoglobulin (rATG) ATGAM	Basiliximab (Simulect)	Alemtuzumab (Campath/Lemtrada)
Anti-CD20	**Costimulatory blockade**	**IL-6 inhibitors**
Rituximab (Rituxan) Ofatumumab (Kesimpta) Ocrelizumab (Ocrevus) Obinutuzumab (Gazyva)	Belatacept (Nulojix)	Tocilizumab (Actemra) Siltuximab (Sylvant) Sarilumab (Kevzara)
Anti-CD38	**Complement inhibition**	**JAK inhibitors**
Daratumumab (Darzalex) Isatuximab (Sarclisa)	C1 esterase inhibitor (Cinryze) C1 esterase inhibitor (Berinert) Eculizumab (Soliris) Ravulizumab (Ultomiris)	Tofacitinib
Proteasome inhibition	**Non-antibody therapies**	**Promising agents in clinical trails**
Carfilzomib (Kyprolis) Bortezomib (Velcade)	Cyclophosphamide (Cytoxan) Fostamatinib (Tavalisse)	Clazakizumab (anti-IL6; CSL Behring) IdeS/Imlifidase (IgG cleavage; Hansa Bio) Inebilizumab (anti-CD19; Viela Bio) VIB4920 (CD40L inhibitor; Viela Bio) REGN5458/9 (Anti-BCMA + Anti-CD3; Regeneron)

Appendix A – Supplementary materials

|	Alizarin red (Osteogenic)	Oil Red O (Adipogenic)	Alcian blue (Chondrogenic)
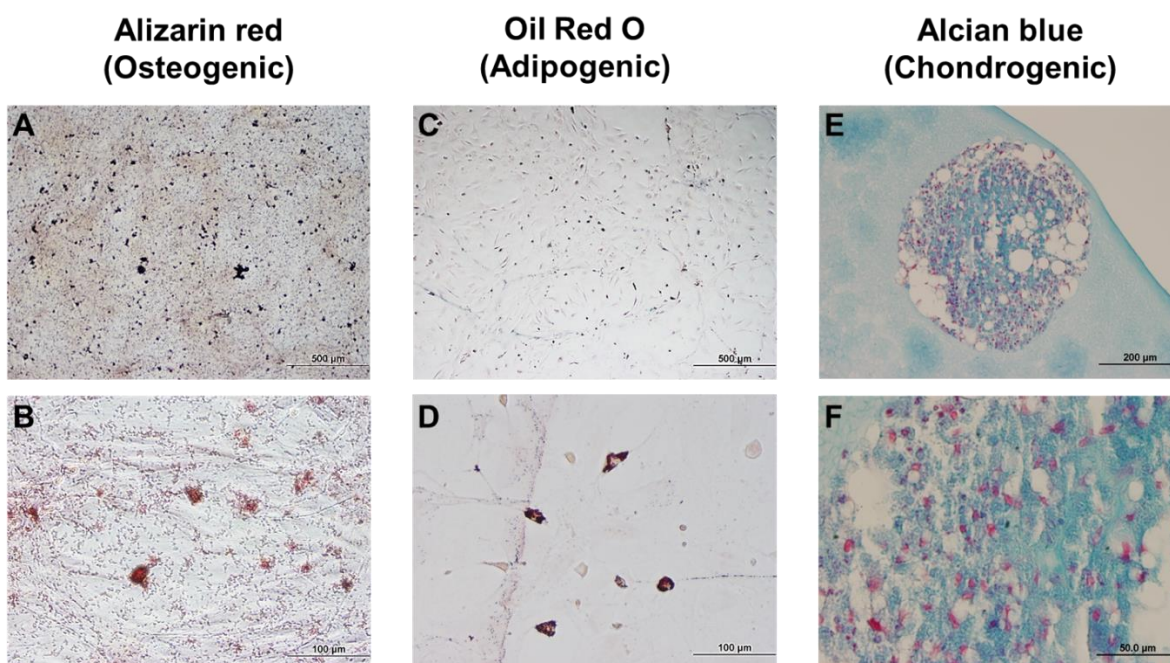
A1 - MSC differentiation potential. Images of Mesenchymal Stem Cells (MSCs) after (A-B) osteogenic, (C-D) adipogenic, and (E-F) chondrogenic differentiation showing mineralized extracellular matrix formation, intracellular lipid vacuoles and collagen formation, respectively.
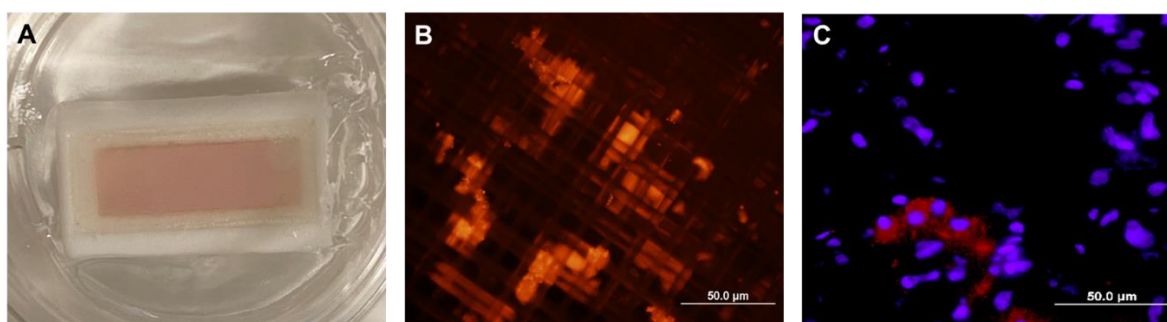
A2 - MSC permanence in NICHE (A) Optical image of NICHE filled with MSC-hydrogel prior to implantation. Fluorescent imaging of DiI-labeled MSCs inside NICHE cell reservoir (B) prior to implantation and (C) 6 weeks post-implantation (red).
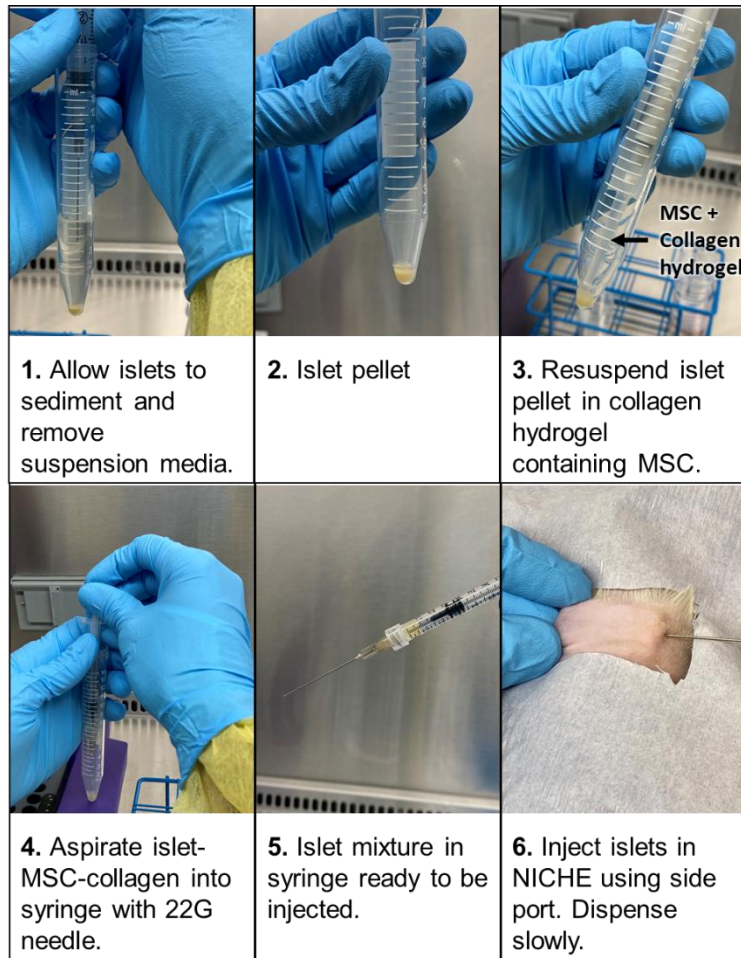
A3 - Islet transplantation procedure
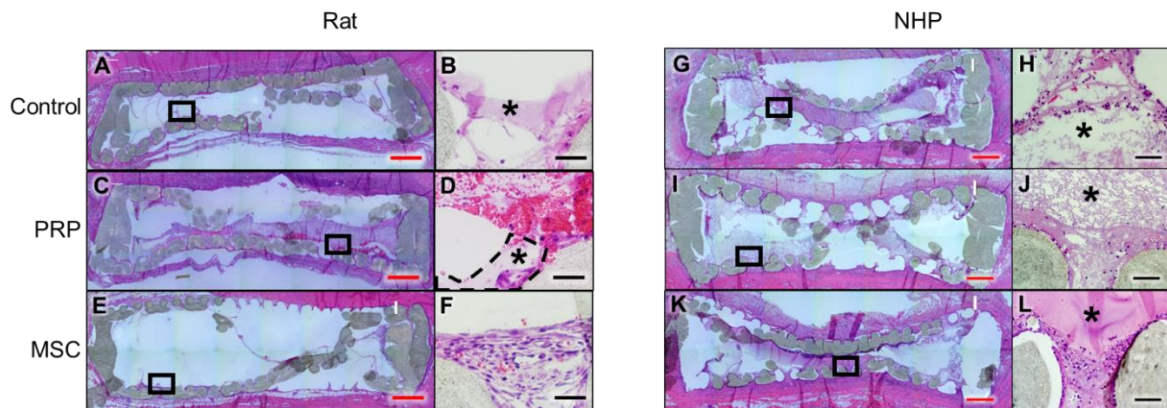
A4 - Devices at 1 week post-implantation. H&E-stained resin-embedded section of devices implanted for 1 week in (A-F) rats and (G-L) NHP. Rat tissues: (A) Control devices and (B) 10X magnified view of black box in A; (C) PRP devices and (D) 10X magnification, (E) MSC devices and (F) 10X magnification. NHP tissues: (G) Control devices and (H) 10X magnification, (I) PRP devices and (J) 10X magnification, (K) MSC devices and (L) 10X magnification. Red and black scale bars indicate 1 mm

and 100 µm, respectively. Black squares indicate areas of magnification. Asterisks indicate remnant hydrogel.
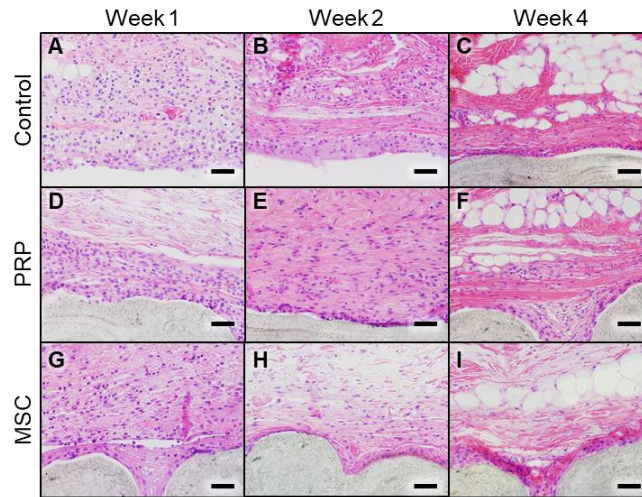
A5 - Reactivity to the implant in NHP. H&E stained sections of tissue around control devices (A) 1, (B) 2, and (C) 4 weeks post-implantation; PRP devices (D) 1, (E) 2, and (F) 4 weeks post-implantation; and MSC devices (A) 1, (B) 2, and (C) 4 weeks post-implantation. Scale bars represent 50 µm.
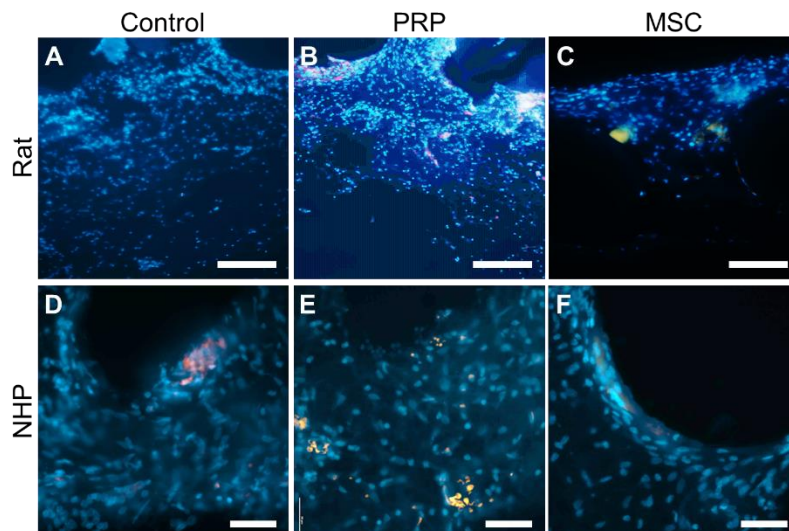
A6 - Isotype control staining of rat and NHP tissues. Isotype control staining of tissues collected from (A) Control, (B) PRP, and (C) MSC devices implanted in rat. Scale bars represent 100 µm. Isotype control staining of tissues collected from (A) Control, (B) PRP, and (C) MSC devices implanted in NHP. Scale bars represent 50 µm.
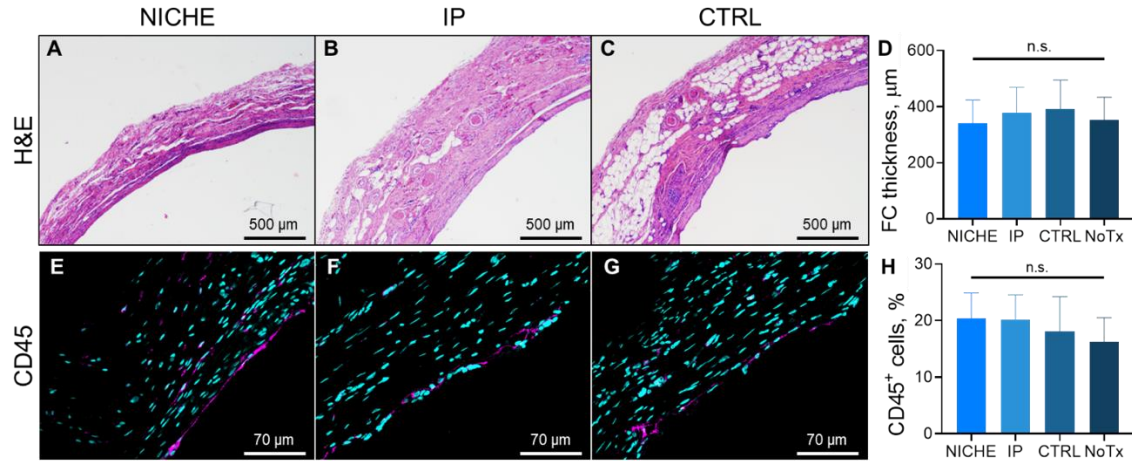
A7 - Fibrotic capsule formation in NICHE. H&E-stained sections of fibrotic capsules formed around NICHE collected from cohorts receiving (A) local (NICHE), (B) systemic (IP) or (C) no (CTRL) immunosuppression. (D) Fibrotic capsule thickness quantification. No transplant (NoTx) cohort refers to fibrotic capsule formed around NICHEs that did not receive cells or immunosuppression. Mean ± SD; One-way ANOVA; n.s.: not significant. Pan-leukocyte (CD45; magenta) and nuclear (DAPI: cyan) labeling of fibrotic capsule sections from (E) NICHE, (F) IP and (G) CTRL cohorts. (H) CD45+ cells expressed as percentage of total cells per field of view. Mean ± SD; One-way ANOVA.

A8 - Optical images of vascularized NICHE Optical images of NICHE incorporated in the subcutaneous tissue of rats 6 weeks post implantation with visible blood vessels (A) branching from the subcutaneous tissue and (B) penetrating into the cell reservoir. (C) Blood vessels branching inside the cell reservoir.

Bibliography

[1] M. Farina, J.F. Alexander, U. Thekkedath, M. Ferrari, A. Grattoni, Cell encapsulation: Overcoming barriers in cell transplantation in diabetes and beyond, Adv Drug Deliv Rev 139 (2019) 92-115.

[2] A. Gamble, A.R. Pepper, A. Bruni, A.M.J. Shapiro, The journey of islet cell transplantation and future development, Islets 10(2) (2018) 80-94.

[3] J.B. Sneddon, Q. Tang, P. Stock, J.A. Bluestone, S. Roy, T. Desai, M. Hebrok, Stem Cell Therapies for Treating Diabetes: Progress and Remaining Challenges, Cell Stem Cell 22(6) (2018) 810-823.

[4] M.R. Rickels, Stem Cell-Derived Islets: Next Steps for Histologic and Functional Assessment During Development as a Cellular Therapy for the Treatment of Diabetes, Diabetes 68(5) (2019) 901-903.

[5] E. Dolgin, Diabetes: Encapsulating the problem, Nature 540(7632) (2016) S60-S62.

[6] B. Ludwig, S. Ludwig, A. Steffen, Y. Knauf, B. Zimerman, S. Heinke, S. Lehmann, U. Schubert, J. Schmid, M. Bleyer, U. Schonmann, C.K. Colton, E. Bonifacio, M. Solimena, A. Reichel, A.V. Schally, A. Rotem, U. Barkai, H. Grinberg-Rashi, F.J. Kaup, Y. Avni, P. Jones, S.R. Bornstein, Favorable outcome of experimental islet xenotransplantation without immunosuppression in a nonhuman primate model of diabetes, Proc Natl Acad Sci U S A 114(44) (2017) 11745-11750.

[7] B. Ludwig, A. Reichel, A. Steffen, B. Zimerman, A.V. Schally, N.L. Block, C.K. Colton, S. Ludwig, S. Kersting, E. Bonifacio, M. Solimena, Z. Gendler, A. Rotem, U. Barkai, S.R. Bornstein, Transplantation of human islets without immunosuppression, Proc Natl Acad Sci U S A 110(47) (2013) 19054-8.

[8] P.O. Carlsson, D. Espes, A. Sedigh, A. Rotem, B. Zimerman, H. Grinberg, T. Goldman, U. Barkai, Y. Avni, G.T. Westermark, L. Carlbom, H. Ahlstrom, O. Eriksson, J. Olerud, O. Korsgren, Transplantation of macroencapsulated human islets within the bioartificial pancreas betaAir to patients with type 1 diabetes mellitus, Am J Transplant 18(7) (2018) 1735-1744.

[9] M.M. Hafiz, R.N. Faradji, T. Froud, A. Pileggi, D.A. Baidal, P. Cure, G. Ponte, R. Poggioli, A. Cornejo, S. Messinger, C. Ricordi, R. Alejandro, Immunosuppression and procedure-related complications in 26 patients with type 1 diabetes mellitus receiving allogeneic islet cell transplantation, Transplantation 80(12) (2005) 1718-28.

[10] N. Niclauss, D. Bosco, P. Morel, L. Giovannoni, T. Berney, G. Parnaud, Rapamycin impairs proliferation of transplanted islet beta cells, Transplantation 91(7) (2011) 714-22.

[11] J.R. Chapman, A.C. Webster, G. Wong, Cancer in the transplant recipient, Cold Spring Harb Perspect Med 3(7) (2013).

[12] J.A. Fishman, Opportunistic infections--coming to the limits of immunosuppression?, Cold Spring Harb Perspect Med 3(10) (2013) a015669.

[13] D.V. Dzhonova, R. Olariu, J. Leckenby, Y. Banz, J.C. Prost, A. Dhayani, P.K. Vemula, E. Voegelin, A. Taddeo, R. Rieben, Local Injections of Tacrolimus-loaded Hydrogel Reduce Systemic Immunosuppression-related Toxicity in Vascularized Composite Allotransplantation, Transplantation 102(10) (2018) 1684-1694.

[14] S.M. Stepkowski, S. Goto, T. Ito, K. Reynolds, R. Didlake, E.K. Kim, B.D. Kahan, Prolongation of heterotopic heart allograft survival by local delivery of continuous low-dose cyclosporine therapy, Transplantation 47(1) (1989) 17-23.

[15] K. Jiang, J.D. Weaver, Y. Li, X. Chen, J. Liang, C.L. Stabler, Local release of dexamethasone from macroporous scaffolds accelerates islet transplant engraftment by promotion of anti-inflammatory M2 macrophages, Biomaterials 114 (2017) 71-81.

[16] J.D. Weaver, Y. Song, E.Y. Yang, C. Ricordi, A. Pileggi, P. Buchwald, C.L. Stabler, Controlled Release of Dexamethasone from Organosilicone Constructs for Local Modulation of Inflammation in Islet Transplantation, Tissue Eng Part A 21(15-16) (2015) 2250-61.

[17] E. Pinto, B. Zhang, S. Song, N. Bodor, P. Buchwald, G. Hochhaus, Feasibility of localized immunosuppression: 2. PLA microspheres for the sustained local delivery of a soft immunosuppressant, Pharmazie 65(6) (2010) 429-35.

[18] P. Buchwald, N. Bocca, S. Marzorati, G. Hochhaus, N. Bodor, C. Stabler, N.S. Kenyon, L. Inverardi, R.D. Molano, C. Ricordi, A. Pileggi, Feasibility of localized immunosuppression: 1. Exploratory studies with glucocorticoids in a biohybrid device designed for cell transplantation, Pharmazie 65(6) (2010) 421-8.

[19] Y. Song, E. Margolles-Clark, C.A. Fraker, J.D. Weaver, C. Ricordi, A. Pileggi, C.L. Stabler, P. Buchwald, Feasibility of localized immunosuppression: 3. Preliminary evaluation of organosilicone constructs designed for sustained drug release in a cell transplant environment using dexamethasone, Pharmazie 67(5) (2012) 394-9.

[20] J. Paez-Mayorga, S. Capuani, N. Hernandez, M. Farina, C.Y.X. Chua, R. Blanchard, A. Sizovs, H.C. Liu, D.W. Fraga, J.A. Niles, H.F. Salazar, B. Corradetti, A.G. Sikora, M. Kloc, X.C. Li, A.O. Gaber, J.E. Nichols, A. Grattoni, Neovascularized implantable cell homing encapsulation platform with tunable local immunosuppressant delivery for allogeneic cell transplantation, Biomaterials 257 (2020) 120232.

[21] M. Farina, C.Y.X. Chua, A. Ballerini, U. Thekkedath, J.F. Alexander, J.R. Rhudy, G. Torchio, D. Fraga, R.R. Pathak, M. Villanueva, C.S. Shin, J.A. Niles, R. Sesana, D. Demarchi, A.G. Sikora, G.S. Acharya, A.O. Gaber, J.E. Nichols, A. Grattoni, Transcutaneously refillable, 3D-printed biopolymeric encapsulation system for the transplantation of endocrine cells, Biomaterials 177 (2018) 125-138.

[22] J.E. Nichols, J.A. Niles, D. DeWitt, D. Prough, M. Parsley, S. Vega, A. Cantu, E. Lee, J. Cortiella, Neurogenic and neuro-protective potential of a novel subpopulation of peripheral blood-derived CD133+ ABCG2+CXCR4+ mesenchymal stem cells: development of autologous cell-based therapeutics for traumatic brain injury, Stem Cell Res Ther 4(1) (2013) 3.

[23] J.E. Nichols, S. La Francesca, S.P. Vega, J.A. Niles, L.B. Argueta, M. Riddle, J. Sakamoto, G. Vargas, R. Pal, L. Woodson, J. Rhudy, D. Lee, D. Seanor, G. Campbell, V. Schnadig, J. Cortiella, Giving new life to old lungs: methods to produce and assess whole human paediatric bioengineered lungs, J Tissue Eng Regen Med 11(7) (2017) 2136-2152.

[24] J.E. Nichols, J. Niles, M. Riddle, G. Vargas, T. Schilagard, L. Ma, K. Edward, S. La Francesca, J. Sakamoto, S. Vega, M. Ogadegbe, R. Mlcak, D. Deyo, L. Woodson, C. McQuitty, S. Lick, D. Beckles, E. Melo, J. Cortiella, Production and assessment

of decellularized pig and human lung scaffolds, Tissue Eng Part A 19(17-18) (2013) 2045-62.

[25] G. Mattsson, P.O. Carlsson, K. Olausson, L. Jansson, Histological markers for endothelial cells in endogenous and transplanted rodent pancreatic islets, Pancreatology 2(2) (2002) 155-62.

[26] M. Farina, A. Ballerini, D. Fraga, U. Thekkedath, O. Sabek, A.O. Gaber, A. Grattoni, Implantable 3D Printed Encapsulation System for Cell Transplantation, Organogenesis and Drug Release, Patent No. PCT/US2018/056203, Apr 25, 2019.

[27] A. Gregor, E. Filova, M. Novak, J. Kronek, H. Chlup, M. Buzgo, V. Blahnova, V. Lukasova, M. Bartos, A. Necas, J. Hosek, Designing of PLA scaffolds for bone tissue replacement fabricated by ordinary commercial 3D printer, J Biol Eng 11 (2017) 31.

[28] M. Shah Mohammadi, M.N. Bureau, S.N. Nazhat, Polylactic acid (PLA) biomedical foams for tissue engineering, Biomedical Foams for Tissue Engineering Applications2014, pp. 313-334.

[29] K. Tappa, U. Jammalamadaka, Novel Biomaterials Used in Medical 3D Printing Techniques, J Funct Biomater 9(1) (2018).

[30] D. da Silva, M. Kaduri, M. Poley, O. Adir, N. Krinsky, J. Shainsky-Roitman, A. Schroeder, Biocompatibility, biodegradation and excretion of polylactic acid (PLA) in medical implants and theranostic systems, Chem Eng J 340 (2018) 9-14.

[31] M. Winnacker, Polyamides and their functionalization: recent concepts for their applications as biomaterials, Biomater Sci 5(7) (2017) 1230-1235.

[32] Y. Kawakami, H. Iwata, Y.J. Gu, M. Miyamoto, Y. Murakami, A.N. Balamurugan, M. Imamura, K. Inoue, Successful subcutaneous pancreatic islet transplantation using an angiogenic growth factor-releasing device, Pancreas 23(4) (2001) 375-81.

[33] A.R. Pepper, B. Gala-Lopez, R. Pawlick, S. Merani, T. Kin, A.M. Shapiro, A prevascularized subcutaneous device-less site for islet and cellular transplantation, Nat Biotechnol 33(5) (2015) 518-23.

[34] J. Etulain, H.A. Mena, R.P. Meiss, G. Frechtel, S. Gutt, S. Negrotto, M. Schattner, An optimised protocol for platelet-rich plasma preparation to improve its angiogenic and regenerative properties, Sci Rep 8(1) (2018) 1513.

[35] J. Kurita, M. Miyamoto, Y. Ishii, J. Aoyama, G. Takagi, Z. Naito, Y. Tabata, M. Ochi, K. Shimizu, Enhanced vascularization by controlled release of platelet-rich plasma impregnated in biodegradable gelatin hydrogel, Ann Thorac Surg 92(3) (2011) 837-44; discussion 844.

[36] A.J. Melchiorri, B.N. Nguyen, J.P. Fisher, Mesenchymal stem cells: roles and relationships in vascularization, Tissue Eng Part B Rev 20(3) (2014) 218-28.

[37] M. Wang, Q. Yuan, L. Xie, Mesenchymal Stem Cell-Based Immunomodulation: Properties and Clinical Application, Stem Cells Int 2018 (2018) 3057624.

[38] M. Johansson, L. Jansson, P.O. Carlsson, Improved vascular engraftment and function of autotransplanted pancreatic islets as a result of partial pancreatectomy in the mouse and rat, Diabetologia 50(6) (2007) 1257-66.

[39] G. Mattsson, L. Jansson, P.O. Carlsson, Decreased vascular density in mouse pancreatic islets after transplantation, Diabetes 51(5) (2002) 1362-6.

[40] R.A. Stokes, K. Cheng, A. Lalwani, M.M. Swarbrick, H.E. Thomas, T. Loudovaris, T.W. Kay, W.J. Hawthorne, P.J. O'Connell, J.E. Gunton, Transplantation sites for human and murine islets, Diabetologia 60(10) (2017) 1961-1971.

[41] A.R. Pepper, B. Gala-Lopez, O. Ziff, A.M.J. Shapiro, Revascularization of Transplanted Pancreatic Islets and Role of the Transplantation Site, Clinical and Developmental Immunology 2013 (2013) 352315.

[42] E. Kargar-Abarghouei, Z. Vojdani, A. Hassanpour, S. Alaee, T. Talaei-Khozani, Characterization, recellularization, and transplantation of rat decellularized testis scaffold with bone marrow-derived mesenchymal stem cells, Stem Cell Res Ther 9(1) (2018) 324.

[43] R. Cheng, J.X. Ma, Angiogenesis in diabetes and obesity, Rev Endocr Metab Disord 16(1) (2015) 67-75.

[44] K.L. Helton, B.D. Ratner, N.A. Wisniewski, Biomechanics of the sensor-tissue interface-effects of motion, pressure, and design on sensor performance and the foreign body response-part I: theoretical framework, J Diabetes Sci Technol 5(3) (2011) 632-46.

[45] J.M. Anderson, A. Rodriguez, D.T. Chang, Foreign body reaction to biomaterials, Semin Immunol 20(2) (2008) 86-100.

[46] S.H. Woo, H.S. Jeong, J.P. Kim, E.H. Koh, S.U. Lee, S.M. Jin, D.H. Kim, J.H. Sohn, S.H. Lee, Favorable vocal fold wound healing induced by platelet-rich plasma injection, Clin Exp Otorhinolaryngol 7(1) (2014) 47-52.

[47] N. Serizawa, Y. Funasaka, H. Goto, A. Kanzaki, J. Hori, Y. Takano, H. Saeki, Platelet-Rich Plasma Injection and Cutaneous Sarcoidal Granulomas, Ann Dermatol 29(2) (2017) 239-241.

[48] S. Hu, P. de Vos, Polymeric Approaches to Reduce Tissue Responses Against Devices Applied for Islet-Cell Encapsulation, Front Bioeng Biotechnol 7 (2019) 134.

[49] B.D. Hori, R.J. Petrell, A.W. Trites, T. Godbey, Lamination for subdermal implant fixation, J Biomed Mater Res B Appl Biomater 91(1) (2009) 17-25.

[50] O.M. Sabek, M. Farina, D.W. Fraga, S. Afshar, A. Ballerini, C.S. Filgueira, U.R. Thekkedath, A. Grattoni, A.O. Gaber, Three-dimensional printed polymeric system to encapsulate human mesenchymal stem cells differentiated into islet-like insulin-producing aggregates for diabetes treatment, J Tissue Eng 7 (2016) 2041731416638198.

[51] M. Farina, A. Ballerini, D.W. Fraga, E. Nicolov, M. Hogan, D. Demarchi, F. Scaglione, O.M. Sabek, P. Horner, U. Thekkedath, O.A. Gaber, A. Grattoni, 3D Printed Vascularized Device for Subcutaneous Transplantation of Human Islets, Biotechnol J 12(9) (2017).

[52] O.M. Sabek, S. Ferrati, D.W. Fraga, J. Sih, E.V. Zabre, D.H. Fine, M. Ferrari, A.O. Gaber, A. Grattoni, Characterization of a nanogland for the autotransplantation of human pancreatic islets, Lab Chip 13(18) (2013) 3675-88.

[53] R.K. Jain, P. Au, J. Tam, D.G. Duda, D. Fukumura, Engineering vascularized tissue, Nat Biotechnol 23(7) (2005) 821-3.

[54] B.M. Prior, H.T. Yang, R.L. Terjung, What makes vessels grow with exercise training?, J Appl Physiol (1985) 97(3) (2004) 1119-28.

[55] N.Y. Li, R.T. Yuan, T. Chen, L.Q. Chen, X.M. Jin, Effect of platelet-rich plasma and latissimus dorsi muscle flap on osteogenesis and vascularization of tissue-engineered bone in dogs, J Oral Maxillofac Surg 67(9) (2009) 1850-8.

[56] V. Hertig, K. Tardif, M.A. Meus, N. Duquette, L. Villeneuve, F. Toussaint, J. Ledoux, A. Calderone, Nestin expression is upregulated in the fibrotic rat heart and

is localized in collagen-expressing mesenchymal cells and interstitial CD31(+)- cells, PLoS One 12(4) (2017) e0176147.

[57] S. Li, D. Tay, S. Shu, X. Bao, Y. Wu, X. Wang, H.K. Yip, Endothelial nitric oxide synthase is expressed in amacrine cells of developing human retinas, Invest Ophthalmol Vis Sci 47(5) (2006) 2141-9.

[58] T.N. Castillo, M.A. Pouliot, H.J. Kim, J.L. Dragoo, Comparison of growth factor and platelet concentration from commercial platelet-rich plasma separation systems, Am J Sports Med 39(2) (2011) 266-71.

[59] L.A. Gomez, M. Escobar, O. Penuela, Standardization of a Protocol for Obtaining Platelet Rich Plasma from blood Donors; a Tool for Tissue Regeneration Procedures, Clin Lab 61(8) (2015) 973-80.

[60] S.H. Ramaswamy Reddy, R. Reddy, N.C. Babu, G.N. Ashok, Stem-cell therapy and platelet-rich plasma in regenerative medicines: A review on pros and cons of the technologies, J Oral Maxillofac Pathol 22(3) (2018) 367-374.

[61] S.S. Lin, R. Landesberg, H.S. Chin, J. Lin, S.B. Eisig, H.H. Lu, Controlled release of PRP-derived growth factors promotes osteogenic differentiation of human mesenchymal stem cells, Conf Proc IEEE Eng Med Biol Soc 2006 (2006) 4358-61.

[62] H.R. Hofer, R.S. Tuan, Secreted trophic factors of mesenchymal stem cells support neurovascular and musculoskeletal therapies, Stem Cell Res Ther 7(1) (2016) 131.

[63] H. Tao, Z. Han, Z.C. Han, Z. Li, Proangiogenic Features of Mesenchymal Stem Cells and Their Therapeutic Applications, Stem Cells Int 2016 (2016) 1314709.

[64] A.D.K. Le, L. Enweze, M.R. DeBaun, J.L. Dragoo, Current Clinical Recommendations for Use of Platelet-Rich Plasma, Curr Rev Musculoskelet Med 11(4) (2018) 624-634.

[65] M. Kabat, I. Bobkov, S. Kumar, M. Grumet, Trends in mesenchymal stem cell clinical trials 2004-2018: Is efficacy optimal in a narrow dose range?, Stem Cells Transl Med 9(1) (2020) 17-27.

[66] X.L. Fan, Y. Zhang, X. Li, Q.L. Fu, Mechanisms underlying the protective effects of mesenchymal stem cell-based therapy, Cell Mol Life Sci (2020).

[67] M.F. Pittenger, D.E. Discher, B.M. Peault, D.G. Phinney, J.M. Hare, A.I. Caplan, Mesenchymal stem cell perspective: cell biology to clinical progress, NPJ Regen Med 4 (2019) 22.

[68] J.J. Rajesh, J. Bijwe, B. Venkataraman, U.S. Tewari, Effect of water absorption on erosive wear behaviour of polyamides, Journal of Materials Science 37(23) (2002) 5107-5113.

[69] A.J.T. Teo, A. Mishra, I. Park, Y.-J. Kim, W.-T. Park, Y.-J. Yoon, Polymeric Biomaterials for Medical Implants and Devices, ACS Biomaterials Science & Engineering 2(4) (2016) 454-472.

[70] K. Jones, Fibrotic Response to Biomaterials and all Associated Sequence of Fibrosis, Host Response to Biomaterials2015, pp. 189-237.

[71] S. Farah, J.C. Doloff, P. Muller, A. Sadraei, H.J. Han, K. Olafson, K. Vyas, H.H. Tam, J. Hollister-Lock, P.S. Kowalski, M. Griffin, A. Meng, M. McAvoy, A.C. Graham, J. McGarrigle, J. Oberholzer, G.C. Weir, D.L. Greiner, R. Langer, D.G. Anderson, Long-term implant fibrosis prevention in rodents and non-human primates using crystallized drug formulations, Nat Mater 18(8) (2019) 892-904.

[72] F.P. Pons-Faudoa, A. Sizovs, N. Di Trani, J. Paez-Mayorga, G. Bruno, J. Rhudy, M. Manohar, K. Gwenden, C. Martini, C.Y.X. Chua, G. Varchi, M.A. Marzinke, A. Grattoni, 2-Hydroxypropyl-beta-cyclodextrin-enhanced pharmacokinetics of cabotegravir from a nanofluidic implant for HIV pre-exposure prophylaxis, J Control Release 306 (2019) 89-96.

[73] S.M. Watt, F. Gullo, M. van der Garde, D. Markeson, R. Camicia, C.P. Khoo, J.J. Zwaginga, The angiogenic properties of mesenchymal stem/stromal cells and their therapeutic potential, Br Med Bull 108 (2013) 25-53.

[74] I.R. Badell, G.M. Karadkhele, P. Vasanth, A.B. Farris, 3rd, J.M. Robertson, C.P. Larsen, Abatacept as rescue immunosuppression after calcineurin inhibitor treatment failure in renal transplantation, Am J Transplant (2019).

[75] C. Schwarz, L. Unger, B. Mahr, K. Aumayr, H. Regele, A.M. Farkas, K. Hock, N. Pilat, T. Wekerle, The Immunosuppressive Effect of CTLA4 Immunoglobulin Is Dependent on Regulatory T Cells at Low But Not High Doses, Am J Transplant 16(12) (2016) 3404-3415.

[76] R. Bahri, A. Naji, C. Menier, B. Charpentier, E.D. Carosella, N. Rouas-Freiss, A. Durrbach, Dendritic cells secrete the immunosuppressive HLA-G molecule upon CTLA4-Ig treatment: implication in human renal transplant acceptance, J Immunol 183(11) (2009) 7054-62.

[77] D.I. Stoia, E. Linul, L. Marsavina, Influence of Manufacturing Parameters on Mechanical Properties of Porous Materials by Selective Laser Sintering, Materials (Basel) 12(6) (2019).

[78] S.C. Ligon, R. Liska, J. Stampfl, M. Gurr, R. Mulhaupt, Polymers for 3D Printing and Customized Additive Manufacturing, Chem Rev 117(15) (2017) 10212-10290.

[79] M.F. Maitz, Applications of synthetic polymers in clinical medicine, Biosurface and Biotribology 1(3) (2015) 161-176.

[80] A. Espona-Noguera, J. Ciriza, A. Canibano-Hernandez, R. Villa, L. Saenz Del Burgo, M. Alvarez, J.L. Pedraz, 3D printed polyamide macroencapsulation devices combined with alginate hydrogels for insulin-producing cell-based therapies, Int J Pharm 566 (2019) 604-614.

[81] F.P. Pons-Faudoa, A. Ballerini, J. Sakamoto, A. Grattoni, Advanced implantable drug delivery technologies: transforming the clinical landscape of therapeutics for chronic diseases, Biomed Microdevices 21(2) (2019) 47.

[82] M. Lovett, K. Lee, A. Edwards, D.L. Kaplan, Vascularization strategies for tissue engineering, Tissue Eng Part B Rev 15(3) (2009) 353-70.

[83] J. Rouwkema, B. Koopman, C. Blitterswijk, W. Dhert, J. Malda, Supply of nutrients to cells in engineered tissues, Biotechnol Genet Eng Rev 26 (2010) 163-78.

[84] S. Li, Y.Y. Liu, L.J. Liu, Q.X. Hu, A Versatile Method for Fabricating Tissue Engineering Scaffolds with a Three-Dimensional Channel for Prevasculature Networks, ACS Appl Mater Interfaces 8(38) (2016) 25096-103.

[85] S. Landau, S. Guo, S. Levenberg, Localization of Engineered Vasculature within 3D Tissue Constructs, Front Bioeng Biotechnol 6 (2018) 2.

[86] M. Groot Nibbelink, K. Skrzypek, L. Karbaat, S. Both, J. Plass, B. Klomphaar, J. van Lente, S. Henke, M. Karperien, D. Stamatialis, A. van Apeldoorn, An important step towards a prevascularized islet microencapsulation device: in vivo

prevascularization by combination of mesenchymal stem cells on micropatterned membranes, J Mater Sci Mater Med 29(11) (2018) 174.

[87] U. Johansson, I. Rasmusson, S.P. Niclou, N. Forslund, L. Gustavsson, B. Nilsson, O. Korsgren, P.U. Magnusson, Formation of composite endothelial cell-mesenchymal stem cell islets: a novel approach to promote islet revascularization, Diabetes 57(9) (2008) 2393-401.

[88] J.J. Moon, J.L. West, Vascularization of engineered tissues: approaches to promote angio-genesis in biomaterials, Curr Top Med Chem 8(4) (2008) 300-10.

[89] J. Svensson, J. Lau, M. Sandberg, P.O. Carlsson, High vascular density and oxygenation of pancreatic islets transplanted in clusters into striated muscle, Cell Transplant 20(5) (2011) 783-8.

[90] L. Jansson, A. Barbu, B. Bodin, C.J. Drott, D. Espes, X. Gao, L. Grapensparr, O. Kallskog, J. Lau, H. Liljeback, F. Palm, M. Quach, M. Sandberg, V. Stromberg, S. Ullsten, P.O. Carlsson, Pancreatic islet blood flow and its measurement, Ups J Med Sci 121(2) (2016) 81-95.

[91] M.D. Sarker, S. Naghieh, N.K. Sharma, L. Ning, X. Chen, Bioprinting of Vascularized Tissue Scaffolds: Influence of Biopolymer, Cells, Growth Factors, and Gene Delivery, J Healthc Eng 2019 (2019) 9156921.

[92] R. Diehl, F. Ferrara, C. Muller, A.Y. Dreyer, D.D. McLeod, S. Fricke, J. Boltze, Immunosuppression for in vivo research: state-of-the-art protocols and experimental approaches, Cell Mol Immunol 14(2) (2017) 146-179.

[93] A.D. Barlow, M.L. Nicholson, T.P. Herbert, Evidence for rapamycin toxicity in pancreatic beta-cells and a review of the underlying molecular mechanisms, Diabetes 62(8) (2013) 2674-82.

[94] J.A. Bluestone, E.W. St Clair, L.A. Turka, CTLA4Ig: bridging the basic immunology with clinical application, Immunity 24(3) (2006) 233-8.

[95] F. Vincenti, Costimulation blockade in autoimmunity and transplantation, J Allergy Clin Immunol 121(2) (2008) 299-306; quiz 307-8.

[96] M.J. Bernett, S.Y. Chu, I. Leung, G.L. Moore, S.H. Lee, E. Pong, H. Chen, S. Phung, U.S. Muchhal, H.M. Horton, G.A. Lazar, J.R. Desjarlais, D.E. Szymkowski, Immune suppression in cynomolgus monkeys by XPro9523: an improved CTLA4-Ig fusion with enhanced binding to CD80, CD86 and neonatal Fc receptor FcRn, MAbs 5(3) (2013) 384-96.

[97] Y. Chen, T. Fukuda, M.S. Thakar, B.T. Kornblit, B.E. Storer, E.B. Santos, R. Storb, B.M. Sandmaier, Immunomodulatory effects induced by cytotoxic T lymphocyte antigen 4 immunoglobulin with donor peripheral blood mononuclear cell infusion in canine major histocompatibility complex-haplo-identical non-myeloablative hematopoietic cell transplantation, Cytotherapy 13(10) (2011) 1269-80.

[98] Y. Ma, B.R. Lin, B. Lin, S. Hou, W.Z. Qian, J. Li, M. Tan, J. Ma, B.H. Li, H. Wang, A.D. Wen, Y.J. Guo, Pharmacokinetics of CTLA4Ig fusion protein in healthy volunteers and patients with rheumatoid arthritis, Acta Pharmacol Sin 30(3) (2009) 364-71.

[99] B. Cooper-Jones, C. Ford, Islet Cell Replacement Therapy for Insulin-Dependent Diabetes, CADTH Issues in Emerging Health Technologies, Ottawa (ON), 2016, pp. 1-9.

[100] T. Desai, L.D. Shea, Advances in islet encapsulation technologies, Nat Rev Drug Discov 16(5) (2017) 338-350.

[101] K. Patel, C. Atkinson, D. Tran, S.N. Nadig, Nanotechnological Approaches to Immunosuppression and Tolerance Induction, Curr Transplant Rep 4(2) (2017) 159-168.

[102] E. Tasciotti, F.J. Cabrera, M. Evangelopoulos, J.O. Martinez, U.R. Thekkedath, M. Kloc, R.M. Ghobrial, X.C. Li, A. Grattoni, M. Ferrari, The Emerging Role of Nanotechnology in Cell and Organ Transplantation, Transplantation 100(8) (2016) 1629-38.

[103] T. Laumonier, N. Potiron, F. Boeffard, C. Chagneau, S. Brouard, C. Guillot, J.P. Soulillou, I. Anegon, B. Le Mauff, CTLA4Ig adenoviral gene transfer induces long-term islet rat allograft survival, without tolerance, after systemic but not local intragraft expression, Hum Gene Ther 14(6) (2003) 561-75.

[104] A. Benigni, S. Tomasoni, L.A. Turka, L. Longaretti, L. Zentilin, M. Mister, A. Pezzotta, N. Azzollini, M. Noris, S. Conti, M. Abbate, M. Giacca, G. Remuzzi, Adeno-associated virus-mediated CTLA4Ig gene transfer protects MHC-mismatched renal allografts from chronic rejection, J Am Soc Nephrol 17(6) (2006) 1665-72.

[105] R.M. Comer, W.J. King, N. Ardjomand, S. Theoharis, A.J. George, D.F. Larkin, Effect of administration of CTLA4-Ig as protein or cDNA on corneal allograft survival, Invest Ophthalmol Vis Sci 43(4) (2002) 1095-103.

[106] W. Zhang, V.S. Gorantla, P.G. Campbell, Y. Li, Y. Yang, C. Komatsu, L.E. Weiss, X.X. Zheng, M.G. Solari, Biopatterned CTLA4/Fc Matrices Facilitate Local Immunomodulation, Engraftment, and Glucose Homeostasis After Pancreatic Islet Transplantation, Diabetes 65(12) (2016) 3660.

[107] M. Brissova, A. Shostak, M. Shiota, P.O. Wiebe, G. Poffenberger, J. Kantz, Z. Chen, C. Carr, W.G. Jerome, J. Chen, H.S. Baldwin, W. Nicholson, D.M. Bader, T. Jetton, M. Gannon, A.C. Powers, Pancreatic islet production of vascular endothelial growth factor--a is essential for islet vascularization, revascularization, and function, Diabetes 55(11) (2006) 2974-85.

[108] G.G. Pinkse, W.P. Bouwman, R. Jiawan-Lalai, O.T. Terpstra, J.A. Bruijn, E. de Heer, Integrin signaling via RGD peptides and anti-beta1 antibodies confers resistance to apoptosis in islets of Langerhans, Diabetes 55(2) (2006) 312-7.

[109] L.A. Llacua, M.M. Faas, P. de Vos, Extracellular matrix molecules and their potential contribution to the function of transplanted pancreatic islets, Diabetologia 61(6) (2018) 1261-1272.

[110] L.M. Weber, K.N. Hayda, K.S. Anseth, Cell-matrix interactions improve beta-cell survival and insulin secretion in three-dimensional culture, Tissue Eng Part A 14(12) (2008) 1959-68.

[111] C.H. Stephens, K.S. Orr, A.J. Acton, S.A. Tersey, R.G. Mirmira, R.V. Considine, S.L. Voytik-Harbin, In situ type I oligomeric collagen macroencapsulation promotes islet longevity and function in vitro and in vivo, Am J Physiol Endocrinol Metab 315(4) (2018) E650-E661.

[112] M.G. McCoy, B.R. Seo, S. Choi, C. Fischbach, Collagen I hydrogel microstructure and composition conjointly regulate vascular network formation, Acta Biomater 44 (2016) 200-8.

[113] D. Isackson, K.J. Cook, L.D. McGill, K.N. Bachus, Mesenchymal stem cells increase collagen infiltration and improve wound healing response to porous titanium percutaneous implants, Med Eng Phys 35(6) (2013) 743-53.

[114] M. Ben Nasr, A. Vergani, J. Avruch, L. Liu, E. Kefaloyianni, F. D'Addio, S. Tezza, D. Corradi, R. Bassi, A. Valderrama-Vasquez, V. Usuelli, J. Kim, J. Azzi, B. El Essawy, J. Markmann, R. Abdi, P. Fiorina, Co-transplantation of autologous MSCs delays islet allograft rejection and generates a local immunoprivileged site, Acta Diabetol 52(5) (2015) 917-27.

[115] H. Li, S. Shen, H. Fu, Z. Wang, X. Li, X. Sui, M. Yuan, S. Liu, G. Wang, Q. Guo, Immunomodulatory Functions of Mesenchymal Stem Cells in Tissue Engineering, Stem Cells International 2019 (2019) 18.

[116] B.M. de Souza, A.P. Boucas, F.D. Oliveira, K.P. Reis, P. Ziegelmann, A.C. Bauer, D. Crispim, Effect of co-culture of mesenchymal stem/stromal cells with pancreatic islets on viability and function outcomes: a systematic review and meta-analysis, Islets 9(2) (2017) 30-42.

[117] A. Gamble, R. Pawlick, A.R. Pepper, A. Bruni, A. Adesida, P.A. Senior, G.S. Korbutt, A.M.J. Shapiro, Improved islet recovery and efficacy through co-culture and co-transplantation of islets with human adipose-derived mesenchymal stem cells, PLoS One 13(11) (2018) e0206449.

[118] V. Vaithilingam, M.D.M. Evans, D.M. Lewy, P.A. Bean, S. Bal, B.E. Tuch, Co-encapsulation and co-transplantation of mesenchymal stem cells reduces pericapsular fibrosis and improves encapsulated islet survival and function when allografted, Sci Rep 7(1) (2017) 10059.

[119] T.Y. Yeung, K.L. Seeberger, T. Kin, A. Adesida, N. Jomha, A.M. Shapiro, G.S. Korbutt, Human mesenchymal stem cells protect human islets from pro-inflammatory cytokines, PLoS One 7(5) (2012) e38189.

[120] Orencia [package insert], Bristol-Myers Squibb Company, Princeton, NJ, 2017.

[121] K.L. Hardinger, D. Sunderland, J.A. Wiederrich, Belatacept for the prophylaxis of organ rejection in kidney transplant patients: an evidence-based review of its place in therapy, Int J Nephrol Renovasc Dis 9 (2016) 139-50.

[122] A.B. Adams, N. Shirasugi, M.M. Durham, E. Strobert, D. Anderson, P. Rees, S. Cowan, H. Xu, Y. Blinder, M. Cheung, D. Hollenbaugh, N.S. Kenyon, T.C. Pearson, C.P. Larsen, Calcineurin inhibitor-free CD28 blockade-based protocol protects allogeneic islets in nonhuman primates, Diabetes 51(2) (2002) 265-70.

[123] M. Lowe, I.R. Badell, P. Thompson, B. Martin, F. Leopardi, E. Strobert, A.A. Price, H.S. Abdulkerim, R. Wang, N.N. Iwakoshi, A.B. Adams, A.D. Kirk, C.P. Larsen, K.A. Reimann, A novel monoclonal antibody to CD40 prolongs islet allograft survival, Am J Transplant 12(8) (2012) 2079-87.

[124] I.R. Badell, M.C. Russell, K. Cardona, V.O. Shaffer, A.P. Turner, J.G. Avila, J.A. Cano, F.V. Leopardi, M. Song, E.A. Strobert, M.L. Ford, T.C. Pearson, A.D. Kirk, C.P. Larsen, CTLA4Ig prevents alloantibody formation following nonhuman primate islet transplantation using the CD40-specific antibody 3A8, Am J Transplant 12(7) (2012) 1918-23.

[125] A.B. Adams, N. Shirasugi, T.R. Jones, M.M. Durham, E.A. Strobert, S. Cowan, P. Rees, R. Hendrix, K. Price, N.S. Kenyon, D. Hagerty, R. Townsend, D. Hollenbaugh, T.C. Pearson, C.P. Larsen, Development of a chimeric anti-CD40

monoclonal antibody that synergizes with LEA29Y to prolong islet allograft survival, J Immunol 174(1) (2005) 542-50.

[126] A.M. Posselt, G.L. Szot, L.A. Frassetto, U. Masharani, M. Tavakol, R. Amin, J. McElroy, M.D. Ramos, R.K. Kerlan, L. Fong, F. Vincenti, J.A. Bluestone, P.G. Stock, Islet transplantation in type 1 diabetic patients using calcineurin inhibitor-free immunosuppressive protocols based on T-cell adhesion or costimulation blockade, Transplantation 90(12) (2010) 1595-601.

[127] A.D. Kirk, D.M. Harlan, N.N. Armstrong, T.A. Davis, Y. Dong, G.S. Gray, X. Hong, D. Thomas, J.H. Fechner, Jr., S.J. Knechtle, CTLA4-Ig and anti-CD40 ligand prevent renal allograft rejection in primates, Proc Natl Acad Sci U S A 94(16) (1997) 8789-94.

[128] M.M. Kho, A.P. Bouvy, M. Cadogan, R. Kraaijeveld, C.C. Baan, W. Weimar, The effect of low and ultra-low dosages Thymoglobulin on peripheral T, B and NK cells in kidney transplant recipients, Transpl Immunol 26(4) (2012) 186-90.

[129] N. Kroger, T. Zabelina, W. Kruger, H. Renges, N. Stute, J. Rischewski, S. Sonnenberg, F. Ayuk, F. Togel, U. Schade, H. Fiegel, R. Erttmann, C. Loliger, A.R. Zander, In vivo T cell depletion with pretransplant anti-thymocyte globulin reduces graft-versus-host disease without increasing relapse in good risk myeloid leukemia patients after stem cell transplantation from matched related donors, Bone Marrow Transplant 29(8) (2002) 683-9.

[130] M. Remberger, B.M. Svahn, J. Mattsson, O. Ringden, Dose study of thymoglobulin during conditioning for unrelated donor allogeneic stem-cell transplantation, Transplantation 78(1) (2004) 122-7.

[131] F.P. Machado, A.R. Vicari, F. Spuldaro, J.B.S. Castro Filho, R.C. Manfro, Polyclonal anti T-lymphocyte antibody therapy monitoring in kidney transplant recipients: comparison of CD3+ T cell and total lymphocyte counts, Einstein (Sao Paulo) 16(4) (2018) eAO4278.

[132] K. Nanmoku, T. Shinzato, T. Kubo, T. Shimizu, T. Yagisawa, Effect of Rabbit Antithymocyte Globulin on Acute and Chronic Active Antibody-Mediated Rejection After Kidney Transplantation, Transplant Proc 51(8) (2019) 2602-2605.

[133] X. Feng, P. Scheinberg, A. Biancotto, O. Rios, S. Donaldson, C. Wu, H. Zheng, K. Sato, D.M. Townsley, J.P. McCoy, N.S. Young, In vivo effects of horse and rabbit antithymocyte globulin in patients with severe aplastic anemia, Haematologica 99(9) (2014) 1433-40.

[134] F. D'Addio, O. Boenisch, C.N. Magee, M.Y. Yeung, X. Yuan, B. Mfarrej, A. Vergani, M.J. Ansari, P. Fiorina, N. Najafian, Prolonged, low-dose anti-thymocyte globulin, combined with CTLA4-Ig, promotes engraftment in a stringent transplant model, PLoS One 8(1) (2013) e53797.

[135] A.M. Shapiro, J.R. Lakey, E.A. Ryan, G.S. Korbutt, E. Toth, G.L. Warnock, N.M. Kneteman, R.V. Rajotte, Islet transplantation in seven patients with type 1 diabetes mellitus using a glucocorticoid-free immunosuppressive regimen, N Engl J Med 343(4) (2000) 230-8.

[136] J. Trinanes, A.E. Rodriguez-Rodriguez, Y. Brito-Casillas, A. Wagner, A.P.J. De Vries, G. Cuesto, A. Acebes, E. Salido, A. Torres, E. Porrini, Deciphering Tacrolimus-Induced Toxicity in Pancreatic beta Cells, Am J Transplant 17(11) (2017) 2829-2840.

[137] U. Kaundal, U. Bagai, A. Rakha, Immunomodulatory plasticity of mesenchymal stem cells: a potential key to successful solid organ transplantation, J Transl Med 16(1) (2018) 31.

[138] Y.M. Pers, M. Ruiz, D. Noel, C. Jorgensen, Mesenchymal stem cells for the management of inflammation in osteoarthritis: state of the art and perspectives, Osteoarthritis Cartilage 23(11) (2015) 2027-35.

[139] Q. Zhao, H. Ren, Z. Han, Mesenchymal stem cells: Immunomodulatory capability and clinical potential in immune diseases, 2(1) (2016) 3-20.

[140] N. Jetten, S. Verbruggen, M.J. Gijbels, M.J. Post, M.P. De Winther, M.M. Donners, Anti-inflammatory M2, but not pro-inflammatory M1 macrophages promote angiogenesis in vivo, Angiogenesis 17(1) (2014) 109-18.

[141] K. Guo, S. Ikehara, X. Meng, Mesenchymal stem cells for inducing tolerance in organ transplantation, Front Cell Dev Biol 2 (2014) 8.

[142] J.W. Lee, X. Fang, A. Krasnodembskaya, J.P. Howard, M.A. Matthay, Concise review: Mesenchymal stem cells for acute lung injury: role of paracrine soluble factors, Stem Cells 29(6) (2011) 913-9.

[143] D.M. Berman, M.A. Willman, D. Han, G. Kleiner, N.M. Kenyon, O. Cabrera, J.A. Karl, R.W. Wiseman, D.H. O'Connor, A.M. Bartholomew, N.S. Kenyon, Mesenchymal stem cells enhance allogeneic islet engraftment in nonhuman primates, Diabetes 59(10) (2010) 2558-68.

[144] Y. Ding, D. Xu, G. Feng, A. Bushell, R.J. Muschel, K.J. Wood, Mesenchymal stem cells prevent the rejection of fully allogenic islet grafts by the immunosuppressive activity of matrix metalloproteinase-2 and -9, Diabetes 58(8) (2009) 1797-806.

[145] S. Forbes, A.R. Bond, K.L. Thirlwell, P. Burgoyne, K. Samuel, J. Noble, G. Borthwick, D. Colligan, N.W.A. McGowan, P.S. Lewis, A.R. Fraser, J.C. Mountford, R.N. Carter, N.M. Morton, M.L. Turner, G.J. Graham, J.D.M. Campbell, Human umbilical cord perivascular cells improve human pancreatic islet transplant function by increasing vascularization, Sci Transl Med 12(526) (2020).

[146] E.J. Jung, S.C. Kim, Y.M. Wee, Y.H. Kim, M.Y. Choi, S.H. Jeong, J. Lee, D.G. Lim, D.J. Han, Bone marrow-derived mesenchymal stromal cells support rat pancreatic islet survival and insulin secretory function in vitro, Cytotherapy 13(1) (2011) 19-29.

[147] J. Cho, M. D'Antuono, M. Glicksman, J. Wang, J. Jonklaas, A review of clinical trials: mesenchymal stem cell transplant therapy in type 1 and type 2 diabetes mellitus, Am J Stem Cells 7(4) (2018) 82-93.

[148] R. Kogawa, K. Nakamura, Y. Mochizuki, A New Islet Transplantation Method Combining Mesenchymal Stem Cells with Recombinant Peptide Pieces, Microencapsulated Islets, and Mesh Bags, Biomedicines 8(9) (2020).

[149] M.J. Smelt, M.M. Faas, B.J. de Haan, P. de Vos, Pancreatic beta-cell purification by altering FAD and NAD(P)H metabolism, Exp Diabetes Res 2008 (2008) 165360.

[150] D.A. Coddington, H. Yang, G. Rowden, P. Colp, T.B. Issekutz, J.R. Wright, Jr., Islet allograft rejection in rats: a time course study characterizing adhesion molecule expression, MHC expression, and infiltrate immunophenotypes, Cell Transplant 7(3) (1998) 285-97.

[151] B. Hirshberg, S. Mog, N. Patterson, J. Leconte, D.M. Harlan, Histopathological study of intrahepatic islets transplanted in the nonhuman primate model using edmonton protocol immunosuppression, J Clin Endocrinol Metab 87(12) (2002) 5424-9.

[152] M. McCall, A.M. Shapiro, Update on islet transplantation, Cold Spring Harb Perspect Med 2(7) (2012) a007823.

[153] K.I. Rother, D.M. Harlan, Challenges facing islet transplantation for the treatment of type 1 diabetes mellitus, J Clin Invest 114(7) (2004) 877-83.

[154] N. Kim, S.G. Cho, Clinical applications of mesenchymal stem cells, Korean J Intern Med 28(4) (2013) 387-402.

[155] Approved Cellular and Gene Therapy Products, 2021. https://www.fda.gov/vaccines-blood-biologics/cellular-gene-therapy-products/approved-cellular-and-gene-therapy-products. (Accessed 03/16/2021 2021).

Publications and Patents

<u>Paez-Mayorga J</u>, Capuani S, Hernandez N, Farina M, Chua CYX, Blanchard R, Sizovs A, Liu H, Fraga DW, Niles JA, Salazar HF, Corradetti B, Sikora AG, Kloc M, Li XC, Gaber AO, Nichols JE, Grattoni A. (2020). Neovascularized implantable cell homing encapsulation platform with tunable local immunosuppressant delivery for allogeneic cell transplantation. Biomaterials, doi: 10.1016/j.biomaterials.2020.120232.

<u>Paez-Mayorga J</u>, Capuani S, Farina M, Lotito ML, Niles JA, Rhudy J, Esnaola L, Chua YX, Taraballi F, Corradetti B, Shelton KA, Nehete P, Nichols JE, Grattoni A. (2020). Enhanced In Vivo Vascularization of 3D-Printed Cell Encapsulation Device Using Platelet Rich Plasma and Mesenchymal Stem Cells. Adv. Healthc. Mat, doi: https://doi.org/10.1002/adhm.202000670

<u>Paez-Mayorga, J.</u>, Hernandez-Vargas, G., Ruiz-Esparza, G. U., Iqbal, H. M. N., Wang, X., Zhang, Y. S., Parra-Saldivar, R., and Khademhosseini, A. (2019). Bioreactors for Cardiac Tissue Engineering. Adv Healthc Mater, 8(7), e1701504. doi:10.1002/adhm.201701504

<u>Paez-Mayorga, J.</u>, Chen, A. L., Kotla, S., Tao, Y., Abe, R. J., He, E. D., Danysh, B. P., Hofmann, M. C., and Le, N. T. (2018). Ponatinib Activates an Inflammatory Response in Endothelial Cells via ERK5 SUMOylation. Front Cardiovasc Med, 5, 125. doi:10.3389/fcvm.2018.00125

US Provisional Patent Application 63/043,439, (2020) "Transcutaneously refillable cell confinement platform with local trophic factor delivery." Grattoni A, <u>Paez-Mayorga J</u>, Capuani S.

Liu, H.C., Viswanath, D., Pesaresi, F., Xu, Y., Zhang, L., Di Trani, N., <u>Paez-Mayorga, J.</u>, Hernandez, N., Wang, Y., Erm, D.R., Ho, J., Susnjar, A., Liu, X., Demaria, S., Chen, S.H., Teh, B.S., Butler, E.B., Chua, C.Y.X., Grattoni, A. (2020). Potentiating anti-tumor efficacy through radiation and sustained intratumoral delivery of anti-CD40 and anti-PDL1. Int. J. Radiat. Oncol. Biol. Phys., doi: 10.1016/j.ijrobp.2020.07.2326

Abe, R. J., Savage, H., Imanishi, M., Banerjee, P., Kotla, S., <u>Paez-Mayorga, J.</u>, Taunton, J., Fujiwara, K., Won, J. H., Yusuf, S. W., Palaskas, N. L., Banchs, J., Lin, S. H., Schadler, K. L., Abe, J. I., & Le, N. T. (2020). p90RSK-MAGI1 Module Controls Endothelial Permeability by Post-translational Modifications of MAGI1 and Hippo Pathway. Front Cardiovasc Med, 7, 542485. doi: 10.3389/fcvm.2020.542485

Abe, J. I., Ko, K. A., Kotla, S., Wang, Y., <u>Paez-Mayorga, J.</u>, Shin, I. J., Imanishi, M., Vu, H. T., Tao, Y., Leiva-Juarez, M. M., Thomas, T. N., Medina, J. L., Won, J. H,. Fujii, Y., Giancursio, C. J., McBeath, E., Shin, J. H., Guzman, L., Abe, R. J., Taunton, J., Mochizuki, W., Faubion, W., Cooke, J.P., Fujiwara, K., Evans, S. E., and Le, N. T. (2019). MAGI1 as a link between endothelial activation and ER stress drives atherosclerosis. JCI Insight, 4(7). doi:10.1172/jci.insight.125570

Kotla, S., Vu, H. T., Ko, K. A., Wang, Y., Imanishi, M., Heo, K. S., Fujii, Y., Thomas, T. N., Gi, Y. J., Mazhar, H., <u>Paez-Mayorga, J.</u>, Shin, J. H., Tao, Y., Giancursio, C. J.,

Medina, J. L., Taunton, J., Lusis, A. J., Cooke, J. P., Fujiwra, K., Le, N. T., and Abe, J. I. (2019). Endothelial senescence is induced by phosphorylation and nuclear export of telomeric repeat binding factor 2-interacting protein. JCI Insight, 4(9). doi:10.1172/jci.insight.124867

Pons-Faudoa, F. P., Sizovs, A., Di Trani, N., Paez-Mayorga, J., Bruno, G., Rhudy, J., Manohar, M., Gwenden, K., Martini, C., Chua, C. Y. X., Varchi, G., Marzinke, M. A., and Grattoni, A. (2019). 2-Hydroxypropyl-beta-cyclodextrin-enhanced pharmacokinetics of cabotegravir from a nanofluidic implant for HIV pre-exposure prophylaxis. J Control Release, 306, 89-96. doi:10.1016/j.jconrel.2019.05.037
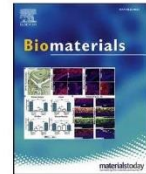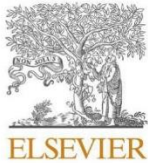
Check for updates

Neovascularized implantable cell homing encapsulation platform with tunable local immunosuppressant delivery for allogeneic cell transplantation

Jesus Paez-Mayorga [a,b], Simone Capuani [a], Nathanael Hernandez [a], Marco Farina [a,c], Corrine Ying Xuan Chua [a], Ryan Blanchard [a], Antons Sizovs [a], Hsuan-Chen Liu [a,d], Daniel W. Fraga [e], Jean A. Niles [f], Hector F. Salazar [a], Bruna Corradetti [a,g], Andrew G. Sikora [d], Malgorzata Kloc [e,h,i], Xian C. Li [e,h], A. Osama Gaber [e], Joan E. Nichols [f], Alessandro Grattoni [a,e,j,*]

[a] Department of Nanomedicine, Houston Methodist Research Institute, Houston, United States
[b] School of Medicine and Health Sciences, Tecnologico de Monterrey, Monterrey, Mexico
[c] Department of Electronics and Telecommunications, Politecnico di Torino, Torino, Italy
[d] Department of Otolaryngology-Head and Neck Surgery, Baylor College of Medicine, Houston, United States
[e] Department of Surgery, Houston Methodist Hospital, Houston, United States
[f] University of Texas Medical Branch, Galveston, United States
[g] Center for NanoHealth, Swansea University Medical School, Swansea, Wales, United Kingdom
[h] Immunobiology and Transplant Science Center, Houston Methodist Hospital, Houston, United States
[i] MD Anderson Cancer Center, University of Texas, Houston, United States
[j] Department of Radiation Oncology, Houston Methodist Hospital, Houston, United States

ABSTRACT

Cell encapsulation is an attractive transplantation strategy to treat endocrine disorders. Transplanted cells offer a dynamic and stimulus-responsive system that secretes therapeutics based on patient need. Despite significant advancements, a challenge in allogeneic cell encapsulation is maintaining sufficient oxygen and nutrient exchange, while providing protection from the host immune system. To this end, we developed a subcutaneously implantable dual-reservoir encapsulation system integrating in situ prevascularization and local immunosuppressant delivery, termed NICHE. NICHE structure is 3D-printed in biocompatible polyamide 2200 and comprises of independent cell and drug reservoirs separated by a nanoporous membrane for sustained local release of immunosuppressant. Here we present the development and characterization of NICHE, as well as efficacy validation for allogeneic cell transplantation in an immunocompetent rat model. We established biocompatibility and mechanical stability of NICHE. Further, NICHE vascularization was achieved with the aid of mesenchymal stem cells. Our study demonstrated sustained local elution of immunosuppressant (CTLA4Ig) into the cell reservoir protected transcutaneously-transplanted allogeneic Leydig cells from host immune destruction during a 31-day study, and reduced systemic drug exposure by 12-fold. In summary, NICHE is the first encapsulation platform achieving both in situ vascularization and immunosuppressant delivery, presenting a viable strategy for allogeneic cell transplantation.

1. Introduction

Technological advances in cell encapsulation are poised to profoundly transform the field of cell transplantation for management of chronic medical conditions, including cardiovascular, neurodegenerative, autoimmune, and endocrine disorders [1–6]. Encapsulation platforms confine transplanted cells within an environment that permits effective oxygen, nutrient, and metabolite transport for prolonged cell viability. For allotransplantation, encapsulation systems could prevent graft rejection by protecting from the host immune

FULL PAPER

ADVANCED
HEALTHCARE
MATERIALS

Check for updates

www.advhealthmat.de

Enhanced In Vivo Vascularization of 3D-Printed Cell Encapsulation Device Using Platelet-Rich Plasma and Mesenchymal Stem Cells

Jesus Paez-Mayorga, Simone Capuani, Marco Farina, Maria Luisa Lotito, Jean A. Niles, Hector F. Salazar, Jessica Rhudy, Lucas Esnaola, Corrine Ying Xuan Chua, Francesca Taraballi, Bruna Corradetti, Kathryn A. Shelton, Pramod N. Nehete, Joan E. Nichols, and Alessandro Grattoni*

The current standard for cell encapsulation platforms is enveloping cells in semipermeable membranes that physically isolate transplanted cells from the host while allowing for oxygen and nutrient diffusion. However, long-term viability and function of encapsulated cells are compromised by insufficient oxygen and nutrient supply to the graft. To address this need, a strategy to achieve enhanced vascularization of a 3D-printed, polymeric cell encapsulation platform using platelet-rich plasma (PRP) and mesenchymal stem cells (MSCs) is investigated. The study is conducted in rats and, for clinical translation relevance, in nonhuman primates (NHP). Devices filled with PRP, MSCs, or vehicle hydrogel are subcutaneously implanted in rats and NHP and the amount and maturity of penetrating blood vessels assessed via histopathological analysis. In rats, MSCs drive the strongest angiogenic response at early time points, with the highest vessel density and endothelial nitric oxide synthase (eNOS) expression. In NHP, PRP and MSCs result in similar vessel densities but incorporation of PRP ensues higher levels of eNOS expression. Overall, enrichment with PRP and MSCs yields extensive, mature vascularization of subcutaneous cell encapsulation devices. It is postulated that the individual properties of PRP and MSCs can be leveraged in a synergistic approach for maximal vascularization of cell encapsulation platforms.

1. Introduction

Cell transplantation is an attractive therapeutic modality where live cells are administered to the patient in lieu of traditional therapeutics. Transplanted cells serve as bioreactors that produce and release therapeutic molecules continuously (i.e., engineered cells) or in response to stimuli (i.e., pancreatic islets), based on patient need. In light of its versatility, cell transplantation holds great promise for treatment of various diseases including diabetes and hormone deficiencies, renal failure, genetic, and neurological disorders.[1]

A key aspect required for viability and function of transplanted cells is adequate oxygen, nutrient, and metabolite transfer between the host and transplant microenvironment. To achieve this, several encapsulation platforms were designed to envelop cells in semipermeable membranes with pores sizes suitable to permit sufficient mass transfer, while preventing cell leakage from the platform. Furthermore, in the eventuality of an allogeneic or xenogeneic

J. Paez-Mayorga, S. Capuani, Dr. M. Farina, M. L. Lotito, H. F. Salazar, J. Rhudy, L. Esnaola, Dr. C. Y. X. Chua, Dr. B. Corradetti, Prof. A. Grattoni
Department of Nanomedicine
Houston Methodist Research Institute
Houston, TX 77030, USA
E-mail: agrattoni@houstonmethodist.org
J. Paez-Mayorga
School of Medicine and Health Sciences
Tecnologico de Monterrey
Monterrey, NL 64849, Mexico

Dr. M. Farina
Department of Electronics and Telecommunications
Politecnico di Torino
Torino, TO 10129, Italy
M. L. Lotito
Department of Mechanical and Aerospace Engineering
Politecnico di Torino
Torino, TO 10129, Italy
J. A. Niles, Prof. J. E. Nichols
University of Texas Medical Branch
Galveston, TX 77550, USA
Dr. F. Taraballi
Regenerative Medicine Program
Houston Methodist Research Institute
Houston, TX 77030, USA

Bioreactors for Cardiac Tissue Engineering

Jesus Paez-Mayorga, Gustavo Hernández-Vargas, Guillermo U. Ruiz-Esparza, Hafiz M. N. Iqbal, Xichi Wang, Yu Shrike Zhang, Roberto Parra-Saldivar,* and Ali Khademhosseini*

The advances in biotechnology, biomechanics, and biomaterials can be used to develop organ models that aim to accurately emulate their natural counterparts. Heart disease, one of the leading causes of death in modern society, has attracted particular attention in the field of tissue engineering. To avoid incorrect prognosis of patients suffering from heart disease, or from adverse consequences of classical therapeutic approaches, as well as to address the shortage of heart donors, new solutions are urgently needed. Biotechnological advances in cardiac tissue engineering from a bioreactor perspective, in which recapitulation of functional, biochemical, and physiological characteristics of the cardiac tissue can be used to recreate its natural microenvironment, are reviewed. Detailed examples of functional and preclinical applications of engineered cardiac constructs and the state-of-the-art systems from a bioreactor perspective are provided. Finally, the current trends and future directions of the field for its translation to clinical settings are discussed.

1. Introduction

Cardiovascular disease, a set of pathologies that include myocardial infarction (MI) and heart failure, is the leading cause of death around the globe.[1,2] The healthy tissue that remains after an ischemic event lacks the necessary mechanical support to properly maintain cardiac function, leading to stress and chronic inflammatory response that eventually cause heart failure.[1,2] While pharmacological approaches have been able to delay the progression toward this devastating disease, the only permanent treatment for end-stage heart failure is cardiac transplantation.[3,4] However, the limited availability of heart donors and the problem of immunosuppression limits the widespread use of this approach.[3,5]

J. Paez-Mayorga
Tecnologico de Monterrey
School of Medicine and Health Sciences
Ave. Eugenio Garza Sada 2501, Monterrey, N. L., CP 64849, Mexico
G. Hernández-Vargas, Prof. H. M. N. Iqbal, Prof. R. Parra-Saldivar
Tecnologico de Monterrey
School of Engineering and Sciences
Campus Monterrey
Ave. Eugenio Garza Sada 2501, Monterrey, N. L., CP 64849, Mexico
E-mail: r.parra@itesm.mx
Dr. G. U. Ruiz-Esparza, Dr. X. Wang, Dr. Y. S. Zhang, Prof. R. Parra-Saldivar, Prof. A. Khademhosseini
Division of Engineering in Medicine
Department of Medicine
Brigham and Women's Hospital
Harvard Medical School
Cambridge, MA 02139, USA
E-mail: khademh@ucla.edu
Dr. G. U. Ruiz-Esparza, Dr. X. Wang, Dr. Y. S. Zhang, Prof. R. Parra-Saldivar, Prof. A. Khademhosseini
Harvard-MIT Division of Health Sciences and Technology
Massachusetts Institute of Technology
Cambridge, MA 02139, USA
Prof. R. Parra-Saldivar
Microsystems Technologies Laboratories
MIT
Cambridge, MA 02139, USA

Prof. A. Khademhosseini
Department of Bioengineering
Department of Chemical and Biomolecular Engineering
Henry Samueli School of Engineering and Applied Sciences
University of California-Los Angeles
Los Angeles, CA 90095, USA
Prof. A. Khademhosseini
Department of Radiology
David Geffen School of Medicine
University of California-Los Angeles
Los Angeles, CA 90095, USA
Prof. A. Khademhosseini
Center for Minimally Invasive Therapeutics (C-MIT)
University of California-Los Angeles
Los Angeles, CA 90095, USA
Prof. A. Khademhosseini
California NanoSystems Institute (CNSI)
University of California-Los Angeles
Los Angeles, CA 90095, USA
Prof. A. Khademhosseini
College of Animal Bioscience and Technology
Department of Bioindustrial Technologies
Konkuk University
Hwayang-dong, Kwangjin-gu, Seoul 143-701, Republic of Korea
Prof. A. Khademhosseini
Center for Nanotechnology
King Abdulaziz University
Jeddah 21569, Saudi Arabia

Ponatinib Activates an Inflammatory Response in Endothelial Cells via ERK5 SUMOylation

Jesus Paez-Mayorga [1,2], Andrew L. Chen [1], Sivareddy Kotla [3], Yunting Tao [1], Rei J. Abe [1], Emma D. He [1], Brian P. Danysh [4], Marie-Claude C. Hofmann [4] and Nhat-Tu Le [1*]

[1] Department of Cardiovascular Sciences, Center of Cardiovascular Regeneration Houston, Methodist Research Institute, Methodist Hospital, Houston, TX, United States, [2] Tecnologico de Monterrey, Escuela de Medicina y Ciencias de la Salud, Monterrey, Mexico, [3] Department of Cardiology, The University of Texas MD Anderson Cancer Center, Houston, TX, United States, [4] Department of Endocrine Neoplasia and Hormonal Disorders, University of Texas MD Anderson Cancer Center, Houston, TX, United States

Ponatinib is a multi-targeted third generation tyrosine kinase inhibitor (TKI) used in the treatment of chronic myeloid leukemia (CML) patients harboring the Abelson (Abl)-breakpoint cluster region (Bcr) T315I mutation. In spite of having superb clinical efficacy, ponatinib triggers severe vascular adverse events (VAEs) that significantly limit its therapeutic potential. On vascular endothelial cells (ECs), ponatinib promotes EC dysfunction and apoptosis, and inhibits angiogenesis. Furthermore, ponatinib-mediated anti-angiogenic effect has been suggested to play a partial role in systemic and pulmonary hypertension via inhibition of vascular endothelial growth factor receptor 2 (VEGFR2). Even though ponatinib-associated VAEs are well documented, their etiology remains largely unknown, making it difficult to efficiently counteract treatment-related adversities. Therefore, a better understanding of the mechanisms by which ponatinib mediates VAEs is critical. In cultured human aortic ECs (HAECs) treated with ponatinib, we found an increase in nuclear factor NF-kB/p65 phosphorylation and NF-kB activity, inflammatory gene expression, cell permeability, and cell apoptosis. Mechanistically, ponatinib abolished extracellular signal-regulated kinase 5 (ERK5) transcriptional activity even under activation by its upstream kinase mitogen-activated protein kinase kinase 5α (CA-MEK5α). Ponatinib also diminished expression of ERK5 responsive genes such as Krüppel-like Factor 2/4 (klf2/4) and eNOS. Because ERK5 SUMOylation counteracts its transcriptional activity, we examined the effect of ponatinib on ERK5 SUMOylation, and found that ERK5 SUMOylation is increased by ponatinib. We also found that ponatibib-mediated increased inflammatory gene expression and decreased anti-inflammatory gene expression were reversed when ERK5 SUMOylation was inhibited endogenously or exogenously. Overall, we propose a novel mechanism by which ponatinib up-regulates endothelial ERK5 SUMOylation and shifts ECs to an inflammatory phenotype, disrupting vascular homeostasis.

Keywords: ponatinib, vascular adverse events, ERK5 SUMOylation, EC inflammation, tyrosine kinase inhibtor (TKI)

80

Biology Contribution

Potentiating Antitumor Efficacy Through Radiation and Sustained Intratumoral Delivery of Anti-CD40 and Anti-PDL1

Hsuan-Chen Liu, PhD,* Dixita I. Viswanath, BS,*,† Federica Pesaresi, MS,*,‡ Yitian Xu, PhD,§,‖ Licheng Zhang, PhD,§,‖ Nicola Di Trani, MS,*,¶ Jesus Paez-Mayorga, BA,*,# Nathanael Hernandez, BS,* Yu Wang, PhD,* Donald R. Erm, AAS,* Jeremy Ho, MD,*,** Antonia Susnjar, BS,* Xuewu Liu, PhD,* Sandra Demaria, PhD,** Shu-Hsia Chen, PhD,§,‖ Bin S. Teh, MD,**,†† Edward Brian Butler, MD,†† Corrine Ying Xuan Chua, PhD,* and Alessandro Grattoni, PhD*,††,‡‡

*Department of Nanomedicine, Houston Methodist Research Institute, Houston, Texas; †Texas A&M University, College of Medicine, Bryan, Texas; ‡Department of Electronics and Telecommunications, Politecnico di Torino, Torino, Italy; §Center for Immunotherapy Research, Houston Methodist Research Institute, Houston, Texas; ‖ImmunoMonitoring Core, Houston Methodist Research Institute, Houston, Texas; ¶University of Chinese Academy of Science (UCAS), Beijing, China; #Tecnologico de Monterrey, School of Medicine and Health Sciences, Monterrey, NL, Mexico; **Weill Cornell Medical College, Weill Cornell Medicine, New York, New York; ††Department of Radiation Oncology, Houston Methodist Research Institute, Houston, Texas; and ‡‡Department of Surgery, Houston Methodist Research Institute, Houston, Texas

Purpose: Mounting evidence demonstrates that combining radiation therapy (RT) with immunotherapy can reduce tumor burden in a subset of patients. However, conventional systemic delivery of immunotherapeutics is often associated with significant adverse effects, which force treatment cessation. The aim of this study was to investigate a minimally invasive

p90RSK-MAGI1 Module Controls Endothelial Permeability by Post-translational Modifications of MAGI1 and Hippo Pathway

Rei J. Abe[1†], Hannah Savage[2†], Masaki Imanishi[3†], Priyanka Banerjee[1], Sivareddy Kotla[3], Jesus Paez-Mayorga[1], Jack Taunton[4], Keigi Fujiwara[3], Jong Hak Won[3], Syed Wamique Yusuf[3], Nicolas L. Palaskas[3], Jose Banchs[3], Steven H. Lin[5], Keri L. Schadler[2*‡], Jun-ichi Abe[3*‡] and Nhat-Tu Le[1*‡]

[1] Department of Cardiovascular Sciences, Center for Cardiovascular Regeneration, Houston Methodist Research Institute, Houston, TX, United States, [2] Department of Pediatric Research, The University of Texas MD Anderson Cancer Center, Houston, TX, United States, [3] Department of Cardiology, The University of Texas MD Anderson Cancer Center, Houston, TX, United States, [4] Department of Cellular and Molecular Pharmacology, University of California, San Francisco, San Francisco, CA, United States, [5] Department of Radiation Oncology, The University of Texas MD Anderson Cancer Center, Houston, TX, United States

Previously, we reported that post-translational modifications (PTMs) of MAGI1, including S741 phosphorylation and K931 de-SUMOylation, both of which are regulated by p90RSK activation, lead to endothelial cell (EC) activation. However, roles for p90RSK and MAGI1-PTMs in regulating EC permeability remain unclear despite MAGI1 being a junctional molecule. Here, we show that thrombin (Thb)-induced EC permeability, detected by the electric cell-substrate impedance sensing (ECIS) based system, was decreased by overexpression of dominant negative p90RSK or a MAGI1-S741A phosphorylation mutant, but was accelerated by overexpression of p90RSK, siRNA-mediated knockdown of *magi1*, or the MAGI1-K931R SUMOylation mutant. MAGI1 depletion also increased the mRNA and protein expression of the large tumor suppressor kinases 1 and 2 (LATS1/2), which inhibited YAP/TAZ activity and increased EC permeability. Because the endothelial barrier is a critical mediator of tumor hypoxia, we also evaluated the role of p90RSK activation in tumor vessel leakiness by using a relatively low dose of the p90RSK specific inhibitor, FMK-MEA. FMK-MEA significantly inhibited tumor vessel leakiness at a dose that does not affect morphology and growth of tumor vessels *in vivo*. These results provide novel insights into crucial roles for p90RSK-mediated MAGI1 PTMs and the Hippo pathway in EC permeability, as well as p90RSK activation in tumor vessel leakiness.

Keywords: p90RSK, SUMOylation, Hippo pathway, EC permeability, MAGI1

INTRODUCTION

Endothelial cell-cell junctions are highly dynamic structures that regulate EC monolayer integrity and barrier function. A number of signaling pathways that regulate cell-cell junctions such as β-catenin phosphorylation and VE-cadherin degradation have been delineated (1–6). Rap1, a member of the Ras-like small GTPase family, has been recognized as a key regulator of cell-cell

MAGI1 as a link between endothelial activation and ER stress drives atherosclerosis

Jun-ichi Abe,[1] Kyung Ae Ko,[1] Sivareddy Kotla,[1] Yin Wang,[1] Jesus Paez-Mayorga,[2,3] Ik Jae Shin,[1] Masaki Imanishi,[1] Hang Thi Vu,[1] Yunting Tao,[2] Miguel M. Leiva-Juarez,[4] Tamlyn N. Thomas,[1] Jan L. Medina,[1] Jong Hak Won,[1] Yuka Fujii,[1] Carolyn J. Giancursio,[2] Elena McBeath,[1] Ji-Hyun Shin,[1] Liliana Guzman,[2] Rei J. Abe,[2] Jack Taunton,[5] Naoki Mochizuki,[6] William Faubion,[7] John P. Cooke,[2] Keigi Fujiwara,[1] Scott E. Evans,[4] and Nhat-Tu Le[2]

[1]Department of Cardiology, The University of Texas MD Anderson Cancer Center, Houston, Texas, USA. [2]Center for Cardiovascular Regeneration, Department of Cardiovascular Sciences, Houston Methodist Research Institute, Houston Texas, USA. [3]Tecnologico de Monterrey, Escuela de Medicina y Ciencias de la Salud, Monterrey, Nuevo Leon, Mexico. [4]Department of Pulmonary Medicine, The University of Texas MD Anderson Cancer Center, Houston, Texas, USA. [5]Department of Cellular and Molecular Pharmacology, University of California, San Francisco, San Francisco, California, USA. [6]Department of Cell Biology, National Cardiovascular Center Research Institute, Osaka, Japan. [7]Division of Gastroenterology and Hepatology, Mayo Clinic, Rochester, Minnesota, USA.

The possible association between the membrane-associated guanylate kinase with inverted domain structure-1 (MAGI1) and inflammation has been suggested, but the molecular mechanisms underlying this link, especially during atherogenesis, remain unclear. In endothelial cells (ECs) exposed to disturbed flow (d-flow), p90 ribosomal S6 kinase (p90RSK) bound to MAGI1, causing MAGI1-S741 phosphorylation and sentrin/SUMO-specific protease 2 T368 phosphorylation-mediated MAGI1-K931 deSUMOylation. MAGI1-S741 phosphorylation upregulated EC activation via activating Rap1. MAGI1-K931 deSUMOylation induced both nuclear translocation of p90RSK-MAGI1 and ATF-6-MAGI1 complexes, which accelerated EC activation and apoptosis, respectively. Microarray screening revealed key roles for MAGI1 in the endoplasmic reticulum (ER) stress response. In this context, MAGI1 associated with activating transcription factor 6 (ATF-6). MAGI1 expression was upregulated in ECs and macrophages found in atherosclerotic-prone regions of mouse aortas as well as in the colonic epithelia and ECs of patients with inflammatory bowel disease. Further, reduced MAGI1 expression in Magi1$^{-/+}$ mice inhibited d-flow–induced atherogenesis. In sum, EC activation and ER stress–mediated apoptosis are regulated in concert by two different types of MAGI1 posttranslational modifications, elucidating attractive drug targets for chronic inflammatory disease, particularly atherosclerosis.

Introduction

Inflammation is an important part of the innate defense system, but this system also plays negative roles in many cases of human diseases. For example, endothelial cell (EC) activation plays a key role in the pathogenesis of atherosclerosis. Proatherogenic agonists, such as inflammatory cytokines and growth factors as well as disturbed flow (d-flow), cause EC activation. In particular, d-flow, which is known to occur in so-called atheroprone areas of large arteries, activates proinflammatory and apoptotic signaling in ECs, leading to EC dysfunction (1, 2). A recent genome-wide association study of an independent cohort of patients with various diseases and healthy controls revealed a possible association between the membrane-associated guanylate kinase with inverted domain structure-1 (MAGI1) locus and the severity of several chronic inflammatory diseases, such as inflammatory bowel disease (IBD), psoriasis, and neuroticism (3–6). Concordantly, MAGI1 mRNA expression levels in small intestine mucosa are increased in patients with IBD (3). These observations suggest that MAGI1 may be involved in the mechanism of EC activation.

MAGI1 is a scaffold protein that contains 6 PSD95/DiscLarge/ZO-1 (PDZ) domains, a guanylate kinase domain, and 2 WW (rsp5) domains flanked by the first and second PDZ domains. MAGI1 is widely

Endothelial senescence is induced by phosphorylation and nuclear export of telomeric repeat binding factor 2–interacting protein

Sivareddy Kotla,[1] Hang Thi Vu,[1] Kyung Ae Ko,[1] Yin Wang,[1] Masaki Imanishi,[1] Kyung-Sun Heo,[1] Yuka Fujii,[1] Tamlyn N. Thomas,[1] Young Jin Gi,[1] Hira Mazhar,[1] Jesus Paez-Mayorga,[2,3] Ji-Hyun Shin,[1] Yunting Tao,[2] Carolyn J. Giancursio,[2] Jan L.M. Medina,[1] Jack Taunton,[4] Aldos J. Lusis,[5] John P. Cooke,[2] Keigi Fujiwara,[1] Nhat-Tu Le,[2] and Jun-ichi Abe[1]

[1]Department of Cardiology, The University of Texas MD Anderson Cancer Center, Houston, Texas, USA. [2]Center for Cardiovascular Regeneration, Department of Cardiovascular Sciences, Houston Methodist Research Institute, Houston, Texas, USA. [3]Tecnologico de Monterrey, Escuela de Medicina y Ciencias de la Salud, Monterrey, Nuevo Leon, Mexico. [4]Department of Cellular and Molecular Pharmacology, UCSF, San Francisco, California, USA. [5]Department of Human Genetics, David Geffen School of Medicine, UCLA, Los Angeles, California, USA.

The interplay among signaling events for endothelial cell (EC) senescence, apoptosis, and activation and how these pathological conditions promote atherosclerosis in the area exposed to disturbed flow (d-flow) in concert remain unclear. The aim of this study was to determine whether telomeric repeat-binding factor 2–interacting protein (TERF2IP), a member of the shelterin complex at the telomere, can regulate EC senescence, apoptosis, and activation simultaneously, and if so, by what molecular mechanisms. We found that d-flow induced p90RSK and TERF2IP interaction in a p90RSK kinase activity–dependent manner. An in vitro kinase assay revealed that p90RSK directly phosphorylated TERF2IP at the serine 205 (S205) residue, and d-flow increased TERF2IP S205 phosphorylation as well as EC senescence, apoptosis, and activation by activating p90RSK. TERF2IP phosphorylation was crucial for nuclear export of the TERF2IP-TRF2 complex, which led to EC activation by cytosolic TERF2IP-mediated NF-κB activation and also to senescence and apoptosis of ECs by depleting TRF2 from the nucleus. Lastly, using EC-specific TERF2IP-knockout (TERF2IP-KO) mice, we found that the depletion of TERF2IP inhibited d-flow–induced EC senescence, apoptosis, and activation, as well as atherosclerotic plaque formation. These findings demonstrate that TERF2IP is an important molecular switch that simultaneously accelerates EC senescence, apoptosis, and activation by S205 phosphorylation.

Introduction

Endothelial cell (EC) activation is characterized by the increased expression of adhesion molecules and chemokines that promote vascular inflammation (1). EC senescence is associated with EC activation, also known as senescence-associated secretory phenotype (SASP) (2). Telomere (TL) shortening contributes to EC senescence, which is associated with the development of atherosclerotic plaques (3, 4). It is well known that disturbed (as opposed to laminar) blood flow (d-flow) induces both EC activation and senescence (5, 6), but how these 2 pathological conditions are concomitantly upregulated by d-flow and subsequently lead to vascular plaque formation are poorly understood. The shelterin complex (TRF1, TRF2, TERF2IP, POT1, TPP1, and TIN2) of the mammalian TL (7) is known to maintain TL length. The complex appears to prevent TLs from shortening rather than to promote telomerase activity (8). In fact, telomerase activity is absent or very low in most adult tissues (7), and substantial evidence indicates that TL shortening, which is induced by depletion of the shelterin complex, is associated with cellular senescence (9, 10). However, whether the shelterin complex plays a role in atherogenesis is unclear. TERF2IP is a member of the shelterin complex of the mammalian TL and can bind both telomeric and nontelomeric chromatin (7), and it is involved in the protection of TLs (7). TERF2IP forms a complex

84

2-Hydroxypropyl-β-cyclodextrin-enhanced pharmacokinetics of cabotegravir from a nanofluidic implant for HIV pre-exposure prophylaxis

Fernanda P. Pons-Faudoa[a,b], Antons Sizovs[a], Nicola Di Trani[a,c], Jesus Paez-Mayorga[a,b], Giacomo Bruno[a,d], Jessica Rhudy[a], Madhuri Manohar[e], Kevin Gwenden[e], Cecilia Martini[f], Corrine Ying Xuan Chua[a], Greta Varchi[f], Mark A. Marzinke[e], Alessandro Grattoni[a,g,h,*]

[a] Department of Nanomedicine, Houston Methodist Research Institute (HMRI), Houston, TX, USA
[b] Tecnologico de Monterrey, School of Medicine and Health Sciences, Monterrey, NL, Mexico
[c] University of Chinese Academy of Science (UCAS), Beijing, China
[d] Politecnico di Torino, Turin, Italy
[e] School of Medicine, Johns Hopkins University, Baltimore, MD, USA
[f] Chemistry and Nanotechnology Unit, Institute of Organic Synthesis and Photoreactivity (IOSP), Bologna, Italy
[g] Department of Surgery, Houston Methodist Hospital, Houston, TX, USA
[h] Department of Radiation Oncology, Houston Methodist Hospital, Houston, TX, USA

ARTICLE INFO

ABSTRACT

Preexposure prophylaxis (PrEP) with antiretrovirals (ARV) can prevent human immunodeficiency virus (HIV) transmission, but its efficacy is highly dependent on strict patient adherence to daily dosing regimen. Long-acting (LA) ARV formulations or delivery systems that reduce dosing frequency may increase adherence and thus PrEP efficacy. While cabotegravir (CAB) long-acting injectable (CAB LA), an integrase strand transfer inhibitor (INSTI), reduces dosing frequency to bimonthly injections, variable pharmacokinetics (PK) between patients and various adverse reactions necessitate improvement in delivery methods. Here we developed a subcutaneously implantable nanofluidic device for the sustained delivery of CAB formulated with 2-hydroxypropyl-β-cyclodextrin (βCAB) and examined the pharmacokinetics (PK) in Sprague-Dawley rats for 3 months in comparison to CAB. Our study demonstrated βCAB treatment group maintained clinically-relevant plasma CAB concentrations 2 times above the protein-adjusted concentration that inhibits viral replication by 90% (2 × PA-IC$_{90}$) and drug penetration into tissues relevant to HIV-1 transmission. Further, we successfully fitted plasma CAB concentrations into a PK model (R^2 = 0.9999) and determined CAB apparent elimination half-life of 47 days. Overall, our data shows the potential of sustained release of βCAB via a nanofluidic implant for long-term PrEP delivery, warranting further investigation for efficacy against HIV infections.

1. Introduction

HIV-1 has infected 77.3 million people since the start of the epidemic and is now a pandemic with approximately 36.9 million people living with the illness and approximately 1.8 million new infections occurring yearly [1]. The Joint United Nations Programme on HIV/AIDS (UNAIDS) spent substantial resources to combat this disease and established a strategic roadmap toward reducing the number of new infections below 500,000 by 2020. However, the 2016 'Prevention Gap Report' from the UNAIDS indicated that attempts to reach this milestone have derailed, with increasing HIV incidence in some countries [2]. Considerable efforts are focused on prevention strategies, of which PrEP with ARVs are proven to be effective at reducing the incidence of

HIV-1 infection as observed in the HPTN 052-TaSP, Partners PrEP, and iPrEx studies [3–5]. Thus far, Truvada, an oral fixed-dose formulation of two nucleotide reverse transcriptase inhibitors, tenofovir disoproxil fumarate (TDF) and emtricitabine (FTC) (TDF/FTC), is the only Food and Drug Administration (FDA)-approved ARV for HIV-1 PrEP. Daily oral Truvada dosing confirmed by detectable drug levels has demonstrated 92% risk reduction in HIV-1 infection in men and transgender women who have sex with men and 90% in sexually active heterosexual adults [4–9]. On the contrary, poor adherence to PrEP exhibited no relative risk reduction on the rates of HIV-1 acquisition [8,10,11].

Prevention is paramount and superior strategies for HIV-1 PrEP are needed to improve adherence and reach the goal of ending the pandemic by 2030 [12]. In light of this, extensive global endeavors are

Curriculum Vitae

Jesús Páez Mayorga enrolled into the MD PhD program at Tecnologico de Monterrey, School of Medicine and Health Sciences, Monterrey Campus in 2012. From 2012 through 2015, Jesus completed 3 consecutive summer research internships at Houston Methodist Research Institute in the departments of Nanomedicine and Infectious Diseases, earning him the Research and Innovation Diploma. In the Spring of 2016, Jesus graduated Magna Cum Laude with a Bachelor of Arts in Biosciences from Tecnologico de Monterrey. In the fall of 2016 Jesus started his PhD (within the MD PhD curriculum) as part of a joint program between Tecnologico de Monterrey and Houston Methodist Research Institute. Jesus completed his first research year (2017-2018) at the Department of Cardiovascular Regeneration under the co-mentorship of John P. Cooke, MD PhD and Nhat-Tu Le, PhD. In 2018, Jesus joined the laboratory of Alessandro Grattoni in the Department of Nanomedicine where he completed his doctoral thesis work in an implantable encapsulation platform for transplantation of allogeneic islets to treat diabetes, which resulted in 2 original research publications and 1 patent. In addition, during his PhD, Jesus co-authored 8 research and review papers. Jesus' doctoral work was selected for presentation at various scientific conferences (listed below) and earned awards in the poster and short talk categories. From 2019-2020 Jesus served on the board of the Methodist Association for Postdoctoral and Trainee Affairs (MAPTA) as vice-president of international affairs where he organized events and workshops catered for the vast international community of trainees at Houston Methodist. Upon completion of his PhD, Jesus will stay on as a postdoctoral fellow under the continued mentorship of Dr. Grattoni for 9 months after which he will resume medical school with expected graduation in 2024.

Oral presentations:
➢ Keystone Symposia - Emerging Cell Therapies: Realizing the Vision of NextGen Cell Therapeutics, Virtual, 2021.
➢ J.C. Walter Transplant Center Research Retreat, Houston, TX, 2019.
➢ 2nd Annual MAPTA Summer Science Symposium, Houston, TX, 2019. (First place award).

Poster presentations:
➢ Advanced Technologies and Treatments for Diabetes, Virtual, 2021.
➢ Fall Symposium of the Department of Nanomedicine, Houston, TX, 2020.
➢ Fall Symposium of the Department of Nanomedicine, Houston, TX, 2019. (Second place award).
➢ Keystone Symposium - Vascular Biology and Human Diseases, Santa Fe, NM, 2018.
➢ Gulf Coast Vascular Research Consortium, College Station, TX, 2018.

This document was typed in using Microsoft Word by Jesús Páez Mayorga